

FIELD-DRIVEN DYNAMICS OF DILUTE GASES, VISCOUS LIQUIDS AND  
POLYMER CHAINS

by

ARUNA MOHAN

B. Tech. Chemical Engineering, Indian Institute of Technology, Delhi (2002),  
M. S. Chemical Engineering Practice, Massachusetts Institute of Technology (2006).

Submitted to the Department of Chemical Engineering  
in partial fulfillment of the requirements for the degree of

Doctor of Philosophy in Chemical Engineering

at the

MASSACHUSETTS INSTITUTE OF TECHNOLOGY

September 2007

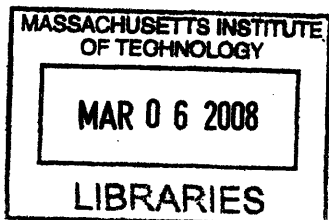
© Massachusetts Institute of Technology 2007. All rights reserved.

Author \_\_\_\_\_  
Department of Chemical Engineering  
August 31, 2007

Certified by \_\_\_\_\_  
Patrick S. Doyle  
Doherty Associate Professor of Chemical Engineering  
Thesis Supervisor

Certified by \_\_\_\_\_  
Howard Brenner  
Willard Henry Dow Professor Emeritus of Chemical Engineering  
Thesis Supervisor

Accepted by \_\_\_\_\_  
William M. Deen  
Chairman, Department Committee on Graduate Students



ARCHIVES



## Field-Driven Dynamics of Dilute Gases, Viscous Liquids and Polymer Chains

by  
Aruna Mohan

Submitted to the Department of Chemical Engineering  
on August 31, 2007, in partial fulfillment of the  
requirements for the degree of  
Doctor of Philosophy in Chemical Engineering

### Abstract

This thesis is concerned with the exploration of field-induced dynamical phenomena arising in dilute gases, viscous liquids and polymer chains. The problems considered herein pertain to the slip-induced motion of a rigid, spherical or nonspherical particle in a fluid in the presence of an inhomogeneous temperature or concentration field or an electric field, and the dynamics of charged polymers animated by the application of an electric field.

The problems studied in this thesis are unified by the existence of a separation of length scales between the macroscopic phenomena of interest and their microscopic underpinnings, and are treated by means of coarse-graining principles that exploit this scale separation. Specifically, the first part of this thesis investigates the dynamics caused by the existence of a slip velocity at a fluid–solid interface. The macroscopic slip boundary condition obtains from the asymptotic matching of the velocity within the microscale layer of fluid adjoining the solid surface, and the velocity in the bulk fluid. In the case of a gas, the microscopic length scale is constituted by the mean free path, and the layer of gas adjoining the solid boundary having a thickness of the order of the mean free path is referred to as the Knudsen layer. The parameter representing the ratio of the mean free path to the macroscopic length scale is the Knudsen number, denoted  $Kn$ . The widely-used Navier–Stokes and Fourier equations are valid away from the solid boundary at distances large compared to the mean free path in the limit  $Kn \ll 1$ , and necessitate the imposition of continuum boundary conditions on the gas velocity and temperature at the outer limit of the Knudsen layer. These macroscopic equations are typically solved subject to the no-slip of velocity and the equality of the gas and solid temperatures at the solid boundary. However, as first pointed out by Maxwell, the no-slip boundary condition fails to explain experimentally observed phenomena when imposed at the surface of a nonuniformly heated solid, and must be replaced by the thermal slip condition obtained via the asymptotic matching of the velocity within the Knudsen layer with that in the bulk gas. Slip has also been proposed to occur at liquid–solid boundaries under conditions of inhomogeneous temperature or concentration.

In this thesis, we extend Faxen’s laws for the force and torque acting on a spherical particle in a fluid with a prescribed undisturbed flow field to account for the existence of fluid slip at the particle surface. Additionally, we investigate the effect of particle asymmetry by studying the motion of a slightly deformed sphere in a fluid having a uniform unperturbed flow field, and demonstrate that the velocity of a force- and torque-free particle is independent of its size or shape. While the slip-induced motions studied in this thesis are presented in the context of thermally-induced slip arising from the existence of a temperature gradient, the results are equally applicable

to more general phoretic transport, encompassing the electrokinetic slip condition employed in the treatment of charged particle dynamics in an electrolytic liquid. Analogous to the thermal slip condition imposed on a gas at the outer limit of the Knudsen layer, the electrokinetic slip condition is imposed at the outer limit of the layer of counterions surrounding a charged surface in an electrolytic liquid.

The studies presented in this thesis have potential applications in aerosol and colloid technology, in the nonisothermal transport of particulates in porous media and MEMS devices, and in the electrophoresis of charged bodies.

The behavior of a charged polymer molecule in an electric field constitutes the subject of the second part of this thesis. Motivated by the medical and technological necessity to effect the size-separation of DNA chains in applications ranging from the Human Genome Project to DNA-based criminology, we consider specifically the dynamics of electric-field driven DNA chains in size-based separation devices. The conventional technique of constant-field gel electrophoresis is ineffective in achieving the separation of long DNA chains whose sizes exceed a few tens of kilobase pairs, owing to the fact that the velocity becomes independent of chain size for long chains in a gel. This limitation of gel electrophoresis has spurred the development of alternative separation devices, such as obstacle courses confined to microchannels wherein the obstacles may be either microfabricated or formed from the self-assembly of paramagnetic beads into columns upon the imposition of a magnetic field transverse to the channel plane. Size separation in the latter devices arises from the fact that longer chains, when driven through the channel by an applied electric field, are more likely to collide with the obstacles and take longer to disentangle from the obstacle once a collision has occurred, relative to shorter chains. Consequently, a longer chain requires more time to traverse the array compared to a shorter chain.

As a model for the transient chain stretching occurring subsequent to the collision of an electrophoresing DNA molecule with an obstacle, we study the unraveling of a single, tethered polymer molecule in a uniform solvent flow field. In the context of a polymer, the microscopic length scale is associated with the size of a monomer. We, however, employ a coarse-grained representation wherein the polymer is modeled by a chain of entropic springs connected by beads, with each bead representing several monomers, thereby enabling a continuum description of the solvent. We adopt the method of Brownian dynamics applied to the bead-spring model of the polymer chain. We consider both linear force-extension behavior, representative of chain stretching in a weak field, and the finitely-extensible wormlike chain model of DNA elasticity, which dominates chain stretching under strong fields. The results yield insight into the mechanism of tension propagation during chain unraveling, and are more generally applicable to situations involving transient stretching, such as chain interactions arising in entangled polymer solutions.

We next conduct investigations of chain dynamics in obstacle-array based separation devices by means of coarse-grained stochastic modeling and Brownian dynamics simulation of a chain in a self-assembled array of magnetic beads, and predict the separation achievable among different chain sizes. We examine the influence of key parameters, namely, the applied electric field strength and the spacing between obstacles, on the separation resolution effected by the device. Our results elucidate the mechanisms of DNA dynamics in microfluidic separation devices, and are expected to aid in the design of DNA separation devices and the selection of parameters for their optimal operation.

Thesis Supervisor: Patrick S. Doyle

Title: Doherty Associate Professor of Chemical Engineering

Thesis Supervisor: Howard Brenner

Title: Willard Henry Dow Professor Emeritus of Chemical Engineering



---

## *Acknowledgements*

---

I wish to express my deep gratitude to Professor Patrick Doyle for guiding my research on the modeling of DNA dynamics. Professor Doyle has always been willing to make time for discussions on matters of research, as well as for career guidance and advice. I have greatly benefitted from my interactions with him over the past few years. My research on the dynamics of viscous fluids was carried out under the supervision of Professor Howard Brenner, whom I thank for his input in that area. I am grateful to my thesis committee, Professors Armstrong, Oppenheim and Smith, for encouraging me to think critically and independently, to express my views, and to conduct research in diverse areas. I am also very grateful to Professor Blankshtein, former Chairman of the Committee on Graduate Students, for providing counseling and guidance whenever the need arose.

I have been fortunate to interact with many gifted individuals during my stay at MIT. I am grateful to Ehud (“Udi”) Yariv, formerly a postdoc in the Brenner group, for many insightful discussions on the kinetic theory of gases and fluid mechanics, and to Jim Bielenberg, another former member of the Brenner group, for helpful discussions on research and coursework. It has been a privilege to interact with all members of the Doyle group, past and present – Greg, Ju Min, Patrick, Ramin and Thierry (whom I was fortunate to have known briefly while they were at MIT), Anthony, Chih-Chen, Dan and Dhananjay, as well as the newest members, Daniel, Jason, Jing, Panda, Rilla and Wui Siew. In particular, Ramin generously provided the code used in this thesis for the generation of magnetic colloid assemblies, and answered my many queries regarding these

systems. I thank the members of the Armstrong group, Dave, Kate, Micah, Theis and Zubair, and also Minggang of the Brown group, for their generosity in sharing their office with me over the past few years. In addition, I am grateful for the friendship of many others within and outside MIT.

Finally, I am very grateful to my parents for their endless and unflinching support. I learnt my first lessons in calculus, linear algebra, stochastic processes and numerous other subjects from my father, whose guidance put me on the path to research. The motivation and encouragement I receive from my parents and many other relatives has always been invaluable, for which I am thankful.

---

# Table of Contents

---

<b>Abstract</b>	<b>3</b>
<b>Chapter 1 Introduction</b>	<b>19</b>
1.1 Fluid Dynamics in Inhomogeneous Fields . . . . .	19
1.1.1 <i>Slow, Nonisothermal Gas Flows</i> . . . . .	19
1.1.2 <i>Specific Objectives and Overview of Results</i> . . . . .	24
1.1.3 <i>Applicability to Phoretic Transport in Liquids</i> . . . . .	24
1.2 Dynamics of an Electric-Field Driven Polymer Chain . . . . .	25
1.2.1 <i>Motivation and Objectives</i> . . . . .	25
1.2.2 <i>Coarse-Grained Modeling</i> . . . . .	28
1.2.3 <i>Brownian Dynamics</i> . . . . .	34
1.2.4 <i>Overview of Results</i> . . . . .	37
<b>Chapter 2 An Extension of Faxen's Laws for Nonisothermal Flow Around a Sphere</b>	<b>39</b>
2.1 Derivation of Faxen's Laws with Account for Thermal Slip . . . . .	39
2.2 Applications . . . . .	42
2.3 Extension to Electrophoresis . . . . .	43

<b>Chapter 3</b>	<b>Thermophoretic Motion of a Slightly Deformed Sphere Through a Viscous Fluid</b>	<b>45</b>
3.1	Introduction . . . . .	45
3.2	Problem Formulation . . . . .	46
3.3	Temperature Fields . . . . .	48
3.4	Flow Field . . . . .	50
3.5	Nonisothermal Flow around an Ellipsoid . . . . .	51
3.6	Discussion . . . . .	56
<b>Chapter 4</b>	<b>Unraveling of a Tethered Polymer Chain in Uniform Solvent Flow</b>	<b>57</b>
4.1	Introduction . . . . .	57
4.2	Problem Definition and Methodology . . . . .	59
4.3	The Rouse Model . . . . .	60
4.4	The Wormlike Chain Model . . . . .	63
4.5	Tension Propagation . . . . .	68
4.6	Discussion . . . . .	78
<b>Chapter 5</b>	<b>Stochastic Modeling and Simulation of DNA Electrophoretic Separation in a Microfluidic Obstacle Array</b>	<b>83</b>
5.1	Introduction . . . . .	83
5.2	CTRW Model of Chain Dynamics . . . . .	85
5.3	Brownian Dynamics Simulations . . . . .	89
	5.3.1 <i>Chain Simulations</i> . . . . .	89
	5.3.2 <i>Selection of Array Geometries</i> . . . . .	91
5.4	Comparison of Model Predictions and Simulation Results . . . . .	93
	5.4.1 <i>Varying Field Strengths</i> . . . . .	93
	5.4.2 <i>Varying Mean Lattice Spacings</i> . . . . .	101
5.5	Discussion . . . . .	103
<b>Chapter 6</b>	<b>Conclusions and Outlook</b>	<b>113</b>
6.1	Fluid Dynamics in Inhomogeneous Fields . . . . .	113
6.2	DNA Dynamics in Microfluidic Separation Devices . . . . .	114
<b>Appendix A</b>	<b>Parameter Estimation for Brownian Dynamics Simulation of <math>\lambda</math>-DNA with Hydrodynamic Interactions</b>	<b>117</b>
A.1	Simulation Procedure . . . . .	117
A.2	Code Validation . . . . .	120
A.3	Parameter Determination . . . . .	121
<b>Appendix B</b>	<b>Nonisothermal Flow Around an Ellipsoid</b>	<b>123</b>
B.1	$O(\epsilon)$ Temperature Field . . . . .	123
B.2	Derivation of $\mathbf{K}^{(1)}$ . . . . .	125
<b>Appendix C</b>	<b>Normal Mode Analysis of a Tethered Rouse Chain</b>	<b>127</b>
C.1	Normal Mode Solution . . . . .	127
C.2	Continuous Approximation . . . . .	130





---

## *List of Figures*

---

1.1	Sequencing of DNA by gel electrophoresis. . . . .	26
1.2	Formation of a hooked chain configuration in an array of obstacles . . . . .	27
1.3	Space curve representation of a wormlike chain . . . . .	32
1.4	Bead-spring model . . . . .	33
4.1	Fractional extension and tension in the first spring as functions of the rescaled time coordinate $\tilde{t}/N^2$ for Rouse chains of several lengths $N$ at a Peclet number of 1. . . . .	62
4.2	Tension profiles for Rouse chains of 41 and 61 beads as functions of the rescaled spring index $(2k - 1)/(2N - 1)$ at a Peclet number of 1 at several points in time. . . . .	63
4.3	Fractional extension as a function of time for 61-bead Rouse chains and wormlike chains (abbreviated WLC) at Peclet numbers of 1 and 100. . . . .	64
4.4	Tension in the first spring as a function of time for 61-bead Rouse and wormlike chains at Peclet numbers of 1 and 100. . . . .	65
4.5	Fractional extension as a function of time nondimensionalized by the convective time scale $L/v$ for a 61-bead wormlike chain at several values of the Peclet number. . . . .	66
4.6	Spring extension in the flow direction, $\tilde{Q}_{\text{spr } k, x}$ , plotted against time for several springs of a 61-bead wormlike chain at Peclet numbers of 10 and 100. . . . .	67
4.7	Fractional extension as a function of $\tilde{t}/N^2$ for wormlike chains of several lengths at Peclet numbers of 1, 10 and 100. . . . .	69

4.8	Tension in the first spring as a function of $\tilde{t}/N^2$ for wormlike chains of several lengths at Peclet numbers of 1, 10 and 100. . . . .	70
4.9	Tension profiles for wormlike chains of 41 and 61 beads as functions of the rescaled spring index $k/N$ at several points in time, compared at equal values of the rescaled time coordinate $\tilde{t}/N^2$ for both chain sizes at two values of the Peclet number. . . . .	71
4.10	Spring tension as a function of spring index $k$ for 61-bead Rouse and wormlike chains at a Peclet number of 100 at times $\tilde{t} = 0.05$ and $\tilde{t} = 2$ . . . . .	72
4.11	Spring tension as a function of spring index $k$ for a 61-bead Rouse chain at a Peclet number of 100 and at time $\tilde{t} = 2$ . . . . .	73
4.12	Tension propagation in Rouse chains at a Peclet number of 1. . . . .	74
4.13	Rescaled spring force $\tilde{F}_{\text{spr } k, x} N/(N_{k,s} \text{Pe})$ as a function of the spring index $k$ for a 101-bead Rouse chain, and that predicted by taking the continuous limit of a semi-infinite Rouse chain. . . . .	76
4.14	Tension propagation in a 61-bead wormlike chain at a Peclet number of 100. . . . .	77
4.15	Tension propagation in a 61-bead wormlike chain at Peclet numbers of 10 and 30. . . . .	79
5.1	Normalized mobility and dispersivity of $\lambda$ -DNA as a function of $\text{Pe}_\lambda$ calculated from simulation in a regular, hexagonal array. . . . .	92
5.2	A regular, hexagonal lattice, a portion of a self-assembled array of magnetic beads from simulation, and a portion of an experimentally generated self-assembled array of magnetic beads. . . . .	94
5.3	Normalized mobility of $\lambda$ -, $2\lambda/3$ - and $\lambda/3$ -DNA as a function of the Peclet number for $\lambda$ -, $2\lambda/3$ - and $\lambda/3$ -DNA, respectively, obtained by simulation in a self-assembled array of magnetic beads, that predicted by our model, and that predicted by the model of Minc et al. . . . .	96
5.4	Normalized dispersivity of $\lambda$ -, $2\lambda/3$ - and $\lambda/3$ -DNA as a function of the Peclet number for $\lambda$ -, $2\lambda/3$ - and $\lambda/3$ -DNA, respectively, obtained by simulation in a self-assembled array of magnetic beads, that predicted by our model, and that predicted by the model of Minc et al. . . . .	97
5.5	Mean distance covered between successive collisions by $\lambda$ -, $2\lambda/3$ - and $\lambda/3$ -DNA as a function of the Peclet number for $\lambda$ -, $2\lambda/3$ - and $\lambda/3$ -DNA, respectively, obtained by simulation in a self-assembled array of magnetic beads, that obtained from our model, and that obtained from the model of Minc et al. . . . .	98
5.6	Mean collision probability of $\lambda$ -, $2\lambda/3$ - and $\lambda/3$ -DNA as a function of the Peclet number for $\lambda$ -, $2\lambda/3$ - and $\lambda/3$ -DNA, respectively, obtained by simulation in a self-assembled array of magnetic beads, that assumed by our model, and that assumed by the model of Minc et al. . . . .	99
5.7	Dispersivity of $\lambda$ -, $2\lambda/3$ - and $\lambda/3$ -DNA normalized with respect to the free solution diffusion coefficient of a free draining chain as a function of the Peclet number for $\lambda$ -, $2\lambda/3$ - and $\lambda/3$ -DNA, respectively, obtained by simulation in a self-assembled array of magnetic beads. . . . .	105
5.8	Separation resolution between $\lambda$ - and $\lambda/3$ -DNA, $\lambda$ - and $2\lambda/3$ -DNA, and $\lambda/3$ - and $2\lambda/3$ -DNA as a function of $\text{Pe}_\lambda$ calculated by simulation in a self-assembled array of magnetic beads, that predicted by our model, and that predicted by the model of Minc et al. . . . .	106

5.9	Normalized mobility of $\lambda$ -, $2\lambda/3$ - and $\lambda/3$ -DNA as a function of the mean lattice spacing obtained by simulation in a self-assembled array of magnetic beads, that predicted by our model, and that predicted by the model of Minc et al. . . . .	107
5.10	Normalized dispersivity of $\lambda$ -, $2\lambda/3$ - and $\lambda/3$ -DNA as a function of the mean lattice spacing obtained by simulation in a self-assembled array of magnetic beads, that predicted by our model, and that predicted by the model of Minc et al. . . . .	108
5.11	Mean distance covered between successive collisions by $\lambda$ -, $2\lambda/3$ - and $\lambda/3$ -DNA as a function of the mean lattice spacing obtained by simulation in a self-assembled array of magnetic beads, that obtained from our model, and that obtained from the model of Minc et al. . . . .	109
5.12	Mean collision probability of $\lambda$ -, $2\lambda/3$ - and $\lambda/3$ -DNA as a function of the mean lattice spacing obtained by simulation in a self-assembled array of magnetic beads, that predicted by our model, and that predicted by the model of Minc et al. . . . .	110
5.13	Separation resolution between $\lambda$ - and $\lambda/3$ -DNA, $\lambda$ - and $2\lambda/3$ -DNA, and $\lambda/3$ - and $2\lambda/3$ -DNA as a function of the mean lattice spacing calculated by simulation in a self-assembled array of magnetic beads, that predicted by our model, and that predicted by the model of Minc et al. . . . .	111



---

## *List of Tables*

---

A.1	Time taken per $10^4$ steps for the simulation of a single chain of $N$ beads with hydrodynamic interactions on a 1.7 GHz processor . . . . .	120
A.2	Parameter dependence of results obtained from Brownian dynamics simulation of $\lambda$ -DNA with hydrodynamic interactions . . . . .	121



# *Introduction*

---

The first part of this thesis investigates dynamical effects in fluids animated by the presence of potential gradients, where the role of potential may be played by a temperature, concentration, or an electric potential field. Chapters 2 and 3 pertain to this subject, which is described in greater detail in Section 1.1.

The subject of the second part of this thesis comprises the dynamics of charged polymers under the imposition of an electric field, with applications to DNA dynamics in size-based separation devices. These issues are elaborated in Chapters 4 and 5, and below in Section 1.2.

## 1.1 Fluid Dynamics in Inhomogeneous Fields

### 1.1.1 *Slow, Nonisothermal Gas Flows*

#### *Hydrodynamic Equations*

The solution of the classical equations of motion, applied individually to each molecule of a fluid concurrently with the imposition of momentum and energy conservation during molecular encounters, is usually beyond the ambit of computational feasibility over spatial and temporal scales of interest. The derivation of coarse-grained equations offers a great simplification over the detailed molecular picture, both computationally and conceptually. For the special case of a dilute, weakly-interacting gas, the coarse-graining of the reversible, Newtonian equations of motion was

performed by Ludwig Boltzmann in 1872 to yield the irreversible Boltzmann kinetic equation for the one-particle probability density function  $f_1(\mathbf{c}, \mathbf{r}, t)$  [1], namely

$$\frac{\partial f_1}{\partial t} + \mathbf{c} \cdot \frac{\partial f_1}{\partial \mathbf{r}} + \mathbf{F} \cdot \frac{\partial f_1}{\partial \mathbf{c}} = \left. \frac{\partial f_1}{\partial t} \right|_{\text{coll}} \quad (1.1)$$

where  $\mathbf{c}$  and  $\mathbf{r}$  denote, respectively, the velocity and position of the gas molecule at time  $t$ , while  $\mathbf{F}$  denotes the net external force acting on the gas molecules. The term  $(\partial f_1 / \partial t)|_{\text{coll}}$  denotes the change in  $f_1$  occurring due to collisions. Details of the intermolecular potential of interactions among the gas molecules are contained within this term.

In obtaining the Boltzmann equation, only short range two-body interactions among the gas molecules are accounted for. Moreover, in considering encounters between two gas molecules, it is assumed that both molecules are distributed at random, and without any correlation between velocity and position. This latter assumption, referred to as the ‘‘assumption of molecular chaos,’’ is justifiable at distances large compared to the range of the two-body interaction potential. In consequence of this assumption, the Boltzmann equation is valid only at length and time resolutions larger than those of a two-body collision. The length scale associated with short range intermolecular interactions is typically of the order of the atomic size, namely,  $10^{-10}$  m. The typical speed of a gas molecule at room temperature is of the order of  $10^2$  m/s, whereby the associated time scale is of order  $10^{-12}$  s.

The laws asserting the conservation of the local mass, momentum and energy follow from the Boltzmann equation, owing to the fact that the aforementioned conserved quantities are left unchanged by two-body collisions. The conservation equations, collectively known as the hydrodynamic equations [1], refer to the following continuity, momentum and internal energy equations:

$$\begin{aligned} \frac{\partial \rho}{\partial t} + \nabla \cdot (\rho \mathbf{v}) &= 0 \\ \rho \frac{\partial \mathbf{v}}{\partial t} + \rho \mathbf{v} \cdot \nabla \mathbf{v} &= -\nabla \cdot \mathbf{P} + \mathbf{F}_v \\ \rho \frac{\partial \epsilon}{\partial t} + \rho \mathbf{v} \cdot \nabla \epsilon &= -\nabla \cdot \mathbf{q} - \mathbf{P} : \nabla \mathbf{v} \end{aligned} \quad (1.2)$$

where we have introduced the pressure tensor  $\mathbf{P}$  and the heat flux vector  $\mathbf{q}$ , given by the respective expressions  $\mathbf{P} = \delta P + \boldsymbol{\tau} = \rho \langle \mathbf{C}\mathbf{C} \rangle$  and  $\mathbf{q} = \rho \langle \mathbf{C}\mathbf{C}^2 \rangle / 2$ , where  $\delta$  denotes the identity tensor,  $P$ , the hydrostatic pressure,  $\boldsymbol{\tau}$ , the stress tensor,  $\rho$ , the local gas density, and  $\mathbf{C} = \mathbf{c} - \langle \mathbf{c} \rangle$ , the local gas velocity with respect to its mean, having magnitude  $C$  [1]. The symbol  $\mathbf{F}_v$  represents the external force per unit volume acting on the gas,  $\epsilon = \langle C^2 / 2 \rangle$  denotes the local average kinetic energy per unit mass of the gas molecule, and  $\mathbf{v} \equiv \langle \mathbf{c} \rangle$ , the local mean gas velocity. The angular brackets represent an averaging over momentum space with respect to the normalized one-particle density function.

### *Kinetic Derivation of Constitutive Equations*

The hydrodynamic equations entail the specification of constitutive relations for the stress tensor  $\mathbf{P}$  and the heat flux vector  $\mathbf{q}$ , and the boundary conditions to be applied at the fluid–solid boundary. The kinetic derivation of the constitutive relations necessitates knowledge of at least an approximate solution for the one-particle density  $f_1$  from the Boltzmann equation.

The derivation of constitutive expressions from the Boltzmann equation is facilitated by the introduction of the Knudsen number, denoted by  $\text{Kn}$ , representing the ratio of the mean free path of the gas to the macroscopic length scale. The mean free path of a gas molecule under conditions of standard temperature and pressure is of order  $10^{-7}$  m, and is typically far exceeded by macroscopic length scales, resulting in the inequality  $\text{Kn} \ll 1$ . The one-particle density  $f_1$  may then be expanded as an asymptotic series in the Knudsen number. This solution technique, valid in the continuum limit  $\text{Kn} \ll 1$ , is due to Chapman and Enskog [1]. The equations obtaining at  $O(1)$  from the Chapman–Enskog expansion are the inviscid Euler equations, with  $f_1$  being identical to the equilibrium, Maxwellian distribution at  $O(1)$ . The Navier–Stokes and Fourier constitutive laws follow at  $O(\text{Kn})$ , having the respective forms  $\tau_{\text{NS}} = -2\mu\overline{\nabla\mathbf{v}}$  and  $\mathbf{q} = -k\nabla T$ , where  $\mu$  denotes the gas viscosity,  $k$ , the thermal conductivity, and  $T$ , the temperature of the gas. The viscosity and thermal conductivity are determined by the nature of intermolecular interactions among the gas molecules. The overbar denotes the traceless, symmetric form of the tensor it surmounts. The equations obtained at  $O(\text{Kn}^2)$  are known as the Burnett equations [1].

However, it has been pointed out by Kogan et al. [2] that the Chapman–Enskog expansion presupposes the magnitude of the gas velocity to be of the same order as the speed of sound. The Knudsen number may be expressed as the ratio  $\text{Ma}/\text{Re}$ , where  $\text{Re}$  denotes the Reynolds number and  $\text{Ma}$  the Mach number, representing the ratio of the magnitude of the gas velocity to the speed of sound. Thus, the inequality  $\text{Kn} \ll 1$  is satisfied in two cases: (1)  $\text{Ma} \sim O(1)$ ,  $\text{Re} \gg O(1)$ , and (2)  $\text{Ma} \ll O(1)$ ,  $\text{Re} \sim O(1)$ . The Chapman–Enskog expansion is valid in the former case wherein  $\text{Ma} \sim O(1)$  and  $\text{Re} \gg O(1)$  [2]. The alternative case where  $\text{Ma} \ll O(1)$  and  $\text{Re} \sim O(1)$  was considered by Kogan et al. [2], who demonstrated that, in this limit, certain terms typically considered to be of higher order than the Navier–Stokes stress tensor, namely, the Burnett thermal stresses, reduce to the same order as the Navier–Stokes equations and must be considered alongside the Newtonian viscous stress tensor of the Navier–Stokes equations. The Burnett thermal stress term is of the form  $\tau_{\text{thermal}} = \omega_3\mu^2/(\rho T)\overline{\nabla\nabla T} + \omega_5\mu^2/(\rho T^2)\overline{\nabla T\nabla T}$ , where  $\omega_3$  and  $\omega_5$  are constants determined by the law of interactions among the gas molecules. The existence of thermal stresses at the same order as the Newtonian viscous stress tensor was in fact noted even earlier by Maxwell [3] in his study on the stresses arising from inequalities of temperature in a rarefied gas. An analogue of the  $H$  theorem (which proves the existence of an irreversibly-increasing quantity that may be identified with the entropy, consistent with the second law of thermodynamics) has recently been established for the modified equations with the inclusion of the thermal stresses in the momentum equation [4].

### *Kinetic Derivation of Boundary Conditions*

We now turn to the specification of boundary conditions. The no-slip boundary condition, conventionally applied to the velocity of a gas at the surface of a solid, asserts equality of the tangential gas and solid velocities at the interface. However, under nonisothermal flow conditions, this boundary condition is known to yield predictions that are inconsistent with experimental observations. For instance, the no-slip hypothesis, when used in conjunction with the Navier–Stokes equations, fails to explain the phenomenon of thermal transpiration, first observed by Reynolds [5] in 1879, involving the existence of a steady-state pressure gradient in a gas contained in a closed insulated capillary tube whose ends are maintained at different temperatures; rather, a vanishing gas velocity, and, hence, a uniform pressure, are incorrectly predicted to exist throughout the gas.

Another phenomenon that the no-slip condition is unable to explain is thermophoresis [6–8], representing the experimentally-observed movement of a solid particle in a laterally-unbounded gas confined between opposing plane walls maintained at different temperatures, the particle motion being from the hot towards the cold wall. Tyndall’s observation in 1870 [7] of the movement of dust particles away from heated surfaces is a manifestation of this phenomenon.

These observations have motivated attempts to derive the continuum boundary conditions from kinetic theory. As discussed by Kogan [9], in order to arrive at the continuum boundary conditions to be imposed on the gas velocity at the solid surface, the Boltzmann equation must be solved both inside the Knudsen layer spanning a thickness of the order of the mean free path proximate to the surface, as well as in the bulk gas. In effecting the asymptotic solution of the Boltzmann equation, the relevant length scale in the inner, Knudsen layer is the mean free path, whereas that in the outer, bulk gas is the macroscopic length scale. The boundary condition at the solid boundary is such that some fraction of the gas molecules incident on the boundary is typically reflected diffusely, i.e., the reflected gas molecules are in thermal equilibrium. The subsequent matching of these inner and outer solutions at the outer limit of the Knudsen layer yields the velocity and temperature boundary conditions to be imposed on the continuum hydrodynamic equations governing the velocity and temperature in the bulk gas. The difference between the boundary condition on velocity thereby obtained and the velocity of the wall arises due to thermal slip. It was established by Kogan et al. [2] that the thermal slip condition reduces to the same order as the Navier–Stokes equations, and, hence, replaces the conventional no-slip boundary condition in the simultaneous limits  $Ma \ll O(1)$  and  $Re \sim O(1)$ . Temperature jump, arising from the inequality of the temperature at the outer limit of the Knudsen layer and the temperature at the wall, as well as viscous slip proportional to the normal gradient of the tangential gas velocity, have also been established to occur, but are of higher order than the Navier–Stokes equations in the situation under consideration [2].

Various derivations of the thermal slip condition are summarized in Ref. [10], with the form of the resulting boundary condition being given by the expression

$$\mathbf{v} - \mathbf{U} = \beta \frac{\mu}{\rho T} (\boldsymbol{\delta} - \hat{\mathbf{n}}\hat{\mathbf{n}}) \cdot \nabla T \quad (1.3)$$

on the solid boundary, where  $\mathbf{U}$  denotes the wall velocity, and  $\hat{\mathbf{n}}$ , the unit normal to the surface. The constant  $\beta$  is an  $O(1)$  constant governed by the details of the interactions of the gas molecules among themselves and with the solid surface. Typical values of the slip coefficient  $\beta\mu/(\rho T)$  are of order  $10^{-7} \text{ m}^2\text{s}^{-1}\text{K}^{-1}$  for a gas on average at room temperature. Note that Equation 1.3 automatically satisfies the condition  $\hat{\mathbf{n}} \cdot (\mathbf{v} - \mathbf{U}) = \mathbf{0}$  that the solid be impermeable to mass flow through its surface.

An earlier derivation of the slip condition due to Maxwell in 1879 [3] was aimed at explaining the development of a thermomolecular pressure gradient in Reynolds’ [5] thermal transpiration experiment. For a gas of Maxwellian molecules (i.e., molecules that behave as point centers of repulsion, with the repulsive force between two molecules being inversely proportional to the fifth power of the distance between them), the thermal slip condition of Maxwell is identical in form to Equation 1.3, with the coefficient  $\beta = 3/4$  [3]. However, because Maxwell’s derivation of the thermal slip condition assumes the distribution function of the gas molecules in the Knudsen layer to be the same as that in the bulk gas, the 3/4 coefficient is subject to some uncertainty, as pointed out by Maxwell himself [3].

The reduction of Burnett terms previously supposed to be  $O(Kn)$  higher than the Navier–Stokes

equations has also been found to occur in the presence of concentration gradients, resulting in concentration-stress convection and the concomitant concentration-gradient induced slip condition [11]. However, these terms have been found, even for a binary mixture of monatomic gases, to be complicated functions of the composition of the gas mixture and the interaction potential between the individual components of the mixture.

While all of the preceding results derive from the kinetic theory of dilute gases, their generalization to dense gases and liquids is unavailable. Whereas the Boltzmann equation assumes that molecules interact solely through uncorrelated binary collisions, dynamic molecular correlations in dense fluids extend over length scales at least as large as the mean free path. In fact, the expansion of the transport coefficients in powers of density (analogous to the virial expansion) has been found to diverge in the case of dense gases or liquids, owing to the divergence of the mean free path in the limit  $\rho \rightarrow 0$  [12].

### *Governing Equations of Slow, Nonisothermal Gas Flow*

Further simplifications arise in situations where  $\Delta T/T$  is sufficiently small, with  $\Delta T$  the temperature difference across the gas, as follows. It is evident from Equation 1.3 that the characteristic velocity of gas flow induced by thermal slip scales with the ratio of its kinematic viscosity  $\mu/\rho$  to the length scale  $L \equiv \|\nabla \ln T\|^{-1}$  of the externally imposed temperature variation, wherein the modulus bars denote an appropriate norm. Thus, when  $L$  is large compared with the characteristic size, say  $a$ , of a small particle present in the gas whose surface constitutes the solid boundary, the appropriate Reynolds number  $\text{Re}$  governing the gas flow scales as  $a/L \ll 1$ . As a result, the inertial term  $\rho \mathbf{v} \cdot \nabla \mathbf{v}$  of the momentum equation proves to be negligible in comparison with the viscous term,  $\mu \nabla^2 \mathbf{v}$ . Similarly, the Peclet number  $\text{Pe} = \text{RePr}$ , with the Prandtl number  $\text{Pr}$  being  $O(1)$  for gases [1], scales as  $a/L$ , whence the convective term  $\mathbf{v} \cdot \nabla T$  of the thermal energy equation proves to be negligible in comparison with the conduction term,  $\alpha \nabla^2 T$ . Although density is a function of temperature, it is readily proved, by making use of the resulting heat conduction equation, in conjunction with the fact that  $\rho T$  is approximately constant for ideal gases when the pressure remains approximately constant throughout the gas, that the incompressible continuity equation,  $\nabla \cdot \mathbf{v} = 0$ , is valid.

In the presence of temperature gradients, the inclusion of the Burnett thermal stresses [1] alongside the Newtonian viscous stress tensor of the Navier–Stokes equations is also necessary [2]. However, as was first deduced by Maxwell, and elaborated by Galkin et al. [13], when the imposed temperature gradient is sufficiently small, such that the inertial and convective terms of the respective momentum and energy equations are negligible in comparison with the viscous and conduction terms appearing therein, the contribution of such thermal stresses to the flow vanishes. In this approximation, these stresses do not contribute to the force or torque acting on a particle immersed in the gas [13].

As a result, the equations governing  $\mathbf{v}$  are the equations of incompressible Stokes flow (where we, moreover, consider only steady or quasi-steady situations in this thesis), subject to the thermal slip boundary condition. The applicability of the Stokes equations satisfying this boundary condition to slow, nonisothermal gas flow was established by Maxwell [3] and Galkin et al. [13]. At the same time, the equations governing the temperature are the Fourier heat conduction equations applied to the gas as well as to the solid (if the latter is thermally conducting). Concomitantly, the equality of the gas and solid temperatures and heat fluxes is imposed at the boundary.

### 1.1.2 *Specific Objectives and Overview of Results*

In Chapter 2, we provide an extension of Faxen's laws for the force and torque on a rigid sphere in an arbitrary Stokes flow field to account for the occurrence of thermal slip on the solid surface. Chapter 3 treats the flow around a slightly deformed sphere translating at a uniform velocity through a fluid in the presence of an imposed temperature gradient, and demonstrates that the thermophoretic velocity of a nonconducting, force- and torque-free particle is independent of its shape, size and orientation. This finding is in agreement with the general conclusion of Morrison [14] that the phoretic velocity of a force- and torque-free particle is independent of its shape or size. Our studies have potential applications in aerosol technology, as a method of microcontamination control in the semiconductor industry, in the fabrication of optical fibers, in microgravity manufacturing processes, and in the nonisothermal transport of particulates in porous media or MEMS devices. These applications are reviewed by Zheng [8].

### 1.1.3 *Applicability to Phoretic Transport in Liquids*

While the specific problems considered in this thesis are treated in the context of gas flow around a solid particle under nonisothermal conditions, the results are also generally applicable to other situations for which the fluid is known to slip at the surface of the solid. Thermally-induced motion of solid particles is also known to occur in liquids, having been explained on the basis of osmotic pressure gradients resulting from solute particle-solvent interactions [15–18], as well as by interfacial and electrostatic screening effects [19]. It has been proposed [17] that the thermophoretic motion of a particle in a liquid may be rationalized by first deriving the velocity profile in a thin surface layer surrounding the particle, and subsequently using the limiting value of the liquid velocity thereby obtained at the outer edge of this layer as the slip condition to be imposed upon the solution of the nonisothermal Stokes flow problem of liquid flow around the particle. In fact, the transport of solid colloidal particles by phoretic processes in liquids is typically explained via the use of a linear slip condition of the form [20]

$$\mathbf{v} - \mathbf{U} = b(\boldsymbol{\delta} - \hat{\mathbf{n}}\hat{\mathbf{n}}) \cdot \nabla\phi \quad (1.4)$$

identical to Equation 1.3, where  $b$  is a slip coefficient and the field  $\phi$  may denote temperature, concentration or electric potential. Particle motion in the three cases is referred to as thermophoresis, diffusiophoresis and electrophoresis, respectively. Values of the slip coefficient  $b$  for thermophoretic particle motion in several particle-liquid systems are of order  $10^{-8}$ – $10^{-7}$   $\text{cm}^2\text{s}^{-1}\text{K}^{-1}$  [17, 21].

A distinguishing feature of phoretic transport is the existence of a scale separation between the particle's radius and the thickness of the fluid-solid interfacial region. Therefore, boundary layer analysis applied to the Stokes equations yields the velocity field at the outer edge of the interfacial region, which forms the inner boundary condition for flow in the outer fluid. As an example, consider the electrophoretic motion of a charged, electrically insulated particle in an electrolyte upon the application of a uniform unperturbed electric field [20, 22]. The fixed charge on the surface of the particle is balanced by a diffuse counterion cloud composed of ions from the electrolytic liquid. Taken together, the surface charge and the diffuse cloud constitute an electrically neutral double layer. The charge density decays in the diffuse layer away from the solid surface over a characteristic length scale referred to as the Debye length. With the assumption that the charge density relaxes to its value in the bulk according to Boltzmann statistics, the electric potential and, hence, the electric field are obtained from the solution of Poisson's equation. The asymptotic solution of the

Stokes equations with account for the body force arising from the action of the electric field on the charges in the Debye layer and in the bulk, satisfying the no-slip condition at the particle surface, yields the slip velocity to be applied at the outer limit of the inner, Debye region identical in form to Equation 1.4, with the slip coefficient  $b = \epsilon\zeta/(4\pi\mu)$ , where  $\epsilon$  is the fluid's dielectric constant and  $\zeta$ , the zeta potential at the surface, assumed constant [20]. This slip condition is to be used concomitantly with the Stokes equations (in the absence of an electric body force term) in the outer, bulk fluid.

Thus, with the use of an appropriate slip coefficient, our results may be applied to phoretic motion in liquids. The results are of potential interest in connection with applications involving phoretic transport in porous media or MEMS devices.

## 1.2 Dynamics of an Electric-Field Driven Polymer Chain

### 1.2.1 *Motivation and Objectives*

The necessity to effect the size-based separation of DNA fragments arises in applications as diverse as recombinant DNA technology, gene therapy, forensics and population genetics. In fact, the availability of rapid gene sequencing techniques was instrumental in the success of the Human Genome Project. Sequencing technologies rely on the use of chain termination methods to generate a number of small fragments from a DNA molecule, which are each terminated by a known nucleotide. This is achieved as follows. The double-stranded DNA molecule is first denatured to yield the single strands comprising the molecule. (The structure of DNA is described later in this Section.) The single-stranded DNA sample is then divided into four sub-samples, to each of which is added a mix of all four monomeric units of DNA, namely, the nucleotides A, T, G and C, and also one known nucleotide among A, T, G, and C that has been modified so that it cannot react further to generate a longer double-stranded DNA chain and, hence, terminates the chain sequence. The hybridization reaction, generating several small, double-stranded DNA fragments terminated by the known modified nucleotides, is allowed to proceed in each sub-sample. Subsequently, the four sub-samples, each containing fragments of varying sizes, are each separated into their constituent fragments based on size. The lengths of the fragments present in each sub-sample then signal the positions of the corresponding chain-terminating nucleotide added to that sample, thus revealing the sequence of the original chain. The procedure is illustrated in Fig. 1.1 below. Frequently, a long DNA molecule is treated with restriction enzymes that cut the molecule at the location of specific base sequences to form shorter DNA chains, which are subsequently sequenced by means of chain termination methods, as described above.

The conventional technique for achieving the size-based separation of DNA fragments, namely, gel electrophoresis, involves the size-dependent motion of the negatively charged DNA molecules through a gel upon the application of a constant electric field. The interactions of the DNA chain with the gel are size-dependent, and the retardation of the molecule by the gel increases with the size of the molecule. The gels most commonly used to effect the separation of DNA chains are polyacrylamide and agarose [23].

Typically, gel electrophoresis employs gels having a mean pore size smaller than the radii of gyration of the chains. The mechanism of chain motion, therefore, involves the snake-like motion of the chain through the gel upon the imposition of an electric field. This mechanism was termed reptation by de Gennes [23,24]. A severe limitation of this technique, however, is that the mobility

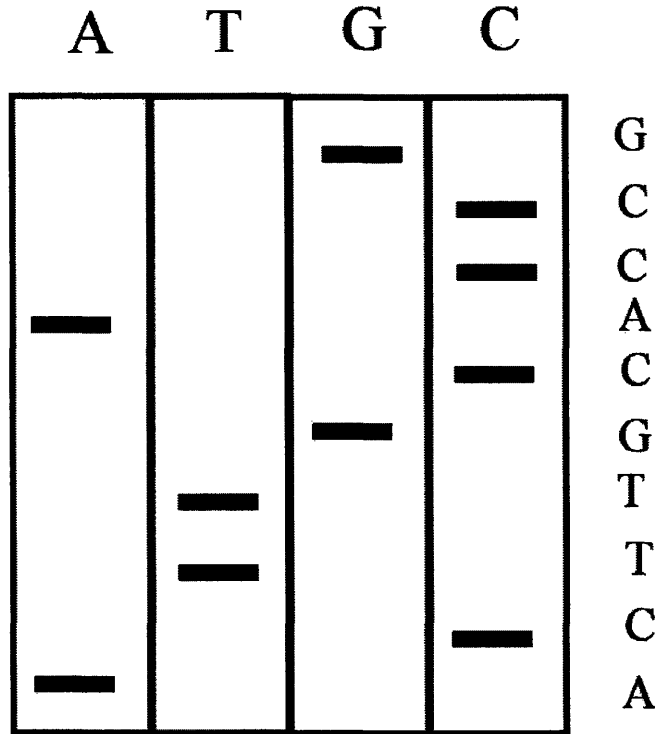


Figure 1.1: *Sequencing of DNA by gel electrophoresis.*

of long DNA chains through the gel saturates at an upper bound independent of chain size. This behavior owes itself to the fact that the flexible DNA molecule loses its coiled conformation when driven by a strong field through gel channels whose pore sizes are smaller than the size of the DNA coil. Under the application of a constant electric field, the chain becomes aligned in the field direction, whereby its electrophoretic mobility becomes independent of size. An upper limit of typically a few tens of kilobase pairs is, consequently, imposed on the chain lengths that can be separated via gel electrophoresis [23].

The above limitation of gel electrophoresis has stimulated the development of several techniques that attempt to avoid this drawback. These include pulsed-field gel electrophoresis, entropic trapping and obstacle-course based separation [23]. Size-based separation has also been achieved via dilute solution capillary electrophoresis, wherein a dilute solution of neutral polymer chains is used as the separation medium [25,26]. The separation is induced by the size-dependent entanglement of the DNA molecules with the neutral host polymer chains [27,28]. These, as well as related studies on the electrophoretic separation of DNA molecules, are discussed in the review of Viovy [23].

Obstacle-course based separation devices entail the electrophoresis of the DNA chains through a microchannel enclosing an array of obstacles. The size specificity of this separation technique arises from the fact that a larger polymer coil is more likely to collide with an obstacle, and once a collision has occurred, a longer chain requires more time for its disengagement from the obstacle than a shorter chain. Consequently, a longer chain requires more time to traverse the array relative to a shorter chain. A high separation resolution between two chain sizes is achieved when a large difference exists between their transit velocities in the array, while simultaneously, both chains

exhibit low dispersivities, resulting in the occurrence of widely separated and narrowly peaked concentration profiles of the two species at the array exit. Such a separation technique was pioneered by Volkmuth and Austin [29], who employed optical microlithography to fabricate obstacle courses in silicon dioxide, and experimentally demonstrated the efficacy of the obstacle courses in separating DNA chains of varying lengths. Subsequently, Doyle et al. [30], followed by Minc et al. [31, 32], have used columns of superparamagnetic beads confined in a microfluidic channel, formed from the self-assembly of the beads upon the imposition of a magnetic field transverse to the channel plane, to separate DNA chains of different lengths driven through the channel by the application of an electric field.

Under conditions wherein the post spacing is larger than the chain sizes, separation in an array of obstacles relies on the formation of hooked chain configurations following collisions. Consequently, and in contrast to gel electrophoresis, these devices may be used to separate long DNA chains. Thus, the use of microfluidic post arrays offers an advantage over gel electrophoresis. Post arrays have also been fabricated and employed under conditions such that the post spacing is comparable to the sizes of the chains to be separated [33]. Figure 1.2 illustrates the formation of a hooked chain configuration during chain motion under an imposed electric field through a self-assembled array of magnetic beads generated by simulation.

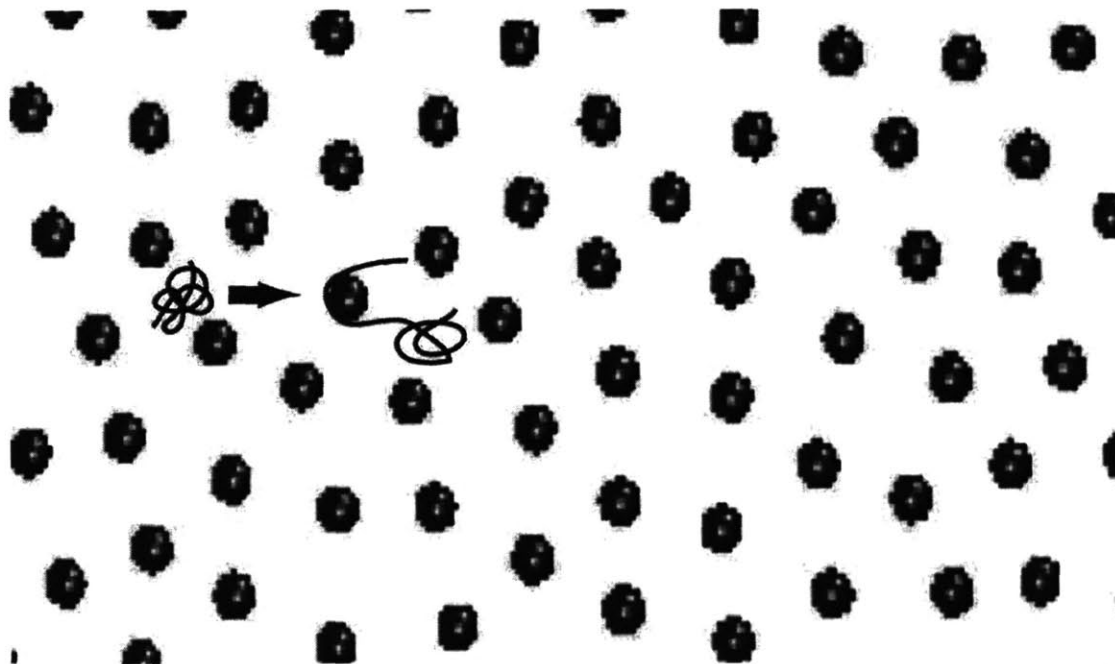


Figure 1.2: *Formation of a hooked chain configuration during chain motion induced by the imposition of an electric field through a self-assembled array of magnetic beads generated by simulation.*

The separation resolution achieved in these devices has been shown to be nonmonotonic with respect to the electric field strength and the spacing between the obstacles in an experimental

study aimed at the size separation of  $\lambda$ -DNA and  $2\lambda$ -DNA chains in a self-assembled array of magnetic beads [31]. However, the ability to predict beforehand the separation resolution yielded by the device as a function of the chain lengths, applied electric field strength and lattice spacing is lacking. The development of predictive models with this ability is clearly desirable, and is expected to facilitate the optimal design and operation of the device to achieve maximum resolution.

Recently, attempts have been made to develop predictive models of device performance. The dynamics of DNA molecules in an array of obstacles have been modeled as being equivalent to a continuous-time random walk by Minc et al. [34], followed by Dorfman [35]. These authors, however, do not fully account for the influence of the electric field strength on chain dynamics. Moreover, their models entail detailed knowledge of single chain–obstacle interactions, the probability of chain–obstacle collision, and the mechanisms of chain unraveling and unhooking subsequent to a collision. As elaborated in Chapter 5, several of their assumptions fail to accurately capture the nature of single chain–obstacle interactions.

The mechanisms of chain collision with a single obstacle have been investigated in several prior studies [36–42]. These studies provide insight into the mechanisms of chain dynamics in an obstacle array. However, the precise nature of chain unraveling or, equivalently, the transient tension propagation in the chain following its collision with an obstacle remains unknown. This issue constitutes the subject of Chapter 4. Furthermore, we make use of the aforementioned studies on collisions with single obstacles to develop an accurate continuous-time random walk model with account for the electric-field dependence of chain dynamics in the obstacle array in Chapter 5. The technique of analysis underlying the studies presented in this thesis is the method of Brownian dynamics applied to the coarse-grained bead–spring model of the polymer chain, described in Sections 1.2.2 and 1.2.3 below.

### 1.2.2 Coarse-Grained Modeling

#### *Structure and Properties of DNA*

Deoxyribonucleic acid, abbreviated DNA, is a nucleic acid comprised of two strands crosslinked via hydrogen bonding to form a double helical structure. The backbone of each strand of DNA is a linear polymer of nucleotides comprising the sugar molecule deoxyribose bonded both to a phosphate unit, as well as to one of four nitrogenous bases, namely Adenine (A), Thymine (T), Guanine (G) and Cytosine (C). The hydrogen bonding between the pairs A=T and G≡C is instrumental in the formation of the double helix, with each strand containing one base of each pair, and with the symbols = and ≡ signifying the presence of 2 and 3 hydrogen bonds, respectively. The base sequence of each stand is, therefore, complementary to that of the other.

The presence of phosphate groups in the backbone is responsible for imparting a negative charge to the DNA molecule. In solution, the DNA molecule is surrounded by a counterion cloud, with the charge surrounding the backbone decaying with distance away from the molecule over a characteristic Debye length of typically 1–3 nm in the commonly employed buffers. Hydrodynamic interactions among the DNA segments are screened over distances that are large compared to the Debye length [43]. Upon the application of an electric field, the DNA coil moves towards the positive electrode in free solution at a size-independent electrophoretic velocity. The electrophoretic mobility of DNA, defined as the velocity per unit applied electric field strength, is typically of order  $10^{-8} \text{ m}^2\text{V}^{-1}\text{s}^{-1}$  in free solution [31, 32].

In our study of DNA dynamics, as is also the case with fluid dynamics, the macroscopic behavior

of interest to us is manifest at length scales far larger than the molecular size of a monomer. In the case of DNA, a nucleotide has a size of about 0.33 nm [44]. The characteristic length scale associated with the stiffness of the DNA molecule, known as the persistence length and denoted by  $A$ , is about two orders of magnitude larger at 53 nm in vivo [45]. The double helical structure of DNA imparts a greater stiffness to the molecule than that of many industrial polymers, resulting in the relatively large value of its persistence length compared to the persistence lengths of industrial polymers, which are typically of order 1 nm. Over length scales shorter than the persistence length, the DNA backbone remains stiff, whereas at length scales large compared to the persistence length, its configuration appears to be that of a continuous, flexible chain. The fully-extended chain length (equivalently, the contour length, denoted by  $L$ ) of the DNA of bacteriophage  $\lambda$ , which infects *Escherichia coli*, is still larger at 16.5  $\mu\text{m}$ , corresponding to 48.5 kilobase pairs. This DNA molecule, commonly known as  $\lambda$ -DNA, is widely used in studies on the polymer physics of DNA, and is stained with TOTO or YOYO dye for ease of observation in experimental studies. Stained  $\lambda$ -DNA has a contour length of about 21  $\mu\text{m}$  [46]. In our studies, we use DNA chains whose sizes are at least of the order of that of  $\lambda$ -DNA. The global configuration of these long DNA chains does not exhibit a significant dependence on the chemical structure of the monomeric units.

In solution under equilibrium conditions, the size of a DNA coil is far smaller than the contour length of the fully-extended chain. The relevant length scale characterizing the equilibrium size is the radius of gyration of the polymer coil in solution, denoted  $R_g$ . Under good solvent conditions, wherein intrachain repulsive interactions dominate over chain-solvent repulsion, thereby resulting in a net swelling of the coil, the experimentally measured radius of gyration of  $\lambda$ -DNA is 0.69  $\mu\text{m}$  [47]. The coil size of DNA is, hence, about an order of magnitude larger than the persistence length. Owing to this separation of local and global length scales in DNA and several other polymers, many global configurational properties exhibit universal behavior for a large class of polymers. The issue of universality is explored further below.

### *Universality and Scaling Laws*

At global length scales, large compared to the size of individual monomers, the properties of many polymers have been found to obey universal scaling laws dependent on macroscopic characteristics such as chain length and concentration [24]. These scaling laws are derivable from simple models of the polymer.

As an illustration, consider the structure of polyethylene, comprised of the repeating unit  $-\text{CH}_2-\text{CH}_2-$ . The molecule can be approximated by a freely rotating chain of rods of fixed length representing the bonds between consecutive carbon atoms, with the valence angle between two adjacent C—C bonds being held constant at the tetrahedral angle of  $\theta \approx 110^\circ$ . The next bond in the sequence may rotate freely, while keeping the valence angle  $\theta$  fixed, thereby tracing the surface of a cone whose base is orthogonal to the plane constituted by the preceding two C—C bonds. In reality, however, bond rotation is hindered by steric interactions among the methylene ( $\text{CH}_2$ ) groups, and the favorable conformations are those in which the methylene groups attached to adjacent C atoms are in opposite (*trans*) positions [48]. The planar, zigzag, all-*trans* conformation of the molecule possesses the globally minimum energy, while two local minima in energy exist for so-called *gauche* conformations. The time scale of order  $10^{-11}$  s taken to transition between the two states is much smaller than the macroscopic time scales of interest [24]. An even simpler picture of the molecule is that of a hypothetical freely jointed chain consisting of  $N_k$  rigid links of length

$b_k$  joined in linear sequence, with no restrictions on the angle between any two adjacent bonds. Although real polymers do not conform to the freely jointed chain model, the global properties of a real chain with virtually fixed  $\theta$  and restricted bond rotation are known to be similar to that of a freely jointed chain, provided that  $N_k$  and  $b_k$  are appropriately related to the number and length of bonds in the molecule [24, 48, 49]. The scale  $b_k$ , which is of order 1 nm for industrial polymers, is a coarser scale than the atomic bond lengths, which are typically of order 1 Å.

The configuration of the freely jointed chain may be modeled as being equivalent to the series of unbiased steps of equal length taken by a random walker [24, 48]. The step length  $b_k$  is known as the Kuhn length. The squared radius of the polymer coil may then be equated to the mean square end-to-end distance of the path taken by the random walker, given by the expression

$$R_g^2 \sim N_k b_k^2 = (\text{constant})L \quad (1.5)$$

where, as before,  $L = N_k b_k$  is the contour length of the fully-extended molecule. Equation 1.5 does not take account of the self-avoidance disallowing the polymer segments from crossing each other, and describes a “phantom” chain. The corresponding solvent condition is that of a  $\Theta$  solvent, with intrachain repulsion exactly balancing chain–solvent repulsion.

A model representative of a chain in a good solvent, wherein intrachain repulsion exceeds chain–solvent repulsion, is the self-avoiding random walk, possessing the scaling behavior

$$R_g^2 = (\text{constant})L^{2\nu} \quad (1.6)$$

The scaling exponent  $\nu$  depends on the dimensionality of space. The pioneering derivation of  $\nu$  is due to Flory [24, 48], who utilized scaling arguments based on the balance between entropic elasticity and intrachain excluded volume repulsion to arrive at the value  $\nu = 3/(d + 2)$ , where  $d$  denotes the dimensionality of space. Numerical simulations [24] and renormalization group calculations [50] confirm Flory’s predictions. Flory’s result is known to be exact for  $d = 1$ , while his values for  $d = 2$  and  $d = 3$  are within 1% of numerical results [24]. Equation 1.6 reduces to Equation 1.5 for  $\nu = 0.5$  in a  $\Theta$  solvent.

The scaling laws expressed by Equations 1.5 and 1.6 are obeyed by a wide range of polymers including DNA in  $\Theta$  and good solvents, respectively. Note, however, that the universality of polymer behavior lies in the scaling exponent  $\nu$ , whereas the prefactor is dependent on the molecular structure of the individual polymer.

Another universal aspect of polymer behavior is the functional form of the relation between the extension of a polymer in response to a pulling force acting on its ends and the magnitude of the pulling force, when the extension is small compared to the length of the polymer. The force–extension behavior of a freely jointed chain in the limit of small chain extension and for  $N_k \gg 1$  is given by linear Hooke’s law behavior, with the associated potential function being quadratic. Such a chain possessing linear force–extension behavior is known as a Gaussian chain in view of the Gaussian distribution of its end-to-end vector. A Gaussian chain exhibits an increasingly larger extension when it is acted upon by a stretching force of increasing magnitude, and is clearly not representative of a polymer chain of finite length under the application of a large force. The Gaussian model is most accurate under near-equilibrium conditions corresponding to the application of a force that is weak in comparison with the magnitude of the thermal force acting on the chain. A DNA chain is better represented as a continuous space curve rather than as a freely jointed chain; however, at low extensions, it, too behaves as a Gaussian chain. These issues are discussed further

below.

### *Bead-Rod Model*

The bead-rod model is founded on the notion of a freely jointed chain representing an unbiased random walk. This model well approximates many industrial polymers. In the bead-rod model, each rod represents a step of size  $b_k$  taken by the random walker. The extension of the bead-rod chain in response to a stretching force applied to its ends is described by the inverse Langevin force law [48]. In the limit of large extension,  $\mathcal{L} \lesssim L$ , where  $\mathcal{L}$  denotes the chain extension, the fractional extension  $\mathcal{L}/L$  of the bead-rod chain exhibits the dependence  $1 - \mathcal{L}/L \sim 1/F$  on the magnitude of the pulling force  $F$  [51].

The freely jointed chain model describes many industrial polymers accurately. However, as mentioned earlier in this Section, the double helical structure of DNA renders it stiffer than most industrial polymers. The large force behavior of DNA, in contrast to that of the bead-rod model, is of the form  $1 - \mathcal{L}/L \sim 1/\sqrt{F}$  [52]. The force-extension behavior of DNA is better approximated by the wormlike chain model, which is described later in this Section. However, the gross conformation of a wormlike chain whose length is large compared to its persistence length is known to be equivalent to that of a freely-jointed chain having a Kuhn step that is twice the persistence length of the wormlike chain [49]. Consequently,  $b_k = 0.106 \mu\text{m}$  for DNA. The bead-rod model has been used in previous computational studies of DNA dynamics, such as that of Ref. [53]. In this thesis, we instead employ the further coarse-grained (and consequently, less computationally expensive) bead-spring model, also elaborated later in this Section.

### *Wormlike Chain Model*

The wormlike chain model, also known as the Kratky-Porod model, treats the DNA molecule as a continuous space curve and derives its force-extension behavior from the bending stiffness of the chain [50]. The curve is parameterized by the arc length  $s$  measuring the distance along the curve from the origin to any point  $\mathbf{r}(s)$  on the curve. The wormlike chain model is illustrated in Figure 1.3. The symbol  $\mathbf{t}$  denotes the normalized tangent vector drawn to the curve at  $\mathbf{r}(s)$ , as given by the expression

$$\mathbf{t} = \frac{\partial \mathbf{r} / \partial s}{|\partial \mathbf{r} / \partial s|} \quad (1.7)$$

The characteristic length scale of decay in correlations in the tangential direction of the space curve is termed the persistence length, as intimated earlier in this Section. The persistence length  $A$  is, hence, defined by the equation

$$\langle \mathbf{t}(s) \cdot \mathbf{t}(s') \rangle = \exp\left(-\frac{|s - s'|}{A}\right) \quad (1.8)$$

where  $s$  and  $s'$  denote any two points on the curve, and the angular brackets entail the averaging over all chain configurations beginning at  $s = 0$  and terminating at  $s = L$ .

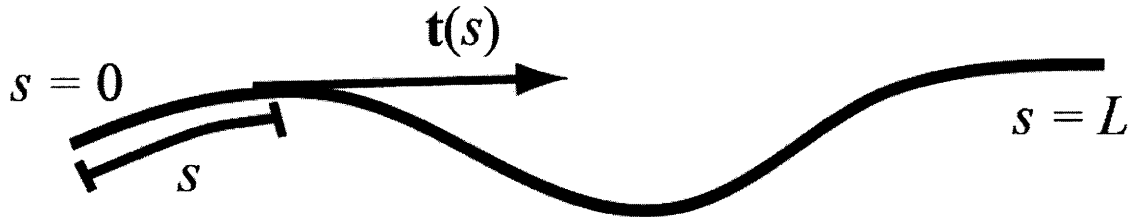


Figure 1.3: *The wormlike chain model represented as a space curve with contour length  $L$  parameterized by the arc length  $s$ , with  $\mathbf{t}(s)$  denoting the unit tangent vector drawn to the curve at  $s$ .*

The bending potential  $U$  of the wormlike chain is given by the expression

$$U = \frac{\kappa}{2} \int_0^L ds \left| \frac{\partial \mathbf{t}}{\partial s} \right|^2 \quad (1.9)$$

where the bending stiffness  $\kappa$  is expressed in terms of the persistence length  $A$  by the relation  $\kappa = k_B T A$ , where  $k_B$  and  $T$  denote, respectively, Boltzmann's constant and the solvent temperature [50, 52]. The response of the wormlike chain to a pulling force of magnitude  $F$  derives from the bending potential of Equation 1.9. However, no closed-form analytical relation exists between the force  $F$  applied to the ends of the molecule and the fractional chain extension  $\mathcal{L}/L$ , with  $\mathcal{L}$  the extension of the molecule in the direction of the force. Instead, the force–extension relation is commonly approximated by the following interpolation formula due to Marko and Siggia [52]:

$$\frac{FA}{k_B T} = \frac{\mathcal{L}}{L} - \frac{1}{4} + \frac{1}{4(1 - \mathcal{L}/L)^2} \quad (1.10)$$

Under conditions of weak stretching such that  $\mathcal{L}/L \ll 1$ , the Marko–Siggia law yields Hooke's law force–extension behavior given by  $FA/(k_B T) = 3\mathcal{L}/(2L)$ , corresponding to a Gaussian chain. When  $\mathcal{L}/L \lesssim 1$ , the Marko–Siggia law correctly predicts the behavior  $1 - \mathcal{L}/L \sim 1/\sqrt{F}$  characteristic of a wormlike chain acted upon by a large stretching force.

In our studies, we make use of the bead–spring model with the spring force law chosen in accordance with Equation 1.10, as detailed below.

### *Bead–Spring Model*

A still more coarse-grained model than those considered thus far is the bead–spring model of the polymer chain, in which each spring encompasses several Kuhn lengths or persistence lengths, as the case may be. The elasticity of the springs is of entropic origin, resulting from the coarse-graining over microscopic degrees of freedom, as depicted in Figure 1.4. The spring force law must be appropriately chosen so as to accurately reflect the force–extension behavior of the molecule in question.

The force–extension behavior originating from the coarse-graining of a large number of Kuhn

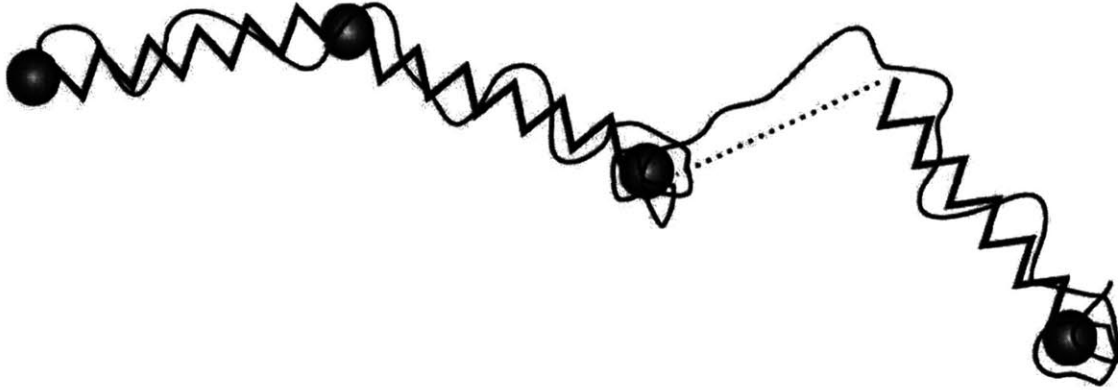


Figure 1.4: *Coarse-grained representation of a polymer molecule by a bead-spring chain.*

steps into a single spring under conditions of small chain extension is described by Hooke's law, and the associated spring potential is Gaussian [48]. However, as discussed earlier, the Gaussian chain model is inappropriate under conditions of strong stretching, and is acceptable only under near-equilibrium conditions. The spring force law most commonly employed to describe a freely jointed chain is the FENE (finitely-extensible nonlinear elastic) law, which serves as an empirical approximation to the inverse Langevin force law [54].

The representation of DNA employed in this thesis is that of the bead-spring model exhibiting the force-extension behavior of a wormlike chain, with  $N$  denoting the number of beads, and with each spring representing  $N_{k,s}$  Kuhn steps. Typically, in so doing, the force-extension behavior of each spring is represented by Equation 1.10, with the fractional chain extension  $\mathcal{L}/L$  replaced by the fractional spring extension  $Q/Q_0$ , where  $Q$  denotes the magnitude of the spring vector and  $Q_0$  the spring length at full extension. However, Underhill and Doyle [55] have noticed that errors result from the formulation of a bead-spring model with the use of the Marko-Siggia interpolation formula (which describes the global force-extension behavior of the polymer molecule stretched at constant force) to determine the force-extension behavior of each spring. These errors may be compensated in part by replacing the true persistence length with an effective persistence length in the Marko-Siggia force law. The resulting force law [55]

$$\mathbf{F}_{\text{spr}}(\mathbf{Q}) = \frac{k_B T}{2\lambda b_k} \left[ \left(1 - \frac{Q}{Q_0}\right)^{-2} - 1 + 4\frac{Q}{Q_0} \right] \frac{\mathbf{Q}}{Q} \quad (1.11)$$

is employed in this thesis. The symbols  $\mathbf{F}_{\text{spr}}$ ,  $\mathbf{Q}$  and  $\lambda$  denote, respectively, the spring tension, the spring vector of magnitude  $Q$  and the ratio of the effective to the true persistence length. The maximum spring length is given by the expression  $Q_0 = N_{k,s} b_k$ . Consequently, the contour length may be written in the form  $L = (N - 1)Q_0$ .

In Section 1.2.3 below, we describe the dynamical equations governing the behavior of a bead-spring chain in a solvent.

### 1.2.3 Brownian Dynamics

The erratic motion of a large particle in a fluid composed of much smaller molecules was first observed by Robert Brown in 1828, and is termed Brownian motion. Brownian motion originates from the frequent collisions of the solvent molecules with the particle induced by thermal noise. Such motion is described by a stochastic differential equation known as the Langevin equation [56]. The Langevin equation is a statement of force balance, and takes the form

$$m \frac{dv}{dt} = -\zeta v + F_B(t) \quad (1.12)$$

for a particle of mass  $m$ , velocity  $v$  and drag coefficient  $\zeta$  constrained to one dimension in an otherwise quiescent solvent, where  $F_B(t)$  denotes the Brownian force resulting from the random impacts of the solvent molecules with the particle. This random, thermal force has the following properties [57]:

$$\begin{aligned} \langle F_B(t) \rangle &= 0 \\ \langle F_B(t) F_B(t') \rangle &= \alpha_B \delta(t - t') \end{aligned} \quad (1.13)$$

with the angular brackets representing an average with respect to the distribution of the random force at the given time  $t$ , and where  $\alpha_B$  is a constant.

The solution of Equation 1.12 yields the results  $\langle v \rangle = 0$  and

$$\frac{1}{2} m \langle v^2 \rangle = \frac{\alpha_B}{4\zeta} \left( 1 - e^{-2\zeta t/m} \right) \quad (1.14)$$

from which it follows that the equilibrium kinetic energy of the particle (in the limit  $t \rightarrow \infty$ ) is  $m \langle v^2 \rangle / 2 = \alpha_B / (4\zeta)$ . We may now take recourse to the theorem of equipartition of energy, whereby  $m \langle v^2 \rangle / 2 = k_B T / 2$  at equilibrium and consequently,  $\alpha_B = 2k_B T \zeta$ . This relationship between the Brownian force and the drag on the bead is a special case of the fluctuation–dissipation theorem [57].

The Brownian force  $F_B$  has the formal representation

$$F_B(t) dt = \sqrt{2k_B T \zeta} dW(t) \quad (1.15)$$

where  $W(t)$  is a Gaussian Wiener process whose increments  $dW$  have the properties  $\langle dW(t) \rangle = 0$  and  $\langle dW(t) dW(t') \rangle = dt \delta(t - t')$  [57].

The time scale  $m/(2\zeta)$  for typical sizes of the Brownian particle is of order  $10^{-3}$ – $10^{-7}$  s, whereby the neglect of inertia in Equation 1.12 is justified [57]. In the absence of external forces, the inertia-less Langevin equation represents the balance between the drag exerted by the solvent and the random, thermal force arising from the collisions of the solvent molecules with the particle, and yields the following stochastic differential equation for the position  $r(t)$  of the particle [with  $\dot{r}(t) = v(t)$ ] in one dimension:

$$dr(t) = \sqrt{\frac{2k_B T}{\zeta}} dW(t) \quad (1.16)$$

The technique of Brownian dynamics may be adopted to derive the time-varying position of each bead in a coarse-grained bead–spring representation of the polymer chain. The coarse-graining of several monomeric units into a single bead whose size is large in comparison with the size of the

solvent molecules underlies the continuum description of the solvent, and enables the application of the Langevin equation to each bead of the chain [57]. However, for a system of  $N$  beads, the solvent velocity field is influenced by the presence of each bead, resulting in a perturbation of the velocity field around the remaining beads. Therefore, in its most general form, the set of Langevin equations governing the positions of each bead must account for hydrodynamic interactions among the beads. The general form of the coupled Langevin equations for the position vector  $\mathbf{r}_i$  of each bead  $i = 1, \dots, N$  of the chain was first derived by Ermak and McCammon [58], and is given by the expression [57, 58]

$$d\mathbf{r}_i = \left[ \mathbf{v} + \frac{1}{k_B T} \sum_{j=1}^N \mathbf{D}_{ij} \cdot \mathbf{F}_j^{\text{det}} + \sum_{j=1}^N \frac{\partial}{\partial \mathbf{r}_j} \cdot \mathbf{D}_{ij} \right] dt + \sum_{j=1}^N \sqrt{2} \mathbf{B}_{ij} \cdot d\mathbf{W}_j \quad (1.17)$$

where  $\mathbf{v}$  denotes the solvent velocity field. Equation 1.17 is a generalization of Equation 1.16 for a three-dimensional multi-particle system in the presence of hydrodynamic interactions, interaction forces and external forces. The term  $\mathbf{D}_{ij}/(k_B T)$  represents the mobility tensor relating the solvent velocity vector induced at the position of bead  $i$  to the force vector acting at the location of bead  $j$ , with  $\mathbf{D}_{ij}$  a  $3 \times 3$  submatrix of the  $3N \times 3N$  symmetric, positive-definite diffusion tensor  $\mathbf{D}$  for the  $N$ -bead system. The properties of symmetry and positive-definiteness of the mobility tensor and, hence, of  $\mathbf{D}$  arise from the properties of incompressible Stokes flows satisfying any set of prescribed boundary conditions [59]. The net deterministic force acting on bead  $j$  is denoted by  $\mathbf{F}_j^{\text{det}}$ . The terms  $\mathbf{W}_j$ ,  $j = 1, \dots, N$ , represent  $N$  independent vector Wiener processes. Their properties  $\langle d\mathbf{W}_j(t) \rangle = \mathbf{0}$  and  $\langle d\mathbf{W}_i(t) d\mathbf{W}_j(t') \rangle = dt \delta_{ij} \delta(t - t') \boldsymbol{\delta}$ , where  $i, j = 1, \dots, N$  and  $\boldsymbol{\delta}$  is the identity tensor, reflect the properties of vanishing mean and  $\delta$ -correlation, respectively, of the random thermal force acting on the beads. The  $3 \times 3$  matrix  $\mathbf{B}_{ij}$  is a square submatrix of the  $3N \times 3N$  tensor  $\mathbf{B}$  obtained from the Cholesky decomposition of  $\mathbf{D}$  [58], whereby  $\mathbf{D} = \mathbf{B} \cdot \mathbf{B}^\dagger$ , with the superscript  $\dagger$  representing the transposition operator. This relation between the random thermal force term and the diffusion tensor derives from the fluctuation–dissipation theorem [57]. A simplification that arises when the solvent possesses an incompressible Stokes flow field is that the term  $\sum_{j=1}^N \partial/\partial \mathbf{r}_j \cdot \mathbf{D}_{ij}$  vanishes [59].

Intrachain exclusion among the beads of a bead–spring chain in a good solvent may be modeled via the inclusion of an excluded volume force in Equation 1.17, whereby  $\mathbf{F}_j^{\text{det}} = \mathbf{F}_j^{\text{ev}} + \mathbf{F}_j^{\text{s}}$  in the absence of external forces, with  $\mathbf{F}_j^{\text{ev}}$  and  $\mathbf{F}_j^{\text{s}}$  denoting, respectively, the net excluded volume force exerted on bead  $j$  by the remaining beads and the net spring force exerted on bead  $j$  by the adjoining springs. The latter is calculated from the expression

$$\mathbf{F}_j^{\text{s}} = \mathbf{F}_{\text{spr}}(\mathbf{Q}_j) - \mathbf{F}_{\text{spr}}(\mathbf{Q}_{j-1}) \quad (1.18)$$

where  $\mathbf{Q}_j = \mathbf{r}_{j+1} - \mathbf{r}_j$  is the spring vector of the spring connecting beads  $j$  and  $j + 1$ . For the special case  $j = 1$ ,

$$\mathbf{F}_1^{\text{s}} = \mathbf{F}_{\text{spr}}(\mathbf{r}_2 - \mathbf{r}_1) \quad (1.19)$$

while for  $j = N$ ,

$$\mathbf{F}_N^{\text{s}} = -\mathbf{F}_{\text{spr}}(\mathbf{r}_N - \mathbf{r}_{N-1}) \quad (1.20)$$

We make use of the modified Marko–Siggia law given by Equation 1.11 to model DNA elasticity in Chapters 4 and 5, while in near-equilibrium situations adequately represented by a quadratic

spring potential, we employ Gaussian springs exhibiting linear force–extension behavior. Intrachain exclusion is considered in Chapter 5 by means of the following expression for the soft, repulsive intrachain excluded volume force developed by Jendřejack et al. [60]:

$$\mathbf{F}_j^{\text{ev}} = v k_B T N_{k,s}^2 \pi \left( \frac{3}{4\pi S_s^2} \right)^{5/2} \sum_{k=1, k \neq j}^N \exp \left[ -\frac{3}{4S_s^2} |\mathbf{r}_j - \mathbf{r}_k|^2 \right] (\mathbf{r}_j - \mathbf{r}_k) \quad (1.21)$$

where  $v$  is the excluded volume parameter and  $S_s^2 = N_{k,s} b_k^2/6$  the mean equilibrium size of a Gaussian spring of  $N_{k,s}$  Kuhn segments. Equation 1.21 derives from the energy penalty associated with the overlap of two Gaussian coils [50, 60]. The parameter  $v$  must be chosen a priori so as to reproduce the experimentally measured equilibrium radius of gyration of the polymer under consideration in a good solvent.

The derivation of the exact Stokes flow field in a solvent containing  $N$  beads induced by the application of a point force at the location of one of the beads entails the solution of the Stokes equations in the fluid domain subject to no-slip of the solvent velocity on the surface of each bead, and is an analytically intractable problem. The most commonly used approximation of the diffusion tensor follows from a variational bound due to Rotne and Prager [61], derived independently by Yamakawa [62], known as the Rotne–Prager–Yamakawa (abbreviated RPY) tensor:

$$\begin{aligned} \frac{D_{ij}^{mn}}{k_B T} &= \frac{1}{8\pi\mu} \left[ \left( 1 + \frac{2a^2}{3r^2} \right) \frac{\delta_{mn}}{r} + \left( 1 - \frac{2a^2}{r^2} \right) \frac{r_m r_n}{r^3} \right] \text{ if } r \geq 2a \text{ and } i \neq j \\ &= \frac{1}{6\pi\mu a} \left[ \left( 1 - \frac{9r}{32a} \right) \delta_{mn} + \frac{3}{32a} \frac{r_m r_n}{r} \right] \text{ if } r < 2a \text{ and } i \neq j \\ &= \frac{\delta_{mn}}{6\pi\mu a} \text{ if } i = j \end{aligned} \quad (1.22)$$

where  $D_{ij}^{mn}$  represents the matrix element of  $\mathbf{D}_{ij}$  associated with the induction of a velocity in the  $m$ -direction at  $\mathbf{r}_i$  by the application of a force in the  $n$ -direction at  $\mathbf{r}_j$ ,  $a$  denotes the bead radius,  $\mu$ , the solvent viscosity and  $\mathbf{r} = \mathbf{r}_i - \mathbf{r}_j$ , the vector pointing from bead  $j$  to bead  $i$ . Note the appearance of the parameter  $a$ , an a priori knowledge of which must precede the application of Equation 1.17 using Equation 1.22.

A simplified form of Equation 1.17 follows under the “free draining” assumption with the neglect of hydrodynamic interactions among the beads, resulting in the equation

$$d\mathbf{r}_i = \left( \mathbf{v} + \frac{1}{\zeta} \mathbf{F}_i^{\text{det}} \right) dt + \sqrt{\frac{2k_B T}{\zeta}} d\mathbf{W}_i, \quad i = 1, \dots, N \quad (1.23)$$

with  $\zeta = 6\pi\mu a$  representing the Stokes drag coefficient for each bead, and  $\mathbf{D} = (k_B T/\zeta)\boldsymbol{\delta}$ . The neglect of hydrodynamic interactions is partially justified by the screening effect of the channel walls in complicated microchannel geometries. The free draining assumption has the additional advantage that Equation 1.23 may be applied in nondimensional form without prior knowledge of the bead radius  $a$ . This is so because the dependence on  $a$  appears only implicitly through  $\zeta$  in Equation 1.23, and  $k_B T/\zeta$  may be chosen as the unit of diffusivity. In contrast, Equations 1.17 and 1.22 necessitate the explicit specification of  $a$ . Typically,  $a$  may be selected to reproduce the experimentally observed diffusion coefficient or relaxation time of the polymer.

In general, Equations 1.17 and 1.23 are nonlinear and must be integrated numerically to determine the bead positions as a function of time. However, in the absence of hydrodynamic interactions, excluded volume interactions and all other nonlinear forces, and with the spring force–extension behavior described by Hooke’s law, Equation 1.23 yields a set of decoupled, linear stochastic differential equations, and consequently, an analysis into normal modes is made possible. We exploit this analytical solution technique in Chapter 4 and Appendix C. Such a linear, free draining bead–spring model of a polymer chain is also known as the Rouse model [50, 57]. Account for excluded volume interactions and nonlinear force–extension behavior necessitates use of a numerical integration technique, for which we adopt the semi-implicit predictor–corrector scheme described in Refs. [63] and [64]. The availability of the bead positions as functions of time enables the computation of several other transient and steady configurational properties of the chain, such as its extension and radius of gyration.

The free draining assumption is employed in Chapters 4 and 5, justified in part by the screening of hydrodynamic interactions in microchannel geometries and by the counterion cloud surrounding DNA. Additionally, we provide a parametric study of a bead–spring chain representing a DNA molecule in a good solvent at a preselected discretization of  $N_{k,s} = 19.8$  in Appendix A for the determination of  $v$  and  $a$  so as to reproduce the experimentally measured radius of gyration [47], diffusion coefficient [47, 65] and relaxation time of DNA [66–69]. Simultaneously, Appendix A also explains in greater detail the simulation procedure adopted by us.

#### 1.2.4 Overview of Results

In Chapter 4, we investigate the mechanism of tension propagation in a polymer chain held tethered at one end following the imposition of uniform solvent flow, and demonstrate that tension propagates diffusively in a Rouse chain, but convectively in a finitely-extensible wormlike chain at high flow strengths. This study has relevance not only to chain unraveling subsequent to a polymer–obstacle collision in an array of obstacles, but also in other situations involving transient chain stretching, such as dilute solution capillary electrophoresis [25, 26] and chain entanglements occurring in flows of polymer solutions [70]. Our findings enable a critical examination of the assumptions made by Minc et al. [34] and Dorfman [35] in modeling chain dynamics in an array of obstacles.

In Chapter 5, we employ the nonseparable continuous-time random walk model [71] of chain dynamics with account for the electric-field dependence of chain extension in the array (neglected in the prior studies of Refs. [34] and [35]) to make analytical predictions of the mobility, dispersivity and collision probability of a single chain and the separation resolution effected between different chain sizes. We concomitantly perform Brownian dynamics simulations of DNA chains in a self-assembled array of magnetic beads [72, 73], and demonstrate that our stochastic model correctly predicts the nonmonotonicity of the separation resolution with respect to the electric field strength. These studies have applications in the design of DNA separation devices and the a priori prediction of their efficacy.



# *An Extension of Faxen's Laws for Nonisothermal Flow Around a Sphere*

---

This Chapter is reprinted in part with permission from A. Mohan and H. Brenner, "An extension of Faxen's laws for nonisothermal flow around a sphere," *Physics of Fluids* **17**, 038107 (2005). Copyright © 2005 by the American Institute of Physics.

## 2.1 Derivation of Faxen's Laws with Account for Thermal Slip

In the present Chapter, we extend Faxen's creeping-flow laws [74] so as to include the effect of thermal slip on the flow around a heat-conducting sphere present in an arbitrary, undisturbed Stokes flow velocity field within which temperature gradients exist.

Consider the Stokes flow of a nonisothermal fluid (of temperature-independent viscosity  $\mu$ , thermal conductivity  $k$ , and heat capacity  $c_p$ ) around a solid sphere of radius  $a$  whose thermal conductivity is  $k_s$ . Under such conditions, the fluid's velocity and pressure fields  $(\mathbf{v}, p)$  satisfy the incompressible creeping flow equations:

$$\begin{aligned}\nabla \cdot \mathbf{v} &= 0 \\ \mu \nabla^2 \mathbf{v} &= \nabla p\end{aligned}\tag{2.1}$$

The velocity field  $\mathbf{v}$  satisfies the no-penetration condition on the sphere surface,  $S_p$ :

$$\hat{\mathbf{r}} \cdot [\mathbf{v} - (\mathbf{U} + \boldsymbol{\Omega} \times \mathbf{r})] = 0 \quad \text{at } r = a \quad (2.2)$$

with  $\mathbf{r}$  the position vector drawn from the sphere center  $r = 0$ , wherein the quantity  $\hat{\mathbf{r}} = \mathbf{r}/r$  denotes a unit radial vector;  $\mathbf{U}$  is the velocity with which the center of the sphere translates, and  $\boldsymbol{\Omega}$  is the angular velocity of the sphere. In the presence of temperature gradients, a thermal slip condition [cf. Equation 1.3], here quantified generically by the thermal slip coefficient  $C_s$ , is imposed upon the relative tangential component of the fluid velocity at a point on  $S_p$ , namely

$$\mathbf{I}_s \cdot [\mathbf{v} - (\mathbf{U} + \boldsymbol{\Omega} \times \mathbf{r})] = C_s \nabla_s T \quad \text{at } r = a \quad (2.3)$$

with  $\nabla_s = \mathbf{I}_s \cdot \nabla$  the surface gradient operator, and  $\mathbf{I}_s = \mathbf{I} - \hat{\mathbf{r}}\hat{\mathbf{r}}$  the surface projection dyadic, in which  $\mathbf{I}$  is the idemfactor.

For gases,  $C_s$  is determined by the interactions among the molecules of the gas and the solid sphere, which govern the law of molecular reflection at the surface. In the case of liquids, Semenov [17] has provided a formula whereby  $C_s$  can be calculated from the properties of the liquid and those of the solid particle. Values of his slip coefficient for the thermophoretic motion of silica particles of radii  $a \approx 0.1 \mu\text{m}$  in water, cyclohexane, and several other solvents are of the order of  $10^{-7} \text{ cm}^2 \text{ s}^{-1} \text{ K}^{-1}$  [17].

The steady temperature fields  $T$  and  $T_s$  in the fluid and sphere are governed by the respective convection-free energy equations

$$\begin{aligned} \nabla^2 T &= 0 \\ \nabla^2 T_s &= 0 \end{aligned} \quad (2.4)$$

subject to the boundary conditions

$$\begin{aligned} T &= T_s \quad \text{at } r = a \\ \hat{\mathbf{r}} \cdot \nabla T &= \gamma \hat{\mathbf{r}} \cdot \nabla T_s \quad \text{at } r = a \quad \text{where } \gamma = k_s/k \\ \nabla T &\longrightarrow \nabla T_\infty = \text{const} \quad \text{as } r \longrightarrow \infty \end{aligned} \quad (2.5)$$

where  $T_\infty$  denotes the undisturbed temperature field and  $\nabla T_\infty$  is a prescribed constant. The respective temperature fields satisfying Equations 2.4–2.5 are readily found to be

$$\begin{aligned} T &= \left[ 1 + \left( \frac{1-\gamma}{2+\gamma} \right) \left( \frac{a}{r} \right)^3 \right] \mathbf{r} \cdot \nabla T_\infty \\ T_s &= \frac{3}{2+\gamma} \mathbf{r} \cdot \nabla T_\infty \end{aligned} \quad (2.6)$$

The radial gas and solid temperature gradients at the sphere surface are thus given by

$$\hat{\mathbf{r}} \cdot \nabla T |_{r=a} = \gamma \hat{\mathbf{r}} \cdot \nabla T_s |_{r=a} = \frac{3\gamma}{2+\gamma} \hat{\mathbf{r}} \cdot \nabla T_\infty \quad (2.7)$$

For convenience, we restore the appearance of a no-slip condition on the sphere by introducing

the new “velocity” field

$$\mathbf{u} = \mathbf{v} - C_s \nabla T \quad (2.8)$$

such that  $\mathbf{u}$  satisfies the no-slip condition  $\mathbf{I}_s \cdot [\mathbf{u} - (\mathbf{U} + \boldsymbol{\Omega} \times \mathbf{r})] = \mathbf{0}$  on  $S_p$ . However,  $\mathbf{u}$ , in contrast with  $\mathbf{v}$ , does not satisfy a no-penetration condition like Equation 2.2, since  $\hat{\mathbf{r}} \cdot [\mathbf{u} - (\mathbf{U} + \boldsymbol{\Omega} \times \mathbf{r})] = -C_s \hat{\mathbf{r}} \cdot \nabla T \neq 0$  in general at  $r = a$  (unless  $k_s = 0$ ). The field  $\mathbf{u}$  satisfies the equations

$$\begin{aligned} \nabla \cdot \mathbf{u} &= 0 \\ \mu \nabla^2 \mathbf{u} &= \nabla p \end{aligned} \quad (2.9)$$

which follow from Equations 2.1 and 2.4<sub>1</sub>. The far-field and surface boundary conditions to be imposed on  $\mathbf{u}$  adopt the respective forms

$$\mathbf{u} \rightarrow \mathbf{u}_\infty \equiv \mathbf{v}_\infty - C_s \nabla T_\infty \quad \text{as } r \rightarrow \infty \quad (2.10)$$

and

$$\mathbf{u} = \mathbf{U} + \boldsymbol{\Omega} \times \mathbf{r} - C_s \hat{\mathbf{r}} \cdot \nabla T \quad \text{at } r = a \quad (2.11)$$

with  $\mathbf{v}_\infty$  the undisturbed Stokes velocity field satisfying Equations 2.1 in the absence of the sphere.

Since  $\mathbf{u}$  satisfies the incompressible creeping motion Equations 2.9, we may use the precursor of Faxen's first law for the force  $\mathbf{F}$  exerted by the fluid on the sphere, derived from the Lorentz reciprocal theorem, in the form [75]

$$\mathbf{F} = -\frac{3\mu}{2a} \int_{S_p} (\mathbf{u} - \mathbf{u}_\infty) dS \quad (2.12)$$

where  $dS$  denotes an areal surface element on  $S_p$ . Substitution of Equation 2.11 into Equation 2.12 yields

$$\mathbf{F} = \mathbf{F}_\Omega + \mathbf{F}_T + \mathbf{F}_\infty - 6\pi\mu a \mathbf{U} \quad (2.13)$$

where

$$\mathbf{F}_\Omega = -\frac{3\mu}{2} \boldsymbol{\Omega} \times \int_{S_p} \hat{\mathbf{r}} dS \quad (2.14)$$

$$\mathbf{F}_T = \frac{3\mu}{2a} C_s \int_{S_p} dS \hat{\mathbf{r}} \cdot \nabla T \quad (2.15)$$

and

$$\mathbf{F}_\infty = \frac{3\mu}{2a} \int_{S_p} \mathbf{u}_\infty dS \quad (2.16)$$

Inasmuch as  $\mathbf{u}_\infty$  is necessarily free of singularities in the fluid domain ( $0 \leq r \leq a$ ) presently occupied by the sphere, a Taylor series expansion of  $\mathbf{u}_\infty$  about the sphere center in Equation 2.16, with the terms involving derivatives of order higher than the second being identically zero in

creeping flow, yields the usual form of Faxen's first law, namely [74]

$$\mathbf{F}_\infty = 6\pi\mu a \left( [\mathbf{u}_\infty]_0 + \frac{a^2}{6} [\nabla^2 \mathbf{u}_\infty]_0 \right) \quad (2.17)$$

where the subscript "0" denotes evaluation of the function to which it is affixed at  $r = 0$ . Furthermore, since  $\int_{S_p} \hat{\mathbf{r}} dS = \mathbf{0}$ , it follows that  $\mathbf{F}_\Omega = \mathbf{0}$ .

To evaluate  $\mathbf{F}_T$ , we substitute Equation 2.7 into Equation 2.15 to obtain

$$\mathbf{F}_T = \frac{9\mu C_s \gamma}{2(2 + \gamma)a} \nabla T_\infty \cdot \int_{S_p} dS \hat{\mathbf{r}} = \frac{6\pi a \mu C_s \gamma}{2 + \gamma} \nabla T_\infty \quad (2.18)$$

since  $\int_{S_p} dS \hat{\mathbf{r}} = (4/3) \pi a^2 \mathbf{I}$ .

Upon summing the various contributions to the force in Equation 2.13 and expressing the result in terms of  $\mathbf{v}$  via use of Equation 2.8, we obtain the following generalization of Faxen's first law:

$$\mathbf{F} = 6\pi\mu a \left( [\mathbf{v}_\infty]_0 + \frac{a^2}{6} [\nabla^2 \mathbf{v}_\infty]_0 - \mathbf{U} - C_s \frac{2}{2 + \gamma} \nabla T_\infty \right) \quad (2.19)$$

The precursor of Faxen's second law for the torque  $\mathbf{L}_0$  acting on the sphere about its center is given by the expression [75]

$$\mathbf{L}_0 = -\frac{3\mu}{a} \int_{S_p} \mathbf{r} \times (\mathbf{u} - \mathbf{u}_\infty) dS \quad (2.20)$$

Substitution of Equation 2.11 into Equation 2.20 reveals that Faxen's second law is not modified by the presence of the uniform temperature gradient,  $\nabla T_\infty$ . Explicitly, making use of the fact that  $\nabla \times \nabla T = \mathbf{0}$ , and hence  $\nabla \times \mathbf{u} = \nabla \times \mathbf{v}$ , we recover the usual form of Faxen's second law [74]:

$$\mathbf{L}_0 = 8\pi\mu a^3 \left( \frac{1}{2} [\nabla \times \mathbf{v}_\infty]_0 - \mathbf{\Omega} \right) \quad (2.21)$$

## 2.2 Applications

Consider the application of Equations 2.19 and 2.21 to the situation wherein the spherical particle is contained between two mass-impermeable hot and cold walls separated by a distance  $L$ . The particle is assumed to be located at a large distance from both walls. Thus, to dominant order in  $a/L \ll 1$ , the fluid far from the particle may effectively be regarded as being at rest, i.e.,  $\mathbf{v}_\infty \rightarrow \mathbf{0}$  as  $r \rightarrow \infty$ . We find that since  $\nabla \times \mathbf{v}_\infty = \mathbf{0}$ , a torque-free sphere will not rotate:  $\mathbf{\Omega} = \mathbf{0}$ . As a result, the velocity of a force- and torque-free spherical particle is given by the expression

$$\mathbf{U} = -C_s \frac{1}{1 + \gamma/2} \nabla T_\infty \quad (2.22)$$

and is identical in form to that obtained from Epstein's theory [6], derived by formally solving the detailed creeping-flow boundary-value problem with Maxwell's thermal slip condition.

Next, consider the case of a small, mobile spherical particle of radius  $a$  in a closed-ended, laterally-insulated circular capillary tube of radius  $R_0$  and length  $2L$ , of large aspect ratio  $L/R_0 \gg 1$ , such that  $a/L \ll 1$ . As in the Reynolds [5] particle-free thermal transpiration problem, the hot and cold ends, respectively situated at  $z = L$  and  $z = -L$ , are maintained at temperatures  $T_h$  and  $T_c$ . The corresponding pressures at the two ends are, respectively, denoted by  $p_h$  and  $p_c$ . The sphere center moves axially with velocity  $\mathbf{U}$  at a distance  $R = b$  from the axis  $R = 0$  of the cylinder, where  $(R, \phi, z)$  denote a system of circular cylindrical coordinates. The sphere is assumed to be instantaneously situated far from either end of the capillary, and to also satisfy the inequality  $a/(R_0 - b) \ll 1$ . The undisturbed velocity field in the absence of the sphere (involving thermal slip along the insulated capillary walls in accord with the relation  $\mathbf{v} = C_s \nabla_s T$  at  $R = R_0$ , where  $\nabla_s = \hat{\mathbf{z}} \partial / \partial z |_{R=R_0}$ , in which  $\hat{\mathbf{z}}$  is a unit vector in the  $z$ -direction), is [3]

$$\mathbf{v}_\infty = - \left[ 1 - 2 \left( \frac{R}{R_0} \right)^2 \right] C_s \nabla T_\infty \quad (2.23)$$

in which  $\nabla T_\infty = \hat{\mathbf{z}} (T_h - T_c) / 2L = \text{constant}$ . In the above, the fluid velocity  $\mathbf{v}$  and sphere velocity  $\mathbf{U}$  are both measured relative to the fixed cylinder walls. Upon introducing Equation 2.23 into Equation 2.19, bearing in mind that the subscript “0” refers to evaluation at  $R = b$ , we obtain

$$\mathbf{F} = 6\pi\mu a \left[ \left\{ 2 \left( \frac{b}{R_0} \right)^2 - \left( \frac{4 + \gamma}{2 + \gamma} \right) \right\} C_s \nabla T_\infty - \mathbf{U} \right] + O \left( \frac{a}{R_0} \right) \quad (2.24)$$

As before,  $\gamma$  refers to the ratio of the sphere’s thermal conductivity to that of the fluid. A small, neutrally buoyant sphere will thus move with the size-independent velocity

$$\mathbf{U} = \left[ 2 \left( \frac{b}{R_0} \right)^2 - \left( \frac{4 + \gamma}{2 + \gamma} \right) \right] C_s \nabla T_\infty + O \left( \frac{a}{R_0} \right) \quad (2.25)$$

and rotate with the angular velocity

$$\boldsymbol{\Omega} = 2C_s \frac{b}{R_0^2} \hat{\mathbf{R}} \times \nabla T_\infty \quad (2.26)$$

where  $\hat{\mathbf{R}}$  is the unit cylindrical radial vector pointing outward from the capillary axis.

### 2.3 Extension to Electrophoresis

While the present work focuses on the specific case of temperature gradient-induced slip, our results are applicable to other sources of slip occurring at solid surfaces. For instance, our scheme may be applied to study the electrokinetic flow around a spherical particle in a capillary tube, wherein the electric potential is governed by equations mathematically identical in form to those governing the temperature field in the present nonisothermal situation, with the electrokinetic slip velocity at the particle surface proportional to the gradient of the electric potential, analogous to the corresponding thermal slip condition. A detailed solution of the problem of electrokinetic flow around a sphere in a capillary is provided in Ref. [76].



# *Thermophoretic Motion of a Slightly Deformed Sphere Through a Viscous Fluid*

---

This Chapter is reproduced in part with permission from A. Mohan and H. Brenner, "Thermophoretic motion of a slightly deformed sphere through a viscous fluid," *SIAM Journal on Applied Mathematics* **66**, 787–801 (2006). Copyright © 2006 by the Society for Industrial and Applied Mathematics.

## **3.1 Introduction**

The thermophoretic motion of a sphere in a gas, which occurs in the direction opposite to that of the imposed temperature gradient, was first calculated by Epstein [6] based upon Maxwell's thermal creep condition. Subsequent analyses of the problem are summarized by Zheng [8]. Most previous studies, however, deal only with the motion of spherical particles, whereas many particles encountered in practical applications are irregularly shaped. Existing theoretical studies of the thermophoresis of nonspherical particles are currently available only for axisymmetric flows, wherein the imposed temperature gradient lies parallel to the particle's axis of symmetry [77, 78]. Reference [79] provides a numerical solution for asymmetric thermophoretic flow around a two-sphere

aggregate. Given this dearth of information on nonsymmetric thermophoretic particle motions, we were motivated to study a ‘simple’ example of such motion.

The present investigation develops an asymptotic expansion of the equations of Stokes flow satisfying the thermal slip condition at the surface of a heat-conducting, arbitrarily deformed sphere, wherein the deviation from the spherical shape is small, while the imposed temperature gradient is arbitrarily oriented with respect to the particle’s geometry. In principle, the asymptotic solution may be obtained correct to any order in the perturbation parameter, which measures the deviation from the spherical shape, for arbitrarily deformed particles. We here provide the explicit solution, correct to the first order, for the specific case of an ellipsoidal particle. For the special case of a force- and torque-free, thermally insulated (i.e., nonconducting) particle, it is found that the thermophoretic velocity of the particle reduces to that of a sphere moving under the same temperature gradient in a gas otherwise at rest. This result accords with the related findings of Morrison [14], namely that the phoretic velocity of an insulated particle is independent of its shape and orientation, as well as of its size. (Morrison’s proof, though offered in the context of electrophoresis, is equally applicable to the thermophoretic case, provided that the particle is nonconducting, i.e., thermally insulated in the latter case.)

The detailed solution for the case of isothermal Stokes flow around a slightly deformed sphere (subject to no slip at its surface) was presented by Brenner and his collaborators [74, 75, 80, 81]. That solution is here extended to allow for slip at the surface of the deformed sphere arising from temperature inhomogeneities in the fluid.

### 3.2 Problem Formulation

Consider the incompressible Stokes flow around a slightly deformed sphere moving without rotation at a velocity of  $\mathbf{U}$  through a fluid across which an otherwise uniform temperature gradient, here denoted by the space-fixed constant vector  $\mathbf{G}$ , has been imposed under undisturbed flow conditions, i.e., in the absence of the particle. It is assumed that the surface of the particle,  $S_p$ , is described geometrically in invariant form by the equation

$$r = a \left[ 1 + \epsilon \sum_n \mathbf{A}_n \boxed{n} \mathbf{P}_n(\hat{\mathbf{r}}) + O(\epsilon^2) \right] \quad (3.1)$$

where  $\mathbf{A}_n$  is an  $O(1)$  body-fixed polyadic of rank  $n$  describing the shape of the deformed body. The  $n$ th-rank polyadics  $\mathbf{P}_n(\hat{\mathbf{r}}) = (-1)^n (n!)^{-1} r^{n+1} \overbrace{\nabla \nabla \dots \nabla}^{n \text{ times}} (1/r)$  are the polyadic surface harmonics of order  $n$  [75, 81], whose argument  $\hat{\mathbf{r}}$  is the space-fixed unit position vector,  $\hat{\mathbf{r}} = \mathbf{r}/r$ , while  $\epsilon \ll 1$  is a small, dimensionless quantity, inseparable from the term  $\sum_n \mathbf{A}_n \boxed{n} \mathbf{P}_n(\hat{\mathbf{r}})$  describing the deformation of the surface. The  $r = |\mathbf{r}|$  radial coordinate is measured from an origin situated at the center of the undeformed sphere of radius  $a$ . Since the surface spherical harmonics constitute a complete set of orthonormal polynomials in the surface coordinates  $(\theta, \phi)$ , any function thereof, say  $f(\hat{\mathbf{r}})$ , may be expanded in invariant form in terms of the polyadics  $\mathbf{P}_n(\hat{\mathbf{r}})$ , analogous to the well-known scalar spherical harmonic expansion of an arbitrary function  $f(\theta, \phi)$  [82]; hence, Equation 3.1 is the general equation characterizing the surface of any arbitrarily shaped body whose deviation from a spherical shape is small. The symbol  $\boxed{n}$  refers to  $n$  successive dot-product contraction operations

performed in the order prescribed by the nesting convention of [75], wherein the  $n$  indices of the corresponding polyadics are contracted sequentially, beginning with the innermost indices. It follows that  $\mathbf{A}_n \overline{[n]} \mathbf{P}_n(\hat{\mathbf{r}}) = \mathbf{P}_n(\hat{\mathbf{r}}) \overline{[n]} \mathbf{A}_n$ , whence the surface  $S_p$  may also be equivalently described by the alternate expression

$$r = a [1 + \epsilon \mathbf{P}_n(\hat{\mathbf{r}}) \overline{[n]} \mathbf{A}_n + O(\epsilon^2)] \quad (3.2)$$

wherein we have here invoked the summation convention, which will be used throughout, with the repeated index  $n$  implying a sum over that index.

The unit normal to  $S_p$  is given by the expression  $\hat{\mathbf{n}} = \nabla f / |\nabla f|$ , with  $f$  defined by the relation  $f(\mathbf{r}) = r - a [1 + \epsilon \mathbf{P}_n \overline{[n]} \mathbf{A}_n + O(\epsilon^2)] = 0$ . Together with the use of the gradient operator in invariant spherical coordinates,

$$\nabla = \hat{\mathbf{r}} \left( \frac{\partial}{\partial r} \right)_{\hat{\mathbf{r}}} + \frac{1}{r} \left( \frac{\partial}{\partial \hat{\mathbf{r}}} \right)_r \quad (3.3)$$

one thus obtains

$$\hat{\mathbf{n}} = \hat{\mathbf{r}} - \epsilon \hat{\nabla} \mathbf{P}_n \overline{[n]} \mathbf{A}_n + O(\epsilon^2) \quad (3.4)$$

wherein  $\hat{\nabla} = (\partial/\partial \hat{\mathbf{r}})_r$  is the surface gradient operator. In deriving the latter, we have used the identities  $\hat{\mathbf{r}} \cdot \hat{\nabla} = 0$  and  $(\mathbf{I} - \hat{\mathbf{r}}\hat{\mathbf{r}}) \cdot \hat{\nabla} = \hat{\nabla}$ , arising from the orthonormality of the coordinate axes.

The equations of Stokes flow, describing the flow around the deformed sphere, are

$$\nabla \cdot \mathbf{v} = 0 \quad (3.5)$$

$$\mu \nabla^2 \mathbf{v} = \nabla p \quad (3.6)$$

where  $p$  denotes the pressure. The boundary conditions imposed upon the fluid's velocity require that the latter approach the particle-free, undisturbed fluid motion at infinity,

$$\mathbf{v} \rightarrow \mathbf{0} \text{ as } r \rightarrow \infty \quad (3.7)$$

and that the thermal slip condition on  $S_p$  satisfy

$$\mathbf{v} = \mathbf{U} + C_s (\mathbf{I} - \hat{\mathbf{n}}\hat{\mathbf{n}}) \cdot \nabla T_s \quad (3.8)$$

where  $T_s$  denotes the temperature within the solid (with  $T_s = T$  on  $S_p$ ), and  $C_s$  is the thermal slip coefficient, which in the case of gases takes the value  $3/4 (\mu/\rho T)$ , according to Maxwell. In that case,  $C_s$  is a constant, owing to the inverse relationship existing between  $\rho$  and  $T$  from the ideal gas law, with the transport coefficient  $\mu$  assumed constant, at least for small temperature gradients. For liquids, Semenov [17] has provided a formula whereby  $C_s$  can be calculated from the properties of the liquid and the solid particle [cf. Chapter 2]. Values of  $C_s$  for the thermophoretic motion of silica particles in several solvents are found to be of the order of  $10^{-8}$ – $10^{-7}$   $\text{cm}^2 \text{ s}^{-1} \text{ K}^{-1}$  [17]. Values of similar order of magnitude for various particle-liquid systems have been found in the experimental study of Ref. [21].

Since the boundary condition on velocity, namely Equation 3.8, may be expressed as the sum of the particle velocity  $\mathbf{U}$  and the thermal slip velocity  $C_s (\mathbf{I} - \hat{\mathbf{n}}\hat{\mathbf{n}}) \cdot \nabla T_s$ , we will restrict ourselves, initially, to solving for the flow caused by thermal slip alone. Later, the flow arising from the motion  $\mathbf{U}$  of the particle will be linearly superposed.

The temperature fields within the fluid and the solid are governed by the respective equations

$$\begin{aligned}\nabla^2 T &= 0 \\ \nabla^2 T_s &= 0\end{aligned}\tag{3.9}$$

subject to the joint boundary conditions

$$T = T_s\tag{3.10}$$

$$\hat{\mathbf{n}} \cdot \nabla T = \gamma \hat{\mathbf{n}} \cdot \nabla T_s\tag{3.11}$$

on  $S_p$ , where  $\gamma$  denotes the ratio  $k_s/k$  of the thermal conductivity of the solid,  $k_s$ , to that of the fluid,  $k$ . In addition, we have the further conditions that the temperature within the particle remains finite at  $r = 0$ , while that within the fluid at infinity is given by the expression

$$T(r \rightarrow \infty) = \text{const} + \mathbf{G} \cdot \mathbf{r}\tag{3.12}$$

The constant appearing in Equation 3.12 is physically irrelevant, whence we may set it to zero. Perturbation solutions will now be developed for the flow and temperature fields in terms of the perturbation parameter,  $\epsilon$ .

### 3.3 Temperature Fields

Define *vector* temperature fields in the fluid and the solid,  $\mathbf{T}$  and  $\mathbf{T}_s$ , respectively, through the relations

$$\begin{aligned}T &= \mathbf{T} \cdot \mathbf{G} \\ T_s &= \mathbf{T}_s \cdot \mathbf{G}\end{aligned}\tag{3.13}$$

Since the scalar temperature fields satisfy Laplace's equation, and whereas the gradient at infinity,  $\mathbf{G}$ , is an arbitrary constant, it follows from Equations 3.9–3.11 that the vector temperature fields satisfy the respective equations

$$\begin{aligned}\nabla^2 \mathbf{T} &= \mathbf{0} \\ \nabla^2 \mathbf{T}_s &= \mathbf{0}\end{aligned}\tag{3.14}$$

subject to the boundary conditions

$$\mathbf{T} = \mathbf{T}_s\tag{3.15}$$

and

$$\hat{\mathbf{n}} \cdot \nabla \mathbf{T} = \gamma \hat{\mathbf{n}} \cdot \nabla \mathbf{T}_s\tag{3.16}$$

on the surface  $S_p$  of the deformed sphere. We expand the vector temperature fields in powers of  $\epsilon$ ,

$$\begin{aligned}\mathbf{T}(\mathbf{r}; \epsilon) &= \mathbf{T}^{(0)}(\mathbf{r}) + \epsilon \mathbf{T}^{(1)}(\mathbf{r}) + O(\epsilon^2) \\ \mathbf{T}_s(\mathbf{r}; \epsilon) &= \mathbf{T}_s^{(0)}(\mathbf{r}) + \epsilon \mathbf{T}_s^{(1)}(\mathbf{r}) + O(\epsilon^2)\end{aligned}\tag{3.17}$$

The temperature fields inside and outside of the particle at various perturbation orders, subject

to the boundary conditions on  $S_p$  given by Equations 3.15 and 3.16, may be obtained from the solution of a sequence of problems satisfying appropriate boundary conditions on the surface of the *undeformed* sphere. These latter boundary conditions, to be imposed on the sphere surface, are obtained by a Taylor series expansion of Equations 3.15 and 3.16 about  $r = a$ . Thus, expansion of Equation 3.15 while making use of Equation 3.1 furnishes the following conditions to be imposed at  $r = a$  on the  $O(1)$  and  $O(\epsilon)$  vector temperature fields:

$$\mathbf{T}^{(0)}\Big|_a = \mathbf{T}_s^{(0)}\Big|_a \quad (3.18)$$

$$\mathbf{T}^{(1)}\Big|_a + a\mathbf{A}_n \boxed{n} \mathbf{P}_n \frac{\partial \mathbf{T}^{(0)}}{\partial r}\Big|_a = \mathbf{T}_s^{(1)}\Big|_a + a\mathbf{A}_n \boxed{n} \mathbf{P}_n \frac{\partial \mathbf{T}_s^{(0)}}{\partial r}\Big|_a \quad (3.19)$$

Similarly, upon expanding  $\nabla \mathbf{T}|_{S_p}$  and  $\nabla \mathbf{T}_s|_{S_p}$  in Taylor series about  $r = a$  and making use of Equation 3.4, it follows from Equation 3.16 that

$$\hat{\mathbf{r}} \cdot \nabla \mathbf{T}^{(0)}\Big|_a = \gamma \hat{\mathbf{r}} \cdot \nabla \mathbf{T}_s^{(0)}\Big|_a \quad (3.20)$$

and

$$\begin{aligned} \hat{\mathbf{r}} \cdot \nabla \mathbf{T}^{(1)}\Big|_a + a\mathbf{A}_n \boxed{n} \mathbf{P}_n \frac{\partial}{\partial r} \hat{\mathbf{r}} \cdot \nabla \mathbf{T}^{(0)}\Big|_a - \hat{\nabla} (\mathbf{P}_n \boxed{n} \mathbf{A}_n) \cdot \nabla \mathbf{T}^{(0)}\Big|_a = \\ \gamma \hat{\mathbf{r}} \cdot \nabla \mathbf{T}_s^{(1)}\Big|_a + a\gamma \mathbf{A}_n \boxed{n} \mathbf{P}_n \frac{\partial}{\partial r} \hat{\mathbf{r}} \cdot \nabla \mathbf{T}_s^{(0)}\Big|_a - \gamma \hat{\nabla} (\mathbf{P}_n \boxed{n} \mathbf{A}_n) \cdot \nabla \mathbf{T}_s^{(0)}\Big|_a \end{aligned} \quad (3.21)$$

The leading-order, undeformed sphere problem is described by the set of equations

$$\begin{aligned} \nabla^2 \mathbf{T}^{(0)} &= \mathbf{0} \\ \nabla^2 \mathbf{T}_s^{(0)} &= \mathbf{0} \end{aligned} \quad (3.22)$$

subject to the boundary conditions given by Equations 3.18 and 3.20. Accordingly, the leading-order vector temperature fields are readily found to be

$$\begin{aligned} \mathbf{T}^{(0)} &= \left[ 1 + \left( \frac{1-\gamma}{2+\gamma} \right) \left( \frac{a}{r} \right)^3 \right] \mathbf{r} \\ \mathbf{T}_s^{(0)} &= \frac{3}{2+\gamma} \mathbf{r} \end{aligned} \quad (3.23)$$

Upon applying the gradient operator, given by Equation 3.3, to Equation 3.23, and noting that  $(\partial \hat{\mathbf{r}} / \partial \hat{\mathbf{r}})_r = \mathbf{I} - \hat{\mathbf{r}}\hat{\mathbf{r}}$ , we obtain

$$\begin{aligned} \nabla \mathbf{T}^{(0)} &= \left[ 1 - 2 \left( \frac{1-\gamma}{2+\gamma} \right) \frac{a^3}{r^3} \right] \hat{\mathbf{r}}\hat{\mathbf{r}} + \left[ 1 + \left( \frac{1-\gamma}{2+\gamma} \right) \left( \frac{a}{r} \right)^3 \right] (\mathbf{I} - \hat{\mathbf{r}}\hat{\mathbf{r}}) \\ \nabla \mathbf{T}_s^{(0)} &= \frac{3}{2+\gamma} \mathbf{I} \end{aligned} \quad (3.24)$$

Making use of Equation 3.24 furnishes the following  $O(\epsilon)$  boundary conditions from Equations

3.19 and 3.21:

$$\mathbf{T}^{(1)}\Big|_a = \mathbf{T}_s^{(1)}\Big|_a + 3 \left( \frac{1-\gamma}{2+\gamma} \right) a \mathbf{A}_n \boxed{n} \mathbf{P}_n \mathbf{P}_1 \quad (3.25)$$

[wherein we have substituted  $\mathbf{P}_1(\hat{\mathbf{r}})$  for  $\hat{\mathbf{r}}$ ], and

$$\begin{aligned} \hat{\mathbf{r}} \cdot \nabla \mathbf{T}^{(1)}\Big|_a + 6 \left( \frac{1-\gamma}{2+\gamma} \right) \mathbf{A}_n \boxed{n} \mathbf{P}_n \mathbf{P}_1 - 3 \left( \frac{1-\gamma}{2+\gamma} \right) \hat{\mathbf{v}} \mathbf{P}_n \boxed{n} \mathbf{A}_n \\ = \gamma \hat{\mathbf{r}} \cdot \nabla \mathbf{T}_s^{(1)}\Big|_a \end{aligned} \quad (3.26)$$

The  $O(\epsilon)$  vector temperature fields are governed by the equations

$$\begin{aligned} \nabla^2 \mathbf{T}^{(1)} &= \mathbf{0} \\ \nabla^2 \mathbf{T}_s^{(1)} &= \mathbf{0} \end{aligned} \quad (3.27)$$

subject to the boundary conditions given by Equations 3.25 and 3.26. Since it is convenient to expand  $\mathbf{T}^{(1)}$  and  $\mathbf{T}_s^{(1)}$  as linear combinations of solid harmonics, these boundary conditions must be expressed as linear combinations of the polyadic surface harmonics.

### 3.4 Flow Field

Next, expand the velocity and pressure fields as perturbation expansions in  $\epsilon$ :

$$\begin{aligned} \mathbf{v}(\mathbf{r}; \epsilon) &= \mathbf{v}^{(0)}(\mathbf{r}) + \epsilon \mathbf{v}^{(1)}(\mathbf{r}) + O(\epsilon^2) \\ p(\mathbf{r}; \epsilon) &= p^{(0)}(\mathbf{r}) + \epsilon p^{(1)}(\mathbf{r}) + O(\epsilon^2) \end{aligned} \quad (3.28)$$

At each order, the perturbation fields  $\mathbf{v}^{(i)}$  and  $p^{(i)}$  obey the Stokes equations,

$$\nabla \cdot \mathbf{v}^{(i)} = 0 \quad (3.29)$$

$$\mu \nabla^2 \mathbf{v}^{(i)} = \nabla p^{(i)} \quad (3.30)$$

The thermal slip boundary condition on the surface  $S_p$  of a stationary particle is, upon setting  $\mathbf{U} = \mathbf{0}$  in Equation 3.8,

$$\mathbf{v} = C_s (\mathbf{I} - \hat{\mathbf{n}}\hat{\mathbf{n}}) \cdot \nabla T_s \quad (3.31)$$

In addition, the velocity fields at all orders vanish at infinity. Expansion of the velocity at the surface  $S_p$  of the deformed sphere in a Taylor series about  $r = a$  gives

$$\mathbf{v}|_{S_p} = \mathbf{v}^{(0)}\Big|_{r=a} + \epsilon \left( \mathbf{v}^{(1)}\Big|_{r=a} + a \mathbf{A}_n \boxed{n} \mathbf{P}_n \frac{\partial \mathbf{v}^{(0)}}{\partial r}\Big|_{r=a} \right) + O(\epsilon^2) \quad (3.32)$$

A similar expansion of the temperature gradient  $\nabla T_s$  on  $S_p$  about  $r = a$  yields

$$\nabla T_s|_{S_p} = \nabla T_s^{(0)}\Big|_{r=a} + \epsilon \left( \nabla T_s^{(1)}\Big|_{r=a} + a \mathbf{A}_n \boxed{n} \mathbf{P}_n \frac{\partial \nabla T_s^{(0)}}{\partial r}\Big|_{r=a} \right) + O(\epsilon^2) \quad (3.33)$$

Substitution of Equations 3.4, 3.32 and 3.33 into Equation 3.31 furnishes the following  $O(1)$  and  $O(\epsilon)$  boundary conditions at  $r = a$ :

$$\mathbf{v}^{(0)}\Big|_{r=a} = C_s (\mathbf{I} - \hat{\mathbf{r}}\hat{\mathbf{r}}) \cdot \nabla T_s^{(0)}\Big|_{r=a} \quad (3.34)$$

and

$$\begin{aligned} \mathbf{v}^{(1)}\Big|_{r=a} = & - a \mathbf{A}_n \boxed{n} \mathbf{P}_n \frac{\partial \mathbf{v}^{(0)}}{\partial r}\Big|_{r=a} + C_s \left\{ \hat{\mathbf{r}} \hat{\nabla} (\mathbf{P}_n \boxed{n} \mathbf{A}_n) \right. \\ & + \left. \hat{\nabla} (\mathbf{P}_n \boxed{n} \mathbf{A}_n) \hat{\mathbf{r}} \right\} \cdot \nabla T_s^{(0)}\Big|_{r=a} + C_s (\mathbf{I} - \hat{\mathbf{r}}\hat{\mathbf{r}}) \cdot \nabla T_s^{(1)}\Big|_{r=a} \\ & + C_s a (\mathbf{A}_n \boxed{n} \mathbf{P}_n) (\mathbf{I} - \hat{\mathbf{r}}\hat{\mathbf{r}}) \cdot \frac{\partial}{\partial r} \nabla T_s^{(0)}\Big|_{r=a} \end{aligned} \quad (3.35)$$

The leading-order velocity field, which vanishes at infinity and is subject to the thermal slip condition, given by Equation 3.34 taken in conjunction with the leading-order temperature gradient on  $S_p$  from Equation 3.24, corresponds to the flow around an undeformed sphere. It is found, using the method of Ref. [83], to be

$$\mathbf{v}^{(0)} = \frac{3C_s}{2 + \gamma} \left[ \left( \frac{a}{2r} + \frac{a^3}{2r^3} \right) \mathbf{I} + \left( \frac{a}{2r} - \frac{3a^3}{2r^3} \right) \hat{\mathbf{r}}\hat{\mathbf{r}} \right] \cdot \mathbf{G} \quad (3.36)$$

Equations 3.24 and 3.36 in combination with Equation 3.35 yield

$$\begin{aligned} \mathbf{v}^{(1)}\Big|_{r=a} = & \frac{6C_s}{2 + \gamma} (\mathbf{A}_n \boxed{n} \mathbf{P}_n) (\mathbf{I} - 2\hat{\mathbf{r}}\hat{\mathbf{r}}) \cdot \mathbf{G} \\ & + \frac{3C_s}{2 + \gamma} \left[ \hat{\mathbf{r}} \hat{\nabla} (\mathbf{P}_n \boxed{n} \mathbf{A}_n) + \hat{\nabla} (\mathbf{P}_n \boxed{n} \mathbf{A}_n) \hat{\mathbf{r}} \right] \cdot \mathbf{G} \\ & + C_s (\mathbf{I} - \hat{\mathbf{r}}\hat{\mathbf{r}}) \cdot \nabla T_s^{(1)}\Big|_{r=a} \end{aligned} \quad (3.37)$$

We have now obtained the governing equations and concomitant boundary conditions for the  $O(\epsilon)$  temperature and velocity problems. However, the completely general solution of these problems, requiring use of general recurrence relations relating the various polyadic surface harmonics and their gradients, is extremely complicated algebraically. Accordingly, in lieu of attempting a completely general calculation, we instead provide the solution only for the specific case of a general triaxial ellipsoid by way of illustrating the general scheme.

### 3.5 Nonisothermal Flow around an Ellipsoid

Consider the ellipsoid,

$$\left( \frac{x_1}{a_1} \right)^2 + \left( \frac{x_2}{a_2} \right)^2 + \left( \frac{x_3}{a_3} \right)^2 = 1 \quad (3.38)$$

where  $(x_1, x_2, x_3)$  are Cartesian coordinates fixed in the ellipsoid, with the coordinate axes pointing along the principal axes of the ellipsoid, and with  $(a_1, a_2, a_3)$  the semi-lengths of these axes. Oblate and prolate spheroids, for which two of the three principal axes are equal, are obtained as special

cases of the ellipsoid, while a circular disk and a needle-shaped object may be approximated by an oblate and a prolate spheroid, respectively, one of whose semi-axes shrinks to zero.

In invariant form, the equation of the ellipsoid may be expressed as [84]

$$\mathbf{r} \cdot \mathbf{D} \cdot \mathbf{r} = 1 \quad (3.39)$$

where  $\mathbf{D}$  is the body-fixed dyadic

$$\mathbf{D} = \frac{\mathbf{i}_1 \mathbf{i}_1}{a_1^2} + \frac{\mathbf{i}_2 \mathbf{i}_2}{a_2^2} + \frac{\mathbf{i}_3 \mathbf{i}_3}{a_3^2} \quad (3.40)$$

in which  $(\mathbf{i}_1, \mathbf{i}_2, \mathbf{i}_3)$  are body-fixed Cartesian unit vectors directed along the principal axes of the ellipsoid. Consider the case where the ellipsoid is a slightly deformed sphere, with the semi-lengths of the principal axes given by  $a_1 = a(1 + \epsilon\alpha_1)$ ,  $a_2 = a(1 + \epsilon\alpha_2)$  and  $a_3 = a(1 + \epsilon\alpha_3)$ , where  $\epsilon \ll 1$ . Since  $\mathbf{i}_1 \mathbf{i}_1 + \mathbf{i}_2 \mathbf{i}_2 + \mathbf{i}_3 \mathbf{i}_3 = \mathbf{I}$ , it follows that

$$\mathbf{D} = \frac{\mathbf{I}}{a^2} - \frac{2\epsilon}{a^2} \mathbf{B} + O(\epsilon^2) \quad (3.41)$$

where  $\mathbf{B}$  is the body-fixed dyadic

$$\mathbf{B} = \alpha_1 \mathbf{i}_1 \mathbf{i}_1 + \alpha_2 \mathbf{i}_2 \mathbf{i}_2 + \alpha_3 \mathbf{i}_3 \mathbf{i}_3 \quad (3.42)$$

For a given ellipsoid, whose volume is  $V = 4\pi a_1 a_2 a_3 / 3$ , it is convenient to choose the radius  $a$  of the sphere such that its volume,  $4\pi a^3 / 3$ , is equal to that of the ellipsoid; that is,  $a^3 = a_1 a_2 a_3$ . Since  $a_i = a(1 + \epsilon\alpha_i)$ , this requires that  $\alpha_1 + \alpha_2 + \alpha_3 = 0$ , i.e.,  $\mathbf{I} : \mathbf{B} = 0$ , or, alternatively,

$$\text{Tr}(\mathbf{B}) = 0 \quad (3.43)$$

where, for any dyadic  $\mathbf{B}$ ,  $\text{Tr}(\mathbf{B})$  denotes the trace,  $\mathbf{B} : \mathbf{I}$ .

Upon combining Equations 3.39 and 3.41 and making use of the symmetry of  $\mathbf{B}$  together with the identity  $\hat{\mathbf{r}} \hat{\mathbf{r}} = 2\mathbf{P}_2(\hat{\mathbf{r}})/3 + \mathbf{I}/3$ , we obtain

$$r = a \left[ 1 + \frac{2}{3} \epsilon \mathbf{B} : \mathbf{P}_2(\hat{\mathbf{r}}) + O(\epsilon^2) \right] \quad (3.44)$$

$\mathbf{B}$  is diagonal, and, hence, symmetric in the body-fixed coordinate system. As a result, it is symmetric in any basis.

The detailed derivation of the  $O(\epsilon)$  temperature fields outside and within the ellipsoid is presented in Appendix B. The resulting solutions are

$$\mathbf{T}^{(1)} = -\frac{6}{5} \left( \frac{1-\gamma}{2+\gamma} \right)^2 \frac{a^3}{r^2} \mathbf{P}_1 \cdot \mathbf{B} + \frac{6}{5} \left( \frac{1-\gamma}{2+\gamma} \right) \frac{a^5}{r^4} \mathbf{P}_3 : \mathbf{B} \quad (3.45)$$

and

$$\mathbf{T}_s^{(1)} = -\frac{18}{5} \frac{1-\gamma}{(2+\gamma)^2} \mathbf{r} \cdot \mathbf{B} \quad (3.46)$$

The  $O(\epsilon)$  boundary condition on velocity, Equation 3.37, thus reduces to

$$\mathbf{v}^{(1)}\Big|_{r=a} = \frac{2C_s}{2+\gamma} \left[ 2\mathbf{B} : \mathbf{P}_2 (\mathbf{I} - 2\hat{\mathbf{r}}\hat{\mathbf{r}}) + \hat{\mathbf{r}}\hat{\nabla}\mathbf{P}_2 : \mathbf{B} + \hat{\nabla}(\mathbf{P}_2 : \mathbf{B})\hat{\mathbf{r}} - \frac{9}{5} \left( \frac{1-\gamma}{2+\gamma} \right) (\mathbf{I} - \hat{\mathbf{r}}\hat{\mathbf{r}}) \cdot \mathbf{B} \right] \cdot \mathbf{G} \quad (3.47)$$

The force on the ellipsoid can be obtained without solving the detailed boundary value problem by making use of the following expression for the force on a body of arbitrary shape [75]:

$$\mathbf{F} = -\frac{3}{2}\mu a \int_{S_1} \mathbf{v}|_{r=a} d\Omega \quad (3.48)$$

where the integration is to be carried out over the surface of a unit sphere,  $S_1$ , and wherein  $d\Omega = d^2\hat{\mathbf{r}}$  is a differential element of solid angle. The analogous expression for the torque on the body about the origin is [75]:

$$\mathbf{T} = 3\mu a^2 \boldsymbol{\varepsilon} : \int_{S_1} \hat{\mathbf{r}} \mathbf{v}|_{r=a} d\Omega \quad (3.49)$$

where  $\boldsymbol{\varepsilon} = -\mathbf{I} \times \mathbf{I}$  is the alternating unit triadic. Following Ref. [74], we introduce the translational hydrodynamic resistance dyadic  $\mathbf{K}$  via the expression

$$\mathbf{F} = -\mu \mathbf{K} \cdot \mathbf{G} \quad (3.50)$$

Expansion of  $\mathbf{F}$  and  $\mathbf{K}$  in powers of  $\epsilon$  gives, for the leading-order terms,

$$\mathbf{F}^{(0)} = -\frac{3}{2}\mu a \int_{S_1} \mathbf{v}^{(0)}\Big|_{r=a} d\Omega = -\mu \mathbf{K}^{(0)} \cdot \mathbf{G} \quad (3.51)$$

whence, from Equation 3.34 [cf. Chapter 2],

$$\mathbf{K}^{(0)} = \frac{9C_s a}{2(2+\gamma)} \int_{S_1} (\mathbf{I} - \hat{\mathbf{r}}\hat{\mathbf{r}}) d\Omega = \frac{12\pi C_s a}{2+\gamma} \mathbf{I} \quad (3.52)$$

in which we have used the identity  $\int_{S_1} (\mathbf{I} - \hat{\mathbf{r}}\hat{\mathbf{r}}) d\Omega = 8\pi\mathbf{I}/3$ . Similarly, for the first-order terms, we find that

$$\mathbf{F}^{(1)} = -\frac{3}{2}\mu a \int_{S_1} \mathbf{v}^{(1)}\Big|_{r=a} d\Omega = -\mu \mathbf{K}^{(1)} \cdot \mathbf{G} \quad (3.53)$$

where

$$\mathbf{K}^{(1)} = \frac{3C_s a}{2 + \gamma} \left[ 2 \int_{S_1} \mathbf{P}_2 (\mathbf{I} - 2\hat{\mathbf{r}}\hat{\mathbf{r}}) : \mathbf{B} d\Omega + \int_{S_1} \hat{\mathbf{r}} \hat{\nabla} \mathbf{P}_2 : \mathbf{B} d\Omega + \int_{S_1} \hat{\nabla} \mathbf{P}_2 : \mathbf{B} \hat{\mathbf{r}} d\Omega - \frac{9}{5} \left( \frac{1 - \gamma}{2 + \gamma} \right) \int_{S_1} (\mathbf{I} - \hat{\mathbf{r}}\hat{\mathbf{r}}) \cdot \mathbf{B} d\Omega \right] \quad (3.54)$$

Details pertaining to the calculation of  $\mathbf{K}^{(1)}$  are given in Appendix B, with the result being

$$\mathbf{K}^{(1)} = -\frac{24\pi}{5} C_s a \frac{1 - 4\gamma}{(2 + \gamma)^2} \mathbf{B} \quad (3.55)$$

We have now obtained the force acting on the stationary ellipsoid due to the thermal creep-induced flow. When the ellipsoid moves through the fluid at a velocity of  $\mathbf{U}$ , the preceding solution is superposed on the additional Stokes flow  $(\mathbf{v}', p')$  satisfying the boundary conditions

$$\begin{aligned} \mathbf{v}' &= \mathbf{U} \text{ on } S_p \\ \mathbf{v}'(r \rightarrow \infty) &\rightarrow \mathbf{0} \end{aligned} \quad (3.56)$$

Analogous to Equations 3.34 and 3.47, we require that

$$\begin{aligned} \mathbf{v}'^{(0)} \Big|_{r=a} &= \mathbf{U} \\ \mathbf{v}'^{(1)} \Big|_{r=a} &= -a \mathbf{A}_n \boxed{n} \mathbf{P}_n \frac{\partial \mathbf{v}'^{(0)}}{\partial r} \Big|_{r=a} \end{aligned} \quad (3.57)$$

The leading-order velocity field  $\mathbf{v}'^{(0)}$  in invariant form is given by the expression [74, 83]

$$\mathbf{v}'^{(0)} = \left[ \frac{3a}{4r} (\mathbf{I} + \hat{\mathbf{r}}\hat{\mathbf{r}}) + \frac{a^3}{4r^3} (\mathbf{I} - 3\hat{\mathbf{r}}\hat{\mathbf{r}}) \right] \cdot \mathbf{U} \quad (3.58)$$

which, in combination with Equation 3.57, yields

$$\mathbf{v}'^{(1)} \Big|_{r=a} = \frac{3}{2} (\mathbf{A}_n \boxed{n} \mathbf{P}_n) (\mathbf{I} - \hat{\mathbf{r}}\hat{\mathbf{r}}) \cdot \mathbf{U} \quad (3.59)$$

At leading order, the force on the ellipsoid is given by Stokes' law,  $\mathbf{F}'^{(0)} = -6\pi\mu a \mathbf{U}$ , whereas at  $O(\epsilon)$ , we obtain

$$\mathbf{F}'^{(1)} = -\frac{3\mu a}{2} \int_{S_1} \mathbf{v}'^{(1)} \Big|_{r=a} d\Omega = -\mu \mathbf{K}'^{(1)} \cdot \mathbf{U} \quad (3.60)$$

where

$$\begin{aligned}\mathbf{K}'^{(1)} &= \frac{3}{2}a\mathbf{B} : \int_{S_1} \mathbf{P}_2(\mathbf{I} - \hat{\mathbf{r}}\hat{\mathbf{r}}) d\Omega \\ &= -\frac{6\pi}{5}a\mathbf{B}\end{aligned}\quad (3.61)$$

Equation 3.61 is in exact agreement with the corresponding result of Ref. [75] satisfying Equation 3.56, wherein the surface of the deformed sphere was expressed as an expansion in scalar spherical harmonics.

The net force on the ellipsoid is obtained from the superposition of the force acting on a stationary ellipsoid under an externally imposed temperature gradient together with the force acting on an ellipsoid translating at a velocity of  $\mathbf{U}$  under isothermal conditions:

$$\mathbf{F}_{\text{net}} = -\mu(\mathbf{K} \cdot \mathbf{G} + \mathbf{K}' \cdot \mathbf{U}) \quad (3.62)$$

It can be seen from Equations 3.34 and 3.47 that the torque  $\mathbf{T}$  acting on the ellipsoid about its center, given by Equation 3.49, vanishes. Under isothermal conditions, the centroid of the ellipsoid is a center of hydrodynamic stress. The existence of such a center for a nonskew body such as an ellipsoid implies that no torque acts about its centroid as the ellipsoid translates without slip [74].

Accordingly, the force- and torque-free ellipsoid will move, without rotation, under the influence of the externally imposed temperature gradient  $\mathbf{G}$  at a velocity  $\mathbf{U} = -(\mathbf{K}')^{-1} \cdot \mathbf{K} \cdot \mathbf{G}$ , where

$$\mathbf{K}' = 6\pi a \left[ \mathbf{I} - \frac{\epsilon}{5}\mathbf{B} + O(\epsilon^2) \right] \quad (3.63)$$

and

$$\mathbf{K} = \frac{12\pi C_s a}{2 + \gamma} \left[ \mathbf{I} - \epsilon \frac{2}{5} \left( \frac{1 - 4\gamma}{2 + \gamma} \right) \mathbf{B} + O(\epsilon^2) \right] \quad (3.64)$$

In view of the identity  $[\mathbf{I} + \epsilon\mathbf{C} + O(\epsilon^2)]^{-1} = \mathbf{I} - \epsilon\mathbf{C} + O(\epsilon^2)$ , valid for any dyadic  $\mathbf{C}$ , this makes

$$\mathbf{U} = -\frac{2C_s}{2 + \gamma} \left[ \mathbf{I} + \epsilon \frac{9}{5} \frac{\gamma}{2 + \gamma} \mathbf{B} + O(\epsilon^2) \right] \cdot \mathbf{G} \quad (3.65)$$

This constitutes the principal result of our ellipsoid calculation.

In the special case where the ellipsoid is nonconducting,  $\gamma = 0$ , whereupon the above reduces simply to

$$\mathbf{U} = -C_s \mathbf{G} [1 + O(\epsilon^2)] \quad (3.66)$$

As such, to at least terms of first order in the deformation, the ellipsoid's thermophoretic velocity is independent of its shape, size and orientation and, hence, is identical to that of a sphere. While we have formally demonstrated the latter result only to the first order, according to Morrison's theory this nonconducting result should hold to all orders in the ellipsoid deformation  $\epsilon$ .

### 3.6 Discussion

We have developed an asymptotic solution of flow around a heat-conducting, slightly deformed sphere under an imposed temperature gradient, wherein the fluid slips at the surface of the deformed sphere. Although we have provided an explicit solution only for the case wherein the deformed sphere is an ellipsoid, to first order in the perturbation scheme, the technique may be readily applied to arbitrarily deformed bodies whose deviation from a spherical shape is small. In principle, the perturbation solution can be carried out to any order. For the specific case of nonconducting particles, we confirm Morrison's generic deduction [14] that the phoretic velocity of a particle is independent of its size, shape and orientation.

# *Unraveling of a Tethered Polymer Chain in Uniform Solvent Flow*

---

This Chapter is reproduced in part with permission from A. Mohan and P. S. Doyle, “Unraveling of a tethered polymer chain in uniform solvent flow,” *Macromolecules* **40**, 4301–4312 (2007). Copyright © 2007 by the American Chemical Society.

## **4.1 Introduction**

The transient unraveling of a polymer chain following a polymer–obstacle collision and the formation of a hooked chain configuration are features common to several size-based DNA separation techniques, including microfabricated obstacle courses [29], self-assembled magnetic bead arrays [30] and dilute solution capillary electrophoresis [25, 26]. In the present Chapter, we model the unraveling process following chain–obstacle collision under the application of an electric field as being equivalent to the unraveling of a tethered polymer chain in a uniform solvent flow field. This equivalence may be rationalized as detailed in the next paragraph.

Under the assumption that the unraveling and unhooking events are decoupled, the unraveling of each arm of the chain following its collision with an obstacle may be modeled as being equivalent to the stretching of a chain tethered to the obstacle under an imposed field. Such a decoupling is

allowed for even in the event that the long arm simultaneously unravels as the chain is unhooking from the obstacle, provided that the tension propagation in the long arm is significantly faster than the ropelike unhooking motion of the chain [41]. Additionally, we invoke the principle of electrohydrodynamic equivalence [43, 85], which states that chain stretching in an electric field is equivalent to that in a uniform hydrodynamic flow field at a flow velocity equal to the free solution electrophoretic velocity of the chain. Such an equivalence holds especially under the free draining conditions assumed in the present study, justified partially by the screening of hydrodynamic interactions in complicated channel geometries. However, more generally, hydrodynamic interactions arising on average from the electric field induced motion of individual polymer segments are screened by the counterion cloud surrounding the polyelectrolytic DNA molecule over distances exceeding the Debye length [43]. With the above assumptions, a parallel between the stretching of a tethered chain in an electric field and that in a hydrodynamic flow field may be established.

Several studies exist on the steady state properties of a tethered chain in uniform flow. The stretching of a tethered DNA molecule in uniform flow was experimentally visualized and the dependence of steady fractional extension on velocity and chain length obtained by Perkins et al. [46]. Larson et al. [86] performed Monte Carlo simulations of DNA chains used in the experiments of Perkins et al., as well as of longer chains, whereas Cheon et al. [87] employed molecular dynamics simulations of chains of several lengths. These studies concentrated on the steady state behavior of chain extension. Scaling arguments were proposed for the steady extension of a chain modeled as a string of nondraining blobs in uniform flow by Brochard-Wyart [88, 89], based on the trumpet picture for moderate stretching, and the stem-and-flower picture for strong stretching. Several static properties of a tethered chain in a uniform flow field, including end-to-end distance, drag and tension distribution, have been investigated by Zimmermann and his coworkers [90, 91], using the bead-spring model both with and without account for excluded volume and hydrodynamic interactions, and analytical calculations based on the equilibrium configurational distribution or the blob model. These authors employ the Gaussian, FENE and freely jointed chain models.

The dynamics of stretching, however, remain relatively unexplored. Scaling arguments have been proposed by Brochard-Wyart and her coworkers [89, 92] for the transient extension of a tethered chain stretched by the application of a constant force at the free end or by a flow field in the trumpet regime, and for stretching in a flow field and relaxation upon cessation of flow in the stem-and-flower regime. Existing simulation studies of chain dynamics in uniform flow are restricted to the near-equilibrium or near-steady state regimes. Avramova et al. provide a Monte Carlo study of the near-equilibrium stretching of a chain upon the imposition of flow and its relaxation following the cessation of flow [93]. Conformational fluctuations of tethered Rouse and FENE chains in flow at steady state have been studied in detail by Rzehak and Zimmermann [94, 95] and Rzehak [96]. A few recent studies have theoretically treated tension propagation in stiff polymers under external fields [97], and in semiflexible polymers under the application of a pulling force [98]. However, a description of the transient stretching of a semiflexible, wormlike chain in flow is lacking.

The aim of the present investigation is to provide a comprehensive study of chain unraveling in uniform flow. One of our objectives is to test the assumption of convective tension propagation in a chain unraveling in an external field, which was hypothesized by Randall and Doyle in their study of single chain-obstacle collisions [41]. The Rouse model is selected for its analytical tractability. The consequences of finite extensibility are examined via Brownian dynamics simulations of DNA chains described by the wormlike chain model, in the absence of other nonlinear effects such as excluded volume and hydrodynamic interactions. In Section 4.2, we describe the problem under consideration

and the methods of analysis adopted. Analytical results for the Rouse model are presented in Section 4.3. Section 4.4 provides a comparison between the behavior of Rouse and wormlike chains, and describes the scaling behavior of the latter model. Results for tension propagation in Rouse and wormlike chains are presented in Section 4.5. Section 4.6 contains a summary of our findings.

## 4.2 Problem Definition and Methodology

In this study, we employ the bead–spring model of the polymer chain, whereby the chain is discretized into  $N$  beads, indexed from 0 to  $N - 1$ , with each pair of adjacent beads connected by a spring. The first bead of the chain is held tethered. The chain is initially in an equilibrium, coiled configuration, and at time  $t = 0$ , a uniform flow of solvent is imposed, with  $\mathbf{v} = v\hat{\mathbf{x}}$  denoting the unperturbed solvent velocity, and  $\hat{\mathbf{x}}$  the unit vector in the flow direction. Under the free draining assumption, the set of Langevin equations [cf. Equation 1.23] governing the evolution of the chain is

$$d\mathbf{r}_0 = 0 \quad (4.1)$$

$$d\mathbf{r}_j = \left( \mathbf{v} + \frac{1}{\zeta} \mathbf{F}_j^{\text{det}} \right) dt + \sqrt{\frac{2k_B T}{\zeta}} d\mathbf{W}_j, \quad j = 1, \dots, N - 1 \quad (4.2)$$

where  $\mathbf{r}_i$ ,  $i = 0, \dots, N - 1$ , denotes the position vector of bead  $i$  relative to the origin, chosen here to lie at the location of the tethered bead ( $\mathbf{r}_0 = \mathbf{0}$ ). In the absence of excluded volume interactions and external forces,  $\mathbf{F}_j^{\text{det}}$  is identical to the spring force exerted on bead  $j$  by the adjoining springs. The drag coefficient  $\zeta$  for a single bead is given by Stokes' law, and  $k_B T$  denotes the thermal energy. The terms  $\mathbf{W}_j$  represent the three-dimensional Wiener processes introduced in Section 1.2 possessing the properties  $\langle d\mathbf{W}_j(t) \rangle = \mathbf{0}$  and  $\langle d\mathbf{W}_i(t) d\mathbf{W}_j(t') \rangle = dt \delta_{ij} \delta(t - t') \boldsymbol{\delta}$ , where  $i, j = 1, \dots, N - 1$  and  $\boldsymbol{\delta}$  is the identity tensor.

We consider DNA molecules of five lengths, namely,  $\lambda$ -DNA (having a contour length of  $21 \mu\text{m}$  when stained with YOYO dye in the ratio of 4 base pairs of DNA per molecule of dye),  $2\lambda$ -DNA,  $4\lambda$ -DNA,  $6\lambda$ -DNA and  $10\lambda$ -DNA. The persistence length of DNA, assumed unchanged on staining, is known to be  $53 \text{ nm}$ . We maintain a constant level of discretization in our study, and vary the number of beads  $N$  in the bead–spring model to accommodate chains of different lengths. As a compromise between achieving satisfactory resolution of the chain into springs while concurrently ensuring an acceptable computational speed, we select a discretization of  $N_{k,s} = 19.8$  Kuhn lengths per spring.

We employ the modified Marko–Siggia force law, given by Equation 1.11, and adopt the ratio  $\lambda = 1.1$  of the effective persistence length to the true persistence length, found by Underhill and Doyle to eliminate errors at 50% mean fractional chain extension [55]. In the linear regime corresponding to  $Q \ll Q_0$ , the modified Marko–Siggia force law reduces to Hooke's law with a spring constant of  $H = 3k_B T / (\lambda b_k^2 N_{k,s})$ , employed in our solution of the Rouse model.

We characterize the strength of the solvent flow by means of a Peclet number, defined as  $\text{Pe} = vN\zeta / (k_B T / b_k)$ , physically equivalent to the dimensionless drag force acting on a chain of  $N$  beads. The diffusivity underlying our definition of  $\text{Pe}$  is, therefore, that of an unconstrained, free draining chain of  $N$  beads as given by  $D = k_B T / (N\zeta)$ . (However, in the limit of large  $N$ , the difference between the use of  $N$  or  $N - 1$  in the definition of the Peclet number and elsewhere is immaterial. Such differences will be ignored throughout this study.) This definition of the Peclet

number is motivated by the observation that the fractional chain extension at steady state is a universal function of the drag force acting on the chain, regardless of chain length [46, 86, 90]. Furthermore, steady state results for a tethered freely jointed chain are known to reduce to the corresponding results for a Gaussian chain in situations wherein  $Pe \ll 1$  [90]. Therefore, we may expect a crossover from the linear, near-equilibrium regime to a regime of strong chain stretching dominated by finite extensibility at a Peclet number of the order of 1. In the present investigation, we consider a range of Peclet numbers from 1 to 100. Assuming a temperature of 298 K, a Peclet number of 100 corresponds to a drag force of 4 pN on a DNA chain, which falls significantly below the value of 65 pN at which the stretching phase transition occurs. The Marko–Siggia law remains valid for DNA molecules stretched to an extension of up to 97%, or up to a Peclet number of  $Pe = 600$  [52].

Equations 4.1 and 4.2, with the spring force law given by Hooke’s law in the Rouse model, reduce to a linear set of Langevin equations, and are amenable to an analysis into normal modes. The wormlike chain model is treated via Brownian dynamics simulations. Initial equilibrium configurations are generated by employing the Marko–Siggia force law to simulate the evolution to equilibrium of Gaussian coils. The radius of gyration of an initially Gaussian configuration converges to its steady, equilibrium value within 5 relaxation times for all the simulated chain lengths, and the resulting configuration is subsequently sampled at intervals of 1 relaxation time to obtain starting configurations for our simulations. We adopt the semi-implicit predictor–corrector scheme of Ref. [63] for the integration of Equation 4.2. A time step of  $5 \times 10^{-4} \zeta Q_0^2 / (k_B T)$  is used. The equilibrium radius of gyration and chain stretch of  $\lambda$ -DNA in the absence of flow were found to vary by less than 2% upon reducing the time step by a factor of 5. Averages are performed over an ensemble of 100 chains. Upon doubling the ensemble size to 200 chains, the equilibrium radius of gyration and chain stretch were found to differ by less than 1% from the corresponding values obtained from an ensemble of 100 chains for  $\lambda$ -DNA in the absence of flow, with thermal noise being further attenuated in the presence of flow. However, in order to facilitate an accurate determination of the instantaneous chain length under tension in flow, the results presented for a 61-bead wormlike chain at  $Pe = 10$  and  $Pe = 30$  derive from ensemble sizes of 10 000 and 1 000, respectively.

Except where dimensional notation proves convenient, nondimensional variables will be employed in the remainder of this study, and will be denoted by the symbol “ $\tilde{\phantom{x}}$ ” surmounting the corresponding dimensional variable. We utilize a length scale of  $Q_0$  and a time scale of  $\zeta Q_0^2 / (k_B T)$ . Consequently, the unit of force employed by us is  $k_B T / Q_0$ , with the spring constant expressed in units of  $k_B T / Q_0^2$ .

### 4.3 The Rouse Model

In this Section, we summarize our results for the end-to-end distance and the tension distribution in a Rouse chain, and highlight their relevant features. The details of the normal mode solution are relegated to Appendix C. We obtain

$$\tilde{L}_e = \frac{Pe N_{k,s}}{\tilde{H}} \frac{1}{N} \sum_{m,j=1}^{N-1} \Omega_{N-1,m} \Omega_{jm} \frac{1 - \exp(-\tilde{H} a_m \tilde{t})}{a_m} \quad (4.3)$$

$$\tilde{F}_{\text{spr } 1, x} = \text{Pe} \frac{N_{k,s}}{N} \sum_{m,j=1}^{N-1} \Omega_{1m} \Omega_{jm} \frac{1 - \exp(-\tilde{H} a_m \tilde{t})}{a_m} \quad (4.4)$$

and

$$\tilde{F}_{\text{spr } k, x} = \text{Pe} \frac{N_{k,s}}{N} \sum_{m,j=1}^{N-1} (\Omega_{km} - \Omega_{k-1,m}) \Omega_{jm} \frac{1 - \exp(-\tilde{H} a_m \tilde{t})}{a_m}, \quad k = 2, \dots, N-1 \quad (4.5)$$

where  $\tilde{L}_e$  and  $\tilde{F}_{\text{spr } k, x}$  denote, respectively, the mean end-to-end distance and spring tension in spring  $k$  in the flow direction, with the index  $k = 1, \dots, N-1$  measured from the tethered end. The end-to-end distance is measured by the  $x$ -coordinate of the bead at the free end of the chain. The elements of the matrix  $\Omega$ , composed of the normalized eigenvectors of the Rouse matrix, are given by [95]

$$\Omega_{jm} = \frac{1}{\sqrt{\frac{N}{2} - \frac{1}{4}}} \sin\left(\frac{2m-1}{2N-1} \pi j\right) \quad (4.6)$$

corresponding to the eigenvalues

$$a_m = 4 \sin^2\left(\frac{2m-1}{2N-1} \frac{\pi}{2}\right) \quad (4.7)$$

It is evident from Equations 4.3–4.7 that the relaxation times of a tethered Rouse chain may be identified with

$$\tilde{\tau}_m = \frac{1}{\tilde{H} a_m} \quad (4.8)$$

Equations 4.3–4.5 may be simplified by means of elementary trigonometric identities, and the summations  $\sum_j \Omega_{jm}$  and the term  $\Omega_{N-1,m}$  approximated in the limit of large  $N$ , yielding

$$\tilde{L}_e = \frac{\text{Pe} N_{k,s}}{\tilde{H} 4N^2} \sum_{m=1}^{N-1} (-1)^{m+1} \frac{1 - \exp(-\tilde{t}/\tilde{\tau}_m)}{\sin^3\left(\frac{2m-1}{2N-1} \frac{\pi}{2}\right)} \quad (4.9)$$

and

$$\tilde{F}_{\text{spr } k, x} = \text{Pe} \frac{N_{k,s}}{2N^2} \sum_{m=1}^{N-1} \cos\left(\frac{2m-1}{2N-1} (2k-1) \frac{\pi}{2}\right) \frac{1 - \exp(-\tilde{t}/\tilde{\tau}_m)}{\sin^2\left(\frac{2m-1}{2N-1} \frac{\pi}{2}\right)}, \quad k = 1, \dots, N-1 \quad (4.10)$$

The scaling behavior of Rouse chains is manifest in Equations 4.9 and 4.10. Owing to the linearity of the Rouse model, the dependence on  $\text{Pe}$  is trivial. The behavior of the chain extension and tension distribution as  $N$  is varied may be gauged from the fact that the slow modes dominate the dynamics, except very close to  $\tilde{t} = 0$ . This is true particularly as the dependence on  $a_m$ , which rapidly increases with  $m$ , approaching a value of 4 as  $m$  approaches  $N-1$ , arises not only in the decaying exponent but also in the form of inverse powers of  $a_m$  in Equations 4.9 and 4.10. Similar to the case of an unconstrained Rouse chain,  $a_m \sim 1/N^2$  and consequently,  $\tau_m \propto N^2$  for the slow modes ( $m \ll N$ ) and for long chains ( $N \gg 1$ ). It then follows that the chain extension expressed

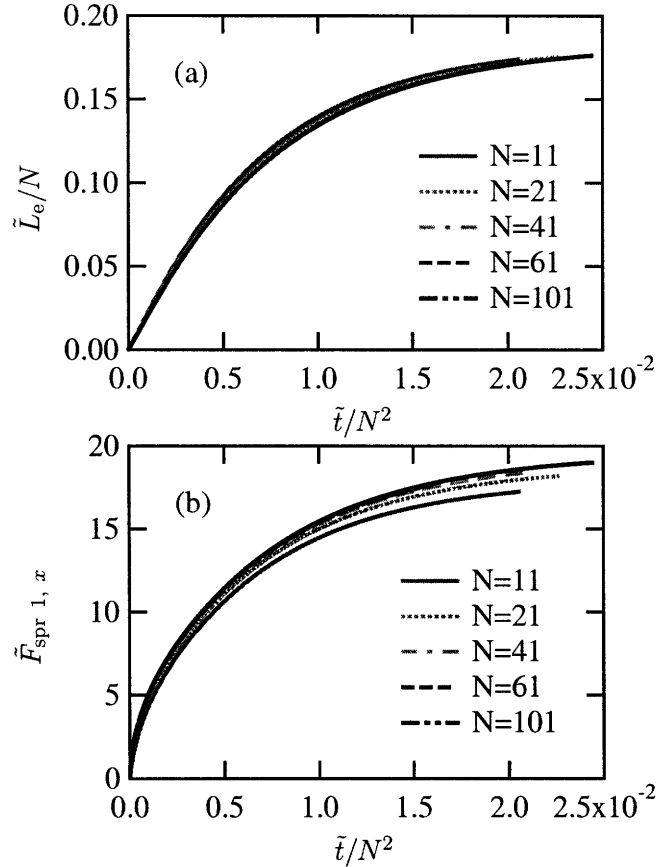


Figure 4.1: *Fractional extension (a) and tension in the first spring (b) as functions of the rescaled time coordinate  $\tilde{t}/N^2$  for Rouse chains of several lengths  $N$  at a Peclet number of 1.*

as a fraction of the contour length, namely,  $\tilde{L}_e/N$ , and the tension in the first spring,  $\tilde{F}_{\text{spr } 1, x}$ , which balances the drag acting on the chain at steady state and is equivalent to the restoring force experienced at the tethered chain end, are universal functions of the rescaled time coordinate  $\tilde{t}/N^2$  at fixed Pe. Similarly, the tension distributions for chains of varying lengths, compared at fixed Pe and at equal values of  $\tilde{t}/N^2$ , collapse when plotted as functions of  $(2k-1)/(2N-1)$ . This behavior is demonstrated in Figures 4.1 and 4.2.

Equation 4.9 reveals that the contributions from the various modes to the chain extension alternate in sign, with the dominant, positive contribution being that of the slowest mode,  $m = 1$ . As a result, Equation 4.9 may be well-approximated by a single exponential relaxation to steady state with time constant  $\tilde{\tau}_1$ , an approximation that marginally overestimates the chain extension (resulting in a maximum error of about 5% for a chain of 61 beads at Pe = 1). The same approximation predicts the spring tensions with varying degrees of accuracy as  $k$  is varied, owing to the fact that the cosine term in Equation 4.10 varies in sign as its argument varies for  $k > 1$ ,

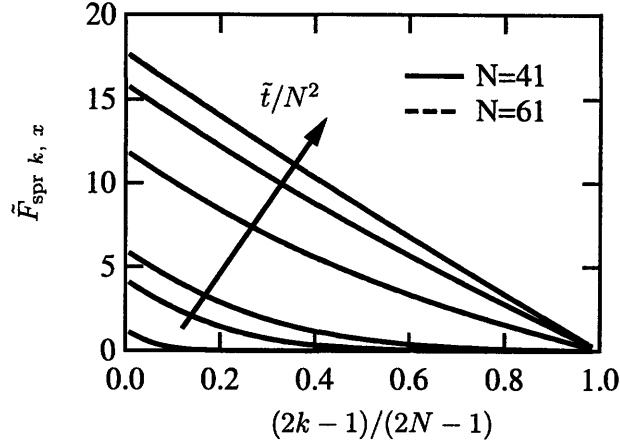


Figure 4.2: *Tension profiles for Rouse chains of 41 and 61 beads as functions of the rescaled spring index  $(2k - 1)/(2N - 1)$  at a Peclet number of 1 at several points in time, compared at  $\tilde{t}/N^2 = 6.0 \times 10^{-5}$ ,  $6.7 \times 10^{-4}$ ,  $1.3 \times 10^{-3}$ ,  $5.4 \times 10^{-3}$ ,  $1.1 \times 10^{-2}$  and  $1.6 \times 10^{-2}$  for both chain sizes.*

resulting in a maximum error of about 20% for the case  $k = 1$  and  $N = 61$  at  $Pe = 1$ . Several modes are required to yield accurate tension profiles, with the use of the first 10 modes being found to adequately capture the shape of the transient tension profiles for the case  $N = 61$ .

Equations 4.3–4.5 lead to simplified predictions in the short time limit of  $\tilde{t} \ll \tilde{\tau}_m$  for all values of  $m$ , yielding the convective behavior  $L_e = vt$  and  $F_{\text{spr } 1, x} = Hvt$  in dimensional units. An initial region of vanishing tension is predicted for the remaining springs, indexed  $k > 1$ . The assumption  $\tilde{t} \ll \tilde{\tau}_{N-1}$  is, however, valid only in an extremely narrow time window. With  $N = 61$ , we obtain  $\tilde{\tau}_{N-1} \simeq 5 \times 10^{-3}$ , leading to a time interval barely discernible in Figure 4.1. The chain extension measured by the end-to-end distance does, however, show convective behavior. This behavior arises from the fact that the bead at the free end of the chain is initially convected by the flow, until the preceding spring begins to deform. This issue is discussed further in Section 4.5.

Single exponential relaxation is predicted by Equations 4.3–4.5 in the long time limit of  $\tilde{t} \gg \tilde{\tau}_2$ , while simultaneously,  $\tilde{t} \geq \tilde{\tau}_1$ . Owing to the existence of almost an order of magnitude difference between the relaxation times of the two slowest modes, the range of validity of this approximation is reasonably large. For instance, for a chain of 61 beads,  $\tilde{\tau}_2 \simeq 3$ , whereas  $\tilde{\tau}_1 \simeq 28$ .

#### 4.4 The Wormlike Chain Model

The approximation of a wormlike spring by a Gaussian spring is valid for spring extensions below approximately 30%, i.e., under near-equilibrium conditions [52]. A comparison between the fractional chain extension and the tension in the first spring predicted by the Rouse and wormlike chain models for  $N = 61$  at Peclet numbers of 1 and 100 is presented in Figures 4.3 and 4.4. The Rouse model is seen to provide a reasonable approximation of a wormlike chain at a Peclet number of 1, but as the Peclet number is increased, deviations from Gaussian behavior are apparent. The seeming agreement between the two models in predicting the chain end-to-end extension, as shown

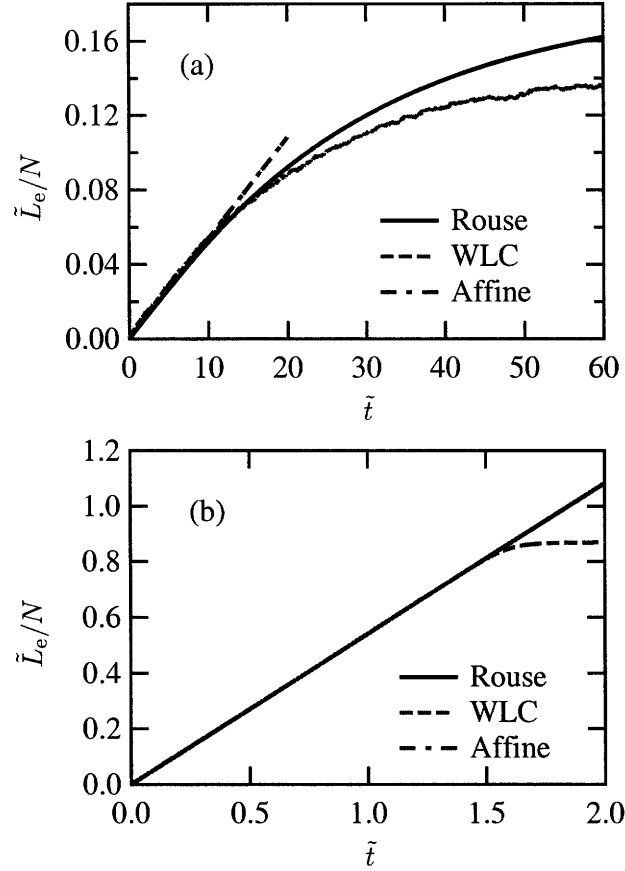


Figure 4.3: *Fractional extension as a function of time for 61-bead Rouse chains and wormlike chains (abbreviated WLC) at Peclet numbers of (a) 1 and (b) 100. Also shown is the fractional extension predicted in the affine deformation limit, namely,  $L_e = vt$ .*

by Figure 4.3, arises due to the convective transport of the free chain end at high Peclet numbers. In particular, at a Peclet number of 100, the affine movement of the chain end of a wormlike chain, leading to the behavior  $L_e = vt$ , is seen to occur almost until steady state is reached.

Figure 4.5 shows the evolution of the fractional chain extension as a function of time nondimensionalized by the convective time scale, i.e.,  $tv/L$ , for a wormlike chain of 61 beads at several flow strengths. The curves initially show affine behavior, corresponding to a line of unit slope passing through the origin. The duration of affine deformation increases with the Peclet number, and in the limit  $Pe \rightarrow \infty$ , affine deformation is expected to occur until steady state. The steady chain extension of a strongly stretched wormlike chain acted upon by a stretching force  $f$  may be estimated from the large force limit of the Marko–Siggia law [cf. Equation 1.10, where the large force limit implies that  $\mathcal{L}/L$  is close to 1 and the dominant term on the right hand side is the last

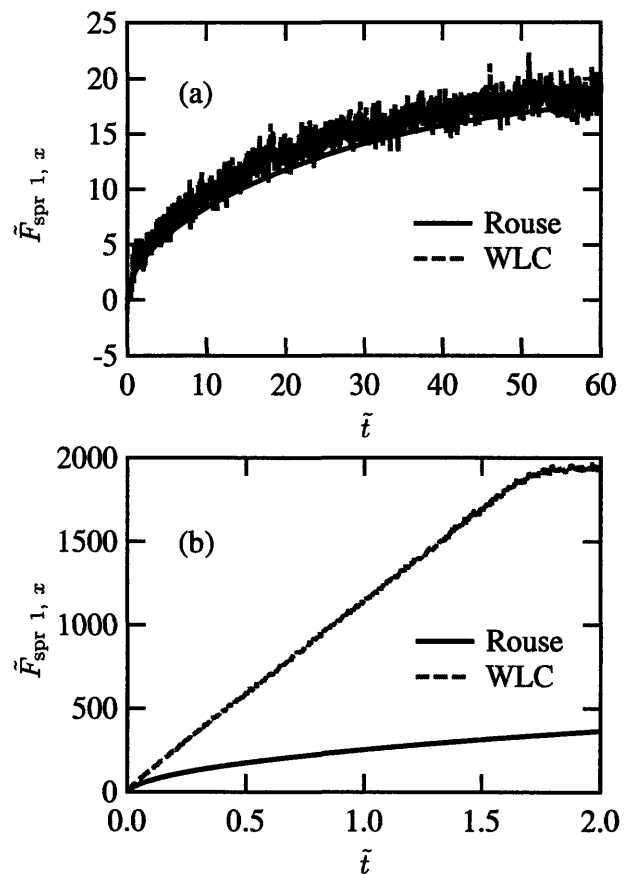


Figure 4.4: Tension in the first spring as a function of time for 61-bead Rouse and wormlike chains at Pecllet numbers of (a) 1 and (b) 100.

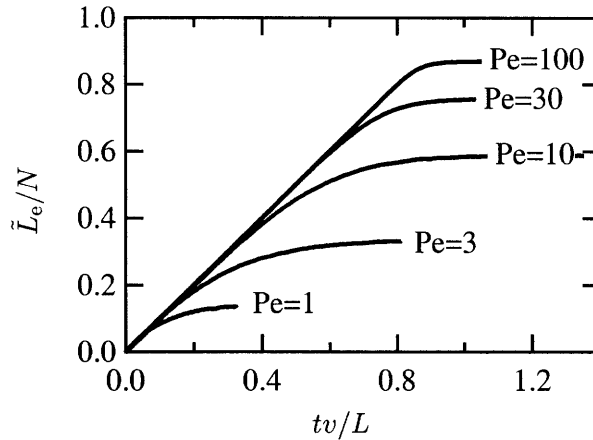


Figure 4.5: Fractional extension as a function of time nondimensionalized by the convective time scale  $L/v$  for a 61-bead wormlike chain at several values of the Peclet number.

term, with  $\mathcal{L} \equiv L_e$  ], given in dimensional form by the expression

$$\frac{fb_k}{k_B T} \simeq \frac{1}{2(1 - L_e/L)^2} \quad (4.11)$$

With the neglect of the nonuniformity in tension along the chain,  $f$  may be replaced by the drag force acting on the chain,  $vN\zeta$ , to yield

$$1 - \frac{L_e}{L} = (2Pe)^{-1/2} \quad (4.12)$$

The components of the spring vectors in the flow direction are plotted against time for several springs of a wormlike chain with  $N = 61$  at  $Pe = 10$  and  $100$  in Figure 4.6. At a moderate Peclet number of 10, the simultaneous, nonlinear deformation of several springs contributes to the chain extension once the spring at the free end of the chain, with  $k = 60$ , begins to deform. On the other hand, at a high Peclet number of 100, spring 60 does not deform almost until steady state is reached. As a result, bead 61 is freely convected, and the chain extension shows affine deformation almost until steady state. The region where nonlinear behavior is manifest in Figure 4.5 shrinks as  $Pe$  is increased.

These features point to the inherent differences between Gaussian and finitely extensible springs. The Gaussian springs close to the tether point of a Rouse chain can extend continuously until the chain extension reaches steady state. On the other hand, the springs of a wormlike chain close to the tether point, where the drag force exerted by flow is maximum, are quickly stretched close to their steady values, after which they exhibit little deformation. These issues also arise in the qualitatively different nature of tension propagation in Rouse and wormlike chains.

Motivated by the scaling behavior of Rouse chains, we next investigate the collapse of data for wormlike chains of different chain lengths. Figures 4.7 and 4.8 demonstrate the collapse of the

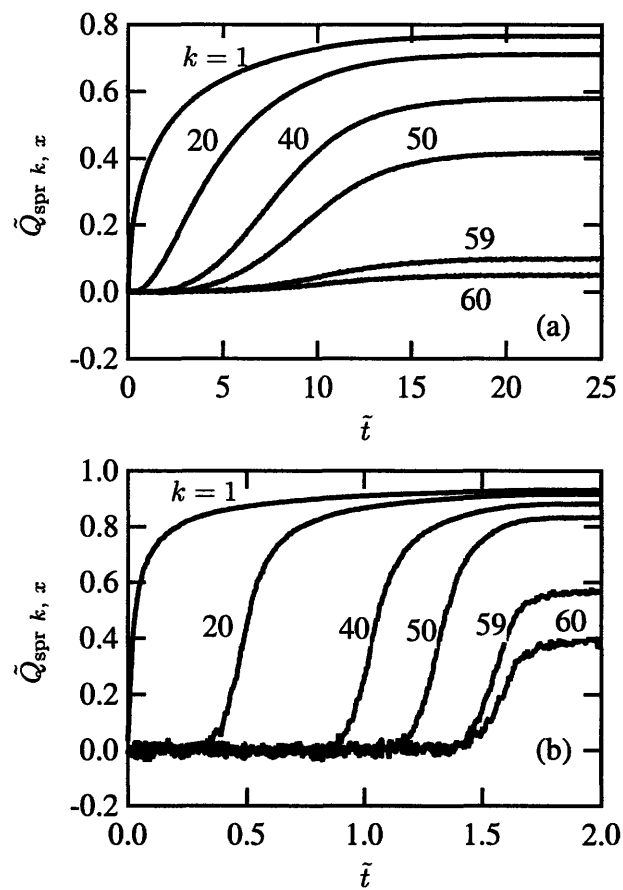


Figure 4.6: Spring extension in the flow direction,  $\tilde{Q}_{\text{spr } k, x}$ , plotted against time for several springs of a 61-bead wormlike chain at Peclet numbers of (a) 10 and (b) 100. The label  $k$  refers to the spring index measured from the tether point.

fractional chain extension and the tension in the first spring, respectively, when plotted as functions of  $\tilde{t}/N^2$  for several chain lengths at three values of the Peclet number. The tension profiles are found to collapse when compared at equal values of  $\tilde{t}/N^2$  for different values of  $N$  on replacing the discrete spring index  $k$  with a continuous measure of distance along the chain,  $k/N$ . This behavior is depicted in Figure 4.9 at  $Pe = 10$  and  $100$ .

## 4.5 Tension Propagation

A strongly stretched wormlike chain exhibits linear tension profiles at all times after an initial period of Gaussian stretching, and a clear demarcation exists between the portion of the chain under tension and the remainder of the chain up to the free end. This moving front remains well-defined with time. Such behavior is clearly manifest in Figure 4.9(b) at a Peclet number of  $100$ . The behavior of the Rouse chain at the same Peclet number may be inferred by exploiting the linearity of the Rouse model to amplify the scale of the  $y$ -axis of Figure 4.2 by a factor of  $100$ . A subsequent comparison with Figure 4.9(b) reveals that tension propagates more gradually in a Rouse chain, as evidenced by its curved tension profiles. The Rouse chain takes longer than the wormlike chain to attain a steady, linear profile. At steady state, the tension in each spring balances the drag on the remainder of the chain up to the free end, and force balance implies that a linear tension profile exists regardless of the spring force law selected. Note that the linearity of the tension profiles at intermediate times indicates that the portion of a wormlike chain under tension at any instant behaves like a shorter, tethered chain at steady state whose length is identical to that of the tension-bearing segment, and that the remainder of the chain not under tension is freely convected by the flow, consequently experiencing no drag.

A further comparison between Rouse and wormlike chains is provided in Figure 4.10. At early time points, the tension profiles of Rouse and wormlike chains are similar, although the springs of a wormlike chain very close to the tether point become highly stretched even at short times at a high Peclet number. Moreover, tension propagates very quickly in a wormlike chain, and the steady, linear tension profile is evident in a wormlike chain even as the Rouse chain continues to deform.

We next investigate the evolution of the chain length under tension with time. For the sake of definiteness, we associate the number of springs under tension, as illustrated in Figure 4.11, with the intercept made by the tangent to the tension profile at the tether point on the  $x$ -axis. Thus, the symbol  $n_t$  denotes the number of springs under tension at time  $t$ , and is determined in a like manner for Rouse and wormlike chains. We allow  $n_t$  to be nonintegral.

Figure 4.12 shows the evolution of  $n_t$  with time for Rouse chains of several lengths. Due to the linearity of the Rouse model,  $n_t$  is independent of the Peclet number, although the spring tensions themselves grow linearly with the Peclet number. The collapse of data for different chain lengths at early time points reveals that while the deformation of the chain starts at the tether point, the springs closer to the free end continue to be convected by the flow for a longer duration. At longer times, a collapse of data is achieved by a rescaling of the axes, as discussed in Section 4.3.

As a simplified model of tension propagation in a Rouse chain, we consider a semi-infinite chain of beads connected by identical linear springs, lying along the positive  $x$ -axis and held fixed at  $x = 0$ . We further assume that the beads are constrained to move only along the  $x$ -axis, and that the random thermal forces acting on the beads are negligible. These assumptions are justified upon the imposition of a solvent flow at an unperturbed velocity of  $v$  in the positive  $x$ -direction at  $t = 0$ .

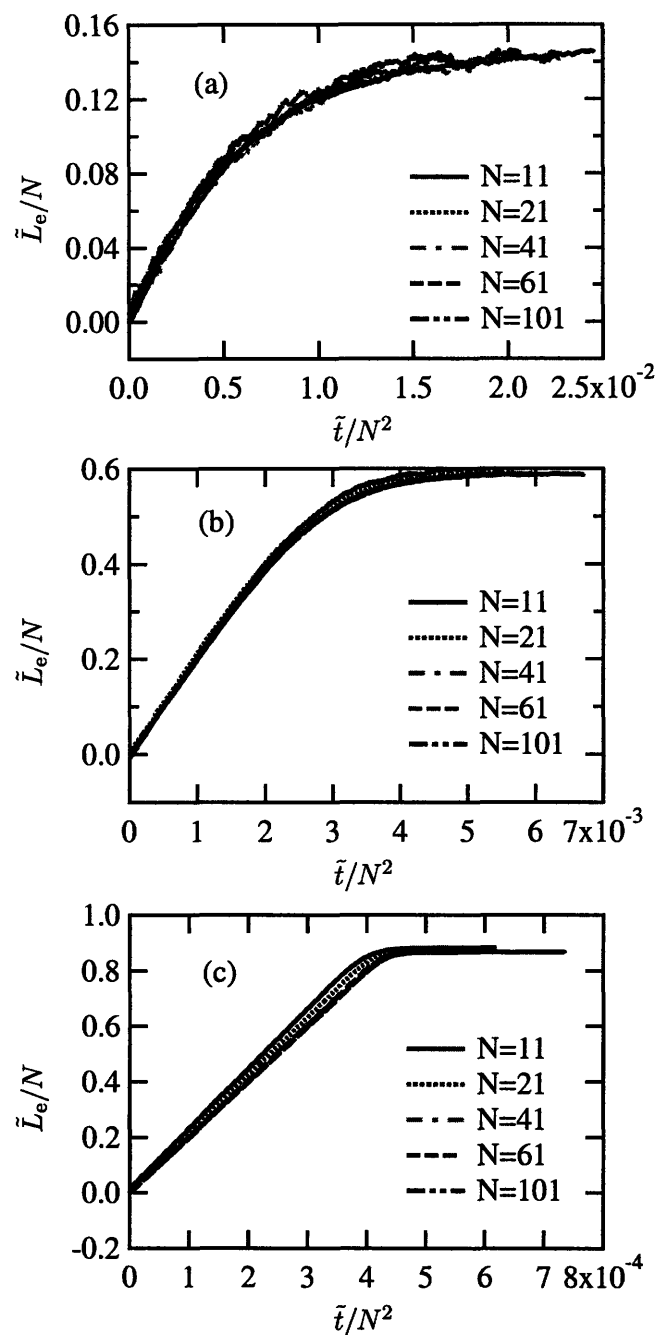


Figure 4.7: Fractional extension as a function of  $\tilde{t}/N^2$  for wormlike chains of several lengths at Peclet numbers of (a) 1, (b) 10 and (c) 100.

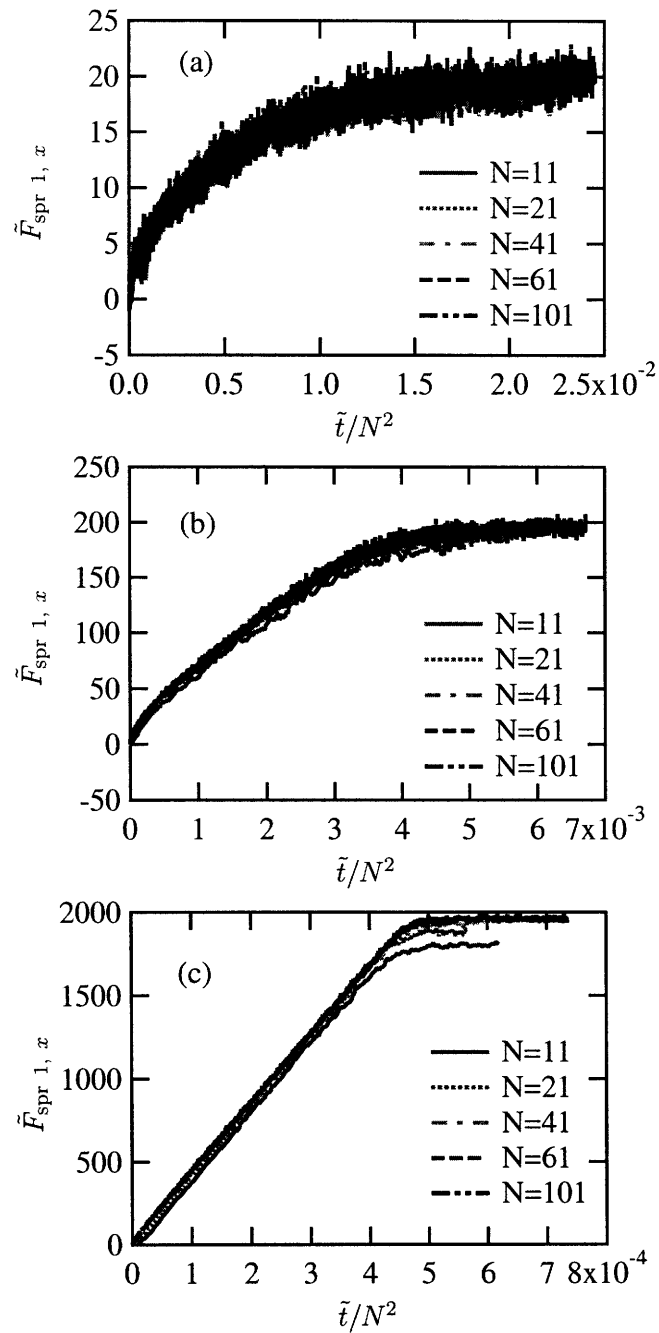


Figure 4.8: Tension in the first spring as a function of  $\tilde{t}/N^2$  for wormlike chains of several lengths at Peclet numbers of (a) 1, (b) 10 and (c) 100.

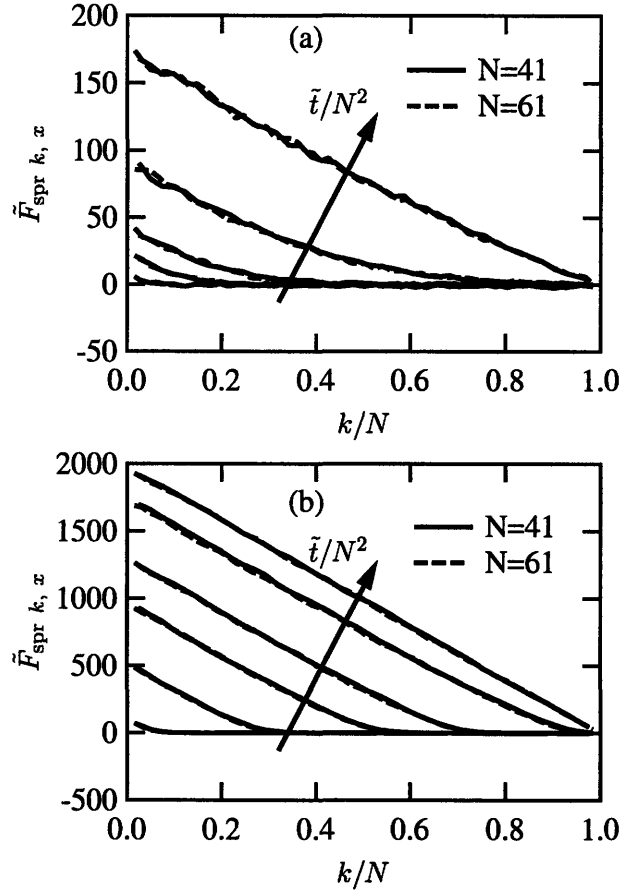


Figure 4.9: Tension profiles for wormlike chains of 41 and 61 beads as functions of the rescaled spring index  $k/N$  at several points in time, compared at equal values of the rescaled time coordinate  $\tilde{t}/N^2$  for both chain sizes at two values of the Peclet number. (a)  $Pe = 10$ ,  $\tilde{t}/N^2 = 1.2 \times 10^{-5}$ ,  $1.3 \times 10^{-4}$ ,  $4.0 \times 10^{-4}$ ,  $1.3 \times 10^{-3}$  and  $3.4 \times 10^{-3}$ . (b)  $Pe = 100$ ,  $\tilde{t}/N^2 = 1.2 \times 10^{-5}$ ,  $1.1 \times 10^{-4}$ ,  $2.1 \times 10^{-4}$ ,  $3.0 \times 10^{-4}$ ,  $4.0 \times 10^{-4}$  and  $5.4 \times 10^{-4}$ .

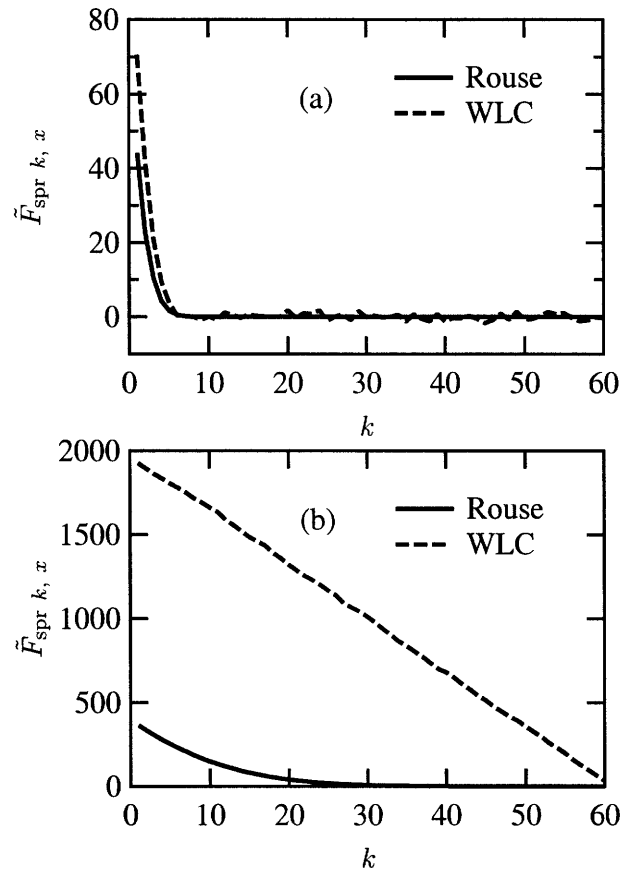


Figure 4.10: *Spring tension as a function of spring index  $k$  for 61-bead Rouse and wormlike chains at a Peclet number of 100 at times (a)  $\tilde{t} = 0.05$  and (b)  $\tilde{t} = 2$ .*

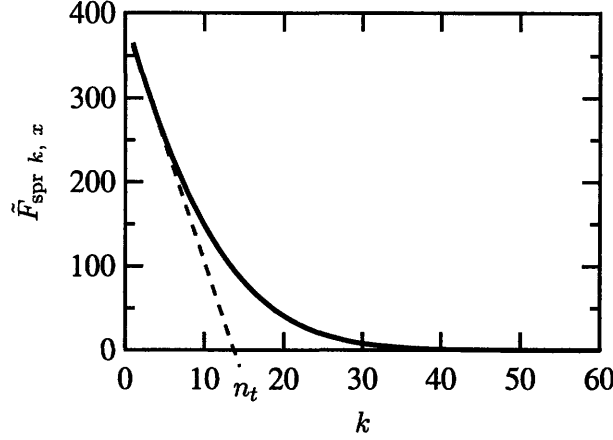


Figure 4.11: *Spring tension as a function of spring index  $k$  for a 61-bead Rouse chain at a Peclet number of 100 and at time  $\tilde{t} = 2$ . The dashed line represents the tangent to the tension profile at the tether point of  $k = 1$ . The intercept made by the tangent on the  $x$ -axis is denoted by  $n_t$ , and is interpreted as the number of springs under tension at time  $\tilde{t}$ .*

Upon going to the continuous limit [50], we obtain the inhomogeneous diffusion equation

$$\frac{\partial s}{\partial t} = \frac{H}{\zeta} \frac{\partial^2 s}{\partial n^2} + v \quad (4.13)$$

governing the bead  $x$ -displacements  $s(n, t)$ , where  $n$ , denoting the bead index, is now treated as a continuous variable analogous to  $x$ . The variable  $s$  in Equation 4.13 is analogous to the temperature of a one dimensional, semi-infinite, heat conducting rod with a constant heat production rate per unit length, and with the temperature at  $x = 0$  being held fixed at the uniform initial temperature of the rod. Equation 4.13 may be solved subject to the boundary condition  $s(n = 0, t) = 0$  and the initial condition  $s(n, t = 0) = 0$ , yielding [99]

$$s(n, t) = \left( vt + \frac{\zeta v}{2H} n^2 \right) \operatorname{erf} \left( \frac{n}{2\sqrt{Ht/\zeta}} \right) + \sqrt{\frac{\zeta v^2 n^2 t}{\pi H}} \exp \left( -\frac{\zeta n^2}{4Ht} \right) - \frac{\zeta v n^2}{2H} \quad (4.14)$$

The growth of  $s(n, t)$ , given by Equation 4.14, is suggestive of the diffusive scaling  $n_t \sim t^{0.5}$ .

Furthermore, Equation 4.14 enables a comparison between the tension profiles obtained from the normal mode analysis of a finite Rouse chain and those following from the continuous approximation of a semi-infinite chain. The tension in spring  $n$  in the continuous limit of the chain is given by the expression  $\tilde{F}_{\text{spr } n, x} = \tilde{H} \partial \tilde{s} / \partial n$  in nondimensional form. Hence, use of Equation 4.14 yields the expression

$$\tilde{F}_{\text{spr } n, x} = \frac{\text{Pe} N_{k,s}}{N} \left[ n \operatorname{erf} \left( \frac{n}{2\sqrt{\tilde{H}\tilde{t}}} \right) + 2\sqrt{\frac{\tilde{H}\tilde{t}}{\pi}} \exp \left( -\frac{n^2}{4\tilde{H}\tilde{t}} \right) - n \right] \quad (4.15)$$

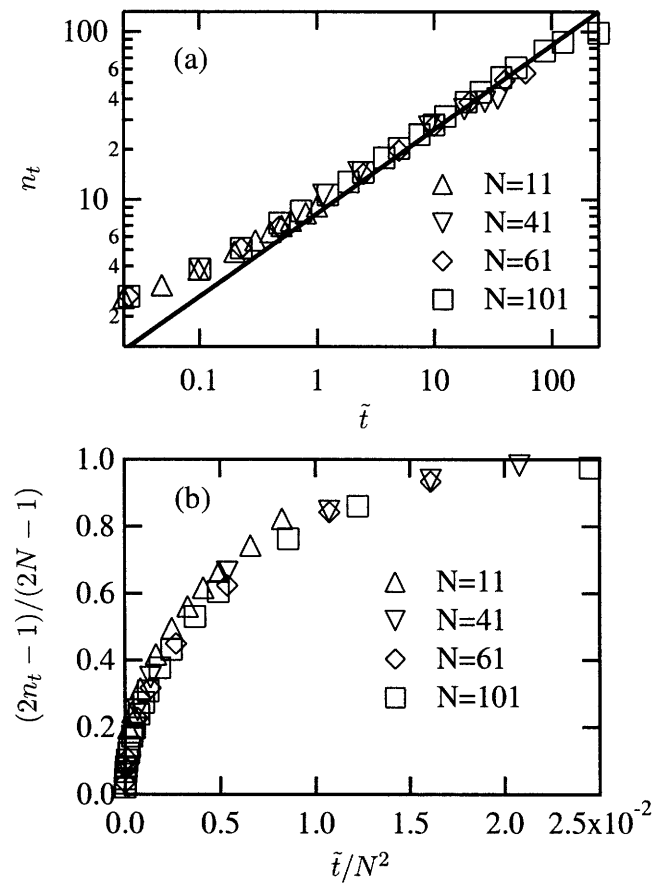


Figure 4.12: *Tension propagation in Rouse chains at a Peclet number of 1. (a)  $n_t$  as a function of time for chains of several lengths (open symbols), and that predicted by Equation 4.17 in the continuous limit of a semi-infinite Rouse chain (solid line). (b) Consequent to the rescaling of both axes, a collapse of data for several chain lengths occurs at long time scales.*

for the spring tensions. A comparison between the tension profiles predicted by Equation 4.15 and those obtained for a chain of 101 beads from Equations 4.4 and 4.5 is illustrated in Figure 4.13 at three time points. The tension profiles predicted in the two cases agree when the finite chain is far from steady state. However, as the finite Rouse chain approaches steady state, it is no longer well-approximated by a semi-infinite chain. As expected, the failure of the approximation at later time points is most evident near the free end of the finite chain.

The tangent  $T_n(\tilde{t})$  to the instantaneous tension profile  $\tilde{F}_{\text{spr } n, x}(\tilde{t})$  from Equation 4.15 at the tethered end  $n = 0$  is of the form

$$T_n(\tilde{t}) = \frac{\text{Pe}N_{k,s}}{N} \left( \sqrt{\frac{4\tilde{H}\tilde{t}}{\pi}} - n \right) \quad (4.16)$$

and consequently,

$$n_t = \sqrt{\frac{4\tilde{H}\tilde{t}}{\pi}} \quad (4.17)$$

Equation 4.17 establishes that tension propagation in a semi-infinite Rouse chain obeys diffusive scaling.

The existence of a power law dependence of  $n_t$  on time for Rouse chains over intermediate time scales is evident from Figure 4.12(a). For chains of lengths  $N = 41, 61$  and  $101$ , the linear region of Figure 4.12(a) exhibits the scaling behavior  $n_t \sim \tilde{t}^\alpha$  over two decades in time, with  $\alpha = 0.43, 0.45$  and  $0.46$ , respectively. Also shown in Figure 4.12(a) is the diffusive behavior predicted by Equation 4.17 in the continuous limit of a semi-infinite Rouse chain. We attribute the deviations from diffusive behavior to errors originating from discretization at early time points until the spring closest to the tether point is stretched significantly (beyond its equilibrium root mean square length). As steady state is approached, the finiteness of the chain length causes deviations from the behavior expected of a semi-infinite chain.

Finally, we test the hypothesis proposed by Randall and Doyle [41] that the length of a tethered DNA chain under tension, denoted here by  $l_t$ , grows linearly in time at a rate equal to the velocity of flow, i.e.,  $l_t = vt$ . We hereafter refer to this model as the convective model of tension propagation. While our simulations of wormlike chains provide us with data on the evolution of  $n_t$  with time, the deduction of the corresponding chain length under tension requires an estimate of the spring extensions. We obtain such an estimate by first assuming that the lengths of all springs in the tension-bearing segment of the chain at any instant are identical. While this assumption may be justified at a high Peclet number (of the order of 100), we expect it to prove less satisfactory at moderate Peclet numbers of the order of 10.

We are now in a position to estimate the number of springs under tension from the convective model. For this purpose, we employ the large force limit of the Marko–Siggia interpolation formula [ cf. Equations 4.11 and 4.12, again with the neglect of the tension variation along the chain], in which  $L_e/L$  is replaced by the fractional spring extension  $l_s/Q_0$ , in conjunction with the hypothesis that  $l_t (= n_t l_s) = vt$ . We thereby obtain the following estimate for the number of springs under tension from the convective model:

$$n_t = \frac{vt/Q_0}{1 - (2\text{Pe})^{-1/2}} \quad (4.18)$$

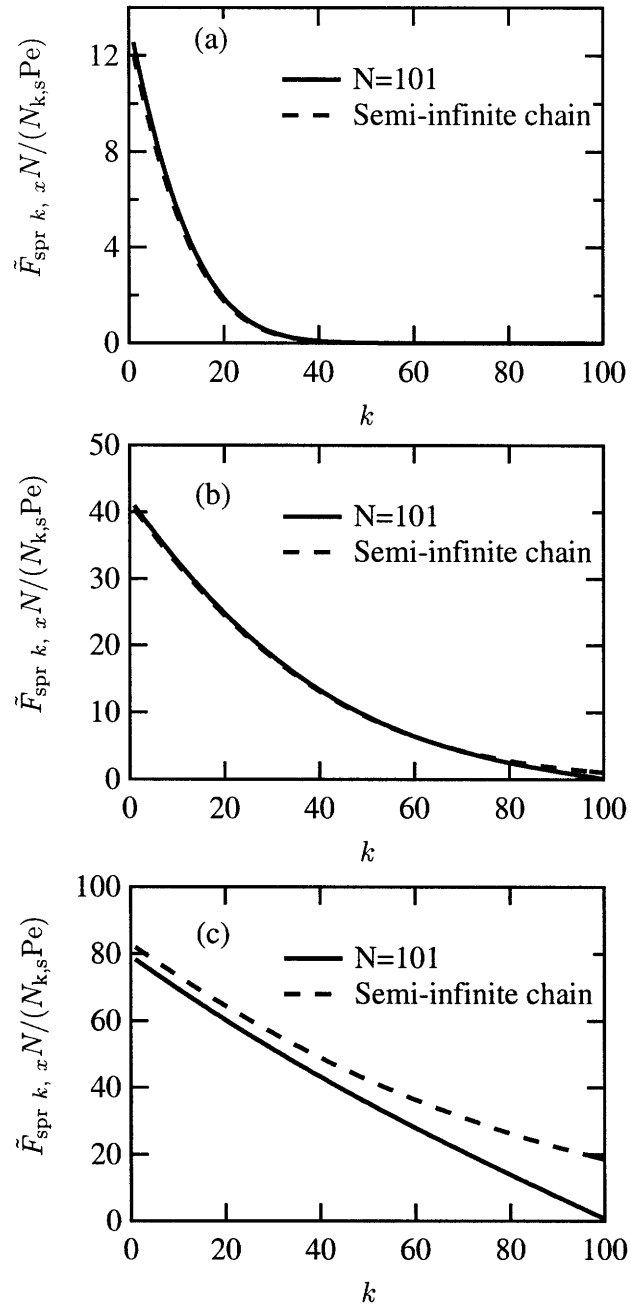


Figure 4.13: Rescaled spring force  $\tilde{F}_{\text{spr } k, x} N / (N_{k,s} \text{Pe})$  as a function of the spring index  $k$  for a 101-bead Rouse chain, and that predicted by taking the continuous limit of a semi-infinite Rouse chain at times (a)  $\tilde{t} = 2.5$ , (b)  $\tilde{t} = 25$  and (c)  $\tilde{t} = 100$ .

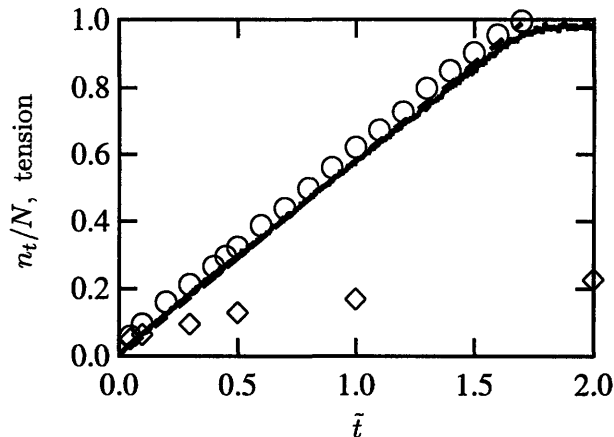


Figure 4.14: *Tension propagation in a 61-bead wormlike chain at a Peclet number of 100. The circles represent  $n_t/N$  as a function of  $\tilde{t}$  for a wormlike chain, and are found to superimpose on the rescaled tension in the first spring  $\tilde{F}_{\text{spr } 1, x}/(N_{k,s}\text{Pe})$ , scaled to reach a value of unity at steady state (shown by the solid line). Also shown for comparison are the corresponding  $n_t/N$  vs.  $\tilde{t}$  curve for a Rouse chain of identical length (diamonds) and that predicted by the convective model of tension propagation (dashed line).*

Figure 4.14 provides a comparison between the prediction of  $n_t$  obtained from the convective model and that obtained from simulation at a Peclet number of 100 for a 61-bead wormlike chain. The convective model predicts a slope of 34.9 for  $n_t$  as a function of  $\tilde{t}$  at  $\text{Pe} = 100$ , while a slope of 34.4 with 95% confidence limits of (34.0, 34.8) is obtained from a linear regression fit to 19 points from simulation. The agreement between the two is impressive, particularly given the assumption of equal spring extensions estimated from the large force limit of the Marko–Siggia law. The corresponding  $n_t$  versus  $\tilde{t}$  curve for a Rouse chain, shown for comparison, emphasizes the relatively rapid propagation of tension in a wormlike chain.

The transient behavior of the tension in the first spring of the wormlike chain is also illustrated in Figure 4.14. At a high Peclet number of 100, the tension at the tether point rises linearly from an initial value of zero to its steady value equal to the steady state drag on the chain, corresponding to  $\tilde{F}_{\text{spr } 1, x} = N_{k,s}\text{Pe}$ . Steady state is reached once tension propagates up to the free chain end, corresponding to a time of  $t \simeq Nl_s/v$ . The close accord between  $n_t/N$  and  $\tilde{F}_{\text{spr } 1, x}/(N_{k,s}\text{Pe})$ , where both quantities have been rescaled to attain a value of unity at steady state, reinforces our conclusion that the tension-bearing segment of a wormlike chain instantaneously acts like a shorter, tethered chain at steady state, and the drag it experiences is balanced by the tension at the tether point.

The prediction of the convective model is also tested under moderate conditions of  $\text{Pe} = 10$  and  $\text{Pe} = 30$ . The results are presented in Figure 4.15, again for a 61-bead chain. At early times, the evolution of  $n_t$  in a wormlike chain closely mimics the behavior of a Rouse chain, as expected for stretching in the linear regime. As tension propagates up to the free end of the chain, the springs near the free end, where the drag force is minimum, tend to be weakly stretched in comparison

with the springs close to the tether point. Therefore, at moderate flow strengths and at long times, the assumption of equal spring extensions in the portion of the chain under tension and the use of the large force limit of the Marko–Siggia law become increasingly likely to fail. (This feature is also apparent in Figure 4.6, providing a comparison between the spring extensions at  $Pe = 10$  and  $Pe = 100$ .) Consequently, deviations from the prediction of the convective model are again manifest as steady state is approached. There is, however, an intermediate region during which  $n_t$  grows linearly in time, and a comparison with the prediction of the convective model may be made in this region. At  $Pe = 10$ , the convective model predicts a slope of 4.18 for  $n_t$  versus  $\tilde{t}$ . A slope of 4.11 with 95% confidence limits of (3.91, 4.32) is obtained from a linear regression fit to the 10 points constituting the linear region obtained from simulation. At  $Pe = 30$ , the slope of 11.2 predicted by the convective model compares well to the value of 10.6 with 95% confidence limits of (10.4, 10.7) obtained via simulation from a linear regression fit to 11 points.

The time point at which the crossover occurs from Rouse to convective behavior may be estimated by imposing the equality of the slope  $dn_t/d\tilde{t}$  for a semi-infinite Rouse chain, derived from Equation 4.17, and that predicted by the convective model, obtained from Equation 4.18. We thereby obtain the expression

$$\tilde{t}_c = \frac{\tilde{H}}{\pi} \left[ \frac{1 - (2Pe)^{-1/2}}{N_{k,s}Pe/N} \right]^2 \quad (4.19)$$

for the nondimensional crossover time  $\tilde{t}_c$ . A crossover time of  $\tilde{t}_c = 1.1$  is predicted by Equation 4.19 at a Peclet number of 10, which is close to the value  $\tilde{t}_c = 1.0$  obtained from the simulation data of Figure 4.15(a). At a Peclet number of 30, the predictions of Equation 4.19 and the simulation data of Figure 4.15(b) are, respectively,  $\tilde{t}_c = 0.15$  and  $\tilde{t}_c = 0.24$ . At a Peclet number of 100, Equation 4.19 yields  $\tilde{t}_c = 0.015$ . However, the prediction of  $\tilde{t}_c$  from the simulation data of Figure 4.14 is hindered by the nonavailability of data points very close to  $\tilde{t} = 0$ , owing to the discretization error.

Figure 4.15 reveals that the rescaled tension in the first spring,  $\tilde{F}_{\text{spr } 1, x}/(N_{k,s}Pe)$ , scaled to reach unity at steady state, closely mirrors the evolution of  $n_t/N$  with time at Peclet numbers of 10 and 30. This is consistent with the existence of a similar trend at  $Pe = 100$ . However, such a correspondence between  $n_t$  and the tension in the first spring is not observed in a Rouse chain, where the rescaled tension in the first spring falls significantly below the  $n_t/N$  versus  $\tilde{t}$  curve at intermediate time points before steady state is reached. These observations suggest that the tension-bearing segment of a wormlike chain, but not of a Rouse chain, behaves instantaneously like a shorter, tethered chain of identical length at steady state.

## 4.6 Discussion

The present investigation provides an analysis of transient chain stretching in a uniform flow field for a free draining polymer chain modeled as a Rouse chain or as a wormlike chain. The Rouse model is found to provide a satisfactory approximation of a finitely extensible DNA chain at Peclet numbers of the order of 1 or smaller, under which conditions the chain has not been significantly perturbed from the linear, near-equilibrium stretching regime. The dynamic scaling behavior of the Rouse model is readily inferred from the analytical solution of the set of linear Langevin equations governing Rouse dynamics.

As the Peclet number is increased, finite extensibility is found to play a dominant role in determining chain dynamics and in controlling the propagation of tension in the chain. For wormlike

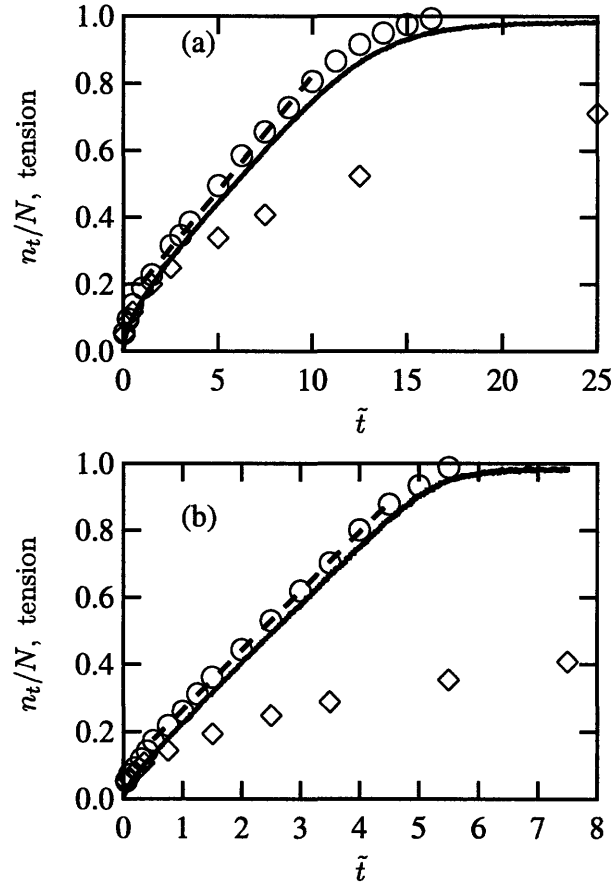


Figure 4.15: *Tension propagation in a 61-bead wormlike chain at Peclet numbers of (a) 10 and (b) 30. The circles represent  $n_t/N$  vs.  $\tilde{t}$  for a wormlike chain. Each dashed line represents the best-fit line passing through the linear region of the corresponding curve for a wormlike chain. Also shown for comparison are the results for a Rouse chain under identical conditions (diamonds). Each solid line is the tension in the first spring rescaled to reach a value of unity at steady state, given by  $\tilde{F}_{\text{spr } 1, x}/(N_{k,s}\text{Pe})$ .*

chains, as for Rouse chains, the transient fractional extension and spring tensions are found to be universal functions of  $t/N^2$  for different chain lengths  $N$  at a fixed value of the Peclet number. The wormlike chain model, unlike the Rouse model, exhibits a nonlinear dependence on the Peclet number, with the chain extension being determined by the cooperative stretching of strongly stretched springs governed by the nonlinear Marko–Siggia force law.

Our results for the time evolution of the chain length under tension indicate a diffusive propagation of tension in Rouse chains. For a wormlike chain, a comparison with the predictions of the convective model of tension propagation is effected by assuming that the springs in the tension-bearing section of the chain have identical extensions, derived from the large force limit of the Marko–Siggia force law. Our results for the tension propagation in a wormlike chain at high Peclet numbers of the order of 100 corroborate the convective model proposed by Randall and Doyle [41]. At a moderate Peclet number of the order of 10, our results suggest a transition from Rouse behavior at early times to convective tension propagation at later times, and an estimate of the time at which the transition occurs is provided. At still longer times, deviations from convective behavior are observed, possibly because the weak stretching of the springs near the free chain end induces errors in our estimate of the spring lengths. Furthermore, the linearity of the tension profiles and the close agreement between the tension in the first spring and the number of springs under tension at any given point in time suggest that the portion of a wormlike chain under tension acts instantaneously like a steady chain of length identical to that of the tension-bearing section.

A comparison may be made with the scaling arguments of Brochard-Wyart and her coworkers [89,92], derived for nondraining blobs in a good solvent. Our results for the short time behavior of the chain extension agree with the convective behavior predicted by those authors. This, however, has been interpreted by us as arising from the affine movement of the free chain end, especially at high Peclet numbers. The long time behavior of chain extension is predicted by Brochard-Wyart et al. from the trumpet picture [92] to be an exponential relaxation to steady state with a time constant that is inversely proportional to the flow velocity. In the stem-and-flower regime, Brochard-Wyart’s arguments for the long time limit of chain stretching [89] imply an exponential relaxation of the chain extension to its steady value with a time constant that is inversely proportional to the square of the flow velocity. These predictions are not reproduced in our results. The linearity of the Rouse model imposes a decoupling of the relaxation times from the solvent velocity. The wormlike chain model predicts a nonlinear dependence of the chain extension on the Peclet number different from that predicted by Brochard-Wyart and her coworkers, resulting from the simultaneous stretching of strongly extended wormlike springs. Furthermore, the results of these researchers predict a steady fractional extension proportional to  $1 - f^{-1}$ , in accord with the behavior of a freely jointed chain acted upon by a drag force of  $f$  [51]. The steady fractional extension of a strongly stretched wormlike chain is, on the other hand, proportional to  $1 - f^{-1/2}$  [52]. A reformulation of the blob model in a theta solvent under free draining conditions leads to results in accord with the predictions of the Rouse model.

As previously stated in Section 4.1, hydrodynamic interactions have been neglected in the present work. Experimental studies of DNA dynamics are typically carried out in microchannels whose heights are far exceeded by the chain contour lengths. For example, the experiments of Ref. [41] employing  $\lambda$ -DNA and T4-DNA having contour lengths of 21  $\mu\text{m}$  and 70  $\mu\text{m}$ , respectively, were conducted in a microchannel of height 2  $\mu\text{m}$ . Hydrodynamic interactions among chain segments are screened under such conditions, thus partially justifying the free draining assumption.

Our results elucidate the mechanism of transient chain unraveling in uniform flow, relevant to

disentanglement processes occurring in post arrays subsequent to a DNA chain–obstacle collision [29,30], in dilute solution capillary electrophoresis [25–28], and in flows of polymer solutions [70].



# *Stochastic Modeling and Simulation of DNA Electrophoretic Separation in a Microfluidic Obstacle Array*

---

## **5.1 Introduction**

The use of microfluidic post arrays for the size-based separation of electric field driven DNA chains of different lengths, actuated by their size-dependent collisions with the posts, has been experimentally established [29, 30]. The chain dynamics in the obstacle array may be decomposed into three sequential, cyclically repeating steps [34, 35], namely, the collision of the chain with an obstacle and the unraveling of the two arms on either side of the obstacle, the unhooking of the chain, and the unhindered motion of the chain until its next collision with an obstacle. This process has been modeled by Minc et al. [34] as a nonseparable continuous-time random walk (CTRW) on a lattice [71, 100]. The model of Minc et al. involves a random waiting time subsequent to a collision encompassing both the duration of the collision, as well as the transit time at the free solution electrophoretic velocity between successive collisions. The DNA chain was thus modeled as a “leaper” [71], and was assumed to transition instantaneously from one lattice site to the next.

Minc et al., following the analysis of Popelka et al. [101], assumed the unraveling time for each arm of the chain to be proportional to the fraction of the chain represented by that arm. However,

as explained in Chapter 4 and Ref. [102], upon modeling the post as a tether point during the unraveling process, the unraveling of the arms under conditions of strong field strengths occurs via a convective mechanism, whereby the transient arm length grows linearly in time at a rate equal to the free solution electrophoretic velocity and independent of its length. The analysis of Minc et al., therefore, overestimates the unraveling time, and, hence, the duration of the collision. Another drawback of the analysis is that the collision probability at each obstacle was set equal to the areal post density, irrespective of the size of the chain. Moreover, Minc et al. equated the chain extension at the end of the unraveling process to the contour length of the chain, thereby neglecting its field-dependence. Consequently, their model failed to predict the experimentally observed field-dependence of the separation resolution [31].

Recently, an attempt was made to take into account the incomplete extension of the chain during collisions at finite field strengths by Dorfman [35]. This study modeled the unraveling process as being equivalent to the unraveling of a tethered polymer chain in a uniform solvent flow field at a solvent velocity equal to the free solution electrophoretic velocity. With this assumption, use may be made of the results of Brochard-Wyart [89] relating the steady state extension of a tethered chain to the solvent velocity, upon replacing the solvent velocity with the relative velocity of the solvent with respect to the extending chain arm, and solving for the rate of chain growth as a function of the instantaneous chain length, under the assumption of quasisteady stretching. However, the study of Ref. [35] instead equated the relationship between the steady state chain extension and the free solution electrophoretic velocity to that between the transient chain extension and its rate of growth, thereby rendering the analysis invalid.

The development of a more accurate model of chain dynamics in an obstacle array requires knowledge of chain-obstacle interactions during and subsequent to a collision. Several studies have focused on the mechanism of collision of a chain with a single, stationary obstacle. Nixon and Slater [103] have provided a rope-over-pulley model of chain unhooking, assuming Gaussian and uniform distributions of the initial difference in arm lengths on either side of the obstacle following a collision. These authors have found that the mean and variance of the unhooking time exhibit the same scaling dependence on the chain length regardless of the initial distribution of arm lengths. A strong dependence of the collision probability and the duration of a collision on the impact parameter has been demonstrated in Refs. [36] and [37]. More complicated configurations involving the hooking of a single chain around two or more obstacles have been theoretically studied in Ref. [38].

More recently, as described in a series of papers, Randall and Doyle [39–41] have provided detailed experimental investigations of polymer-obstacle collisions in PDMS microchannels enclosing an obstacle or a dilute array of obstacles, and have proposed physical mechanisms for the dynamics of chain unraveling and unhooking subsequent to a collision. These authors have classified polymer-obstacle collisions into J- or U-collisions (according as the initial lengths of the two arms of the chain are unequal or equal) involving the sequential unraveling and ropelike unhooking of the two arms of the chain, X-collisions, wherein the long arm of the chain continues to unravel as the chain is unhooking from the post, and rare, metastable W-collisions, resulting from the formation of entangled chain configurations [41]. Different models were proposed for the unhooking time and the holdup time during which center of mass motion is obstructed by the obstacle following X- and J-collisions, inspired by the distinct mechanisms operative in the two cases. X-collisions were found to occur predominantly under conditions of strong electric fields, or, equivalently, at high Peclet numbers. These findings were corroborated by the simulation study of Kim and Doyle [42], based on

Brownian dynamics simulations of collisions of  $\lambda$ -,  $2\lambda$ - and T4-DNA with a single post. The latter study revealed that a crossover from the predominance of X-collisions to J-collisions occurs at an initial short arm fraction of approximately 0.4, with X-collisions being predominant at initial short arm fractions below this value. Kim and Doyle further provided comparisons of the unhooking time and center of mass holdup time as predicted by the collision models of Ref. [41] with simulation data. In accord with the experimental observations of Ref. [41], it was discovered that the ropelike unhooking time of a chain at constant extension provides an excellent approximation of the center of mass holdup time during a polymer–obstacle collision for the entire range of field strengths and chain lengths studied for both X- and J-collisions. Although the holdup times for W-collisions observed in simulations differed from the predicted holdup times of the X- and J-models, as well as from the ropelike unhooking time, such collisions are rare and may be neglected. Furthermore, Kim and Doyle also observed the probability distribution of the initial short arm fraction to be increasingly well-approximated by a uniform distribution as the field strength is increased.

In the present study, we make use of the insight gained into chain–obstacle collisions from the aforementioned studies to develop a more accurate CTRW model of chain dynamics in the array. The center of mass holdup time following each collision is well-approximated by the ropelike unhooking time, as described in the preceding paragraph. We employ the low-force and large-force limits of the Marko–Siggia interpolation formula for the wormlike chain [52], which best describes DNA elasticity, to derive the dependence of chain extension on the field strength [42]. Furthermore, we account for the dependence of the collision probability at each obstacle on the chain size, and generalize the model of Minc et al. [34, 35] to allow for finite transit times between successive collisions. Concomitantly, we perform Brownian dynamics simulations of DNA chains of three sizes, namely,  $\lambda$ -DNA and the two shorter chains  $\lambda/3$ -DNA and  $2\lambda/3$ -DNA resulting from its digestion with the restriction enzyme Xho I [30], in microfluidic post arrays formed from the self-assembly of magnetic beads [72, 73]. We analyze the shortcomings of the model in light of the results for chain mobility, dispersivity, collision probability, mean distance covered between successive collisions, and the separation resolution obtained from simulation.

## 5.2 CTRW Model of Chain Dynamics

In this Section, we present the revised CTRW model of DNA motion in the obstacle array. The chain is modeled as a random walker commencing from position  $r = 0$  and moving in the field direction at the free solution electrophoretic velocity  $\mu_0 E$  between successive collisions, with  $\mu_0$  the free solution electrophoretic mobility and  $E$  the magnitude of the electric field strength. When a collision occurs at an obstacle, representing a “turning point”, the chain waits at the location of the obstacle during the unraveling and unhooking processes before continuing at the free solution electrophoretic velocity until the next collision. The turning points can occur only at the location of the obstacles,  $r = na$ , where  $a$  denotes the lattice constant and  $n$  is an integer.

Let  $p(r, t)$  denote the probability density function of the random variable  $R(t)$  representing the position of the walker at time  $t$ , and let  $R_1$  and  $T_1$  denote, respectively, the random variables representing the distance between consecutive collisions and the time taken to execute the transition from the start of one chain–obstacle collision to the next. Then  $p(r, t)$  is governed by the evolution

equation [71]

$$p(r, t) = \int dr' \int_t^\infty d\tau q(r, t|r', \tau) \chi(r', \tau) + \int dr' \int_0^t d\tau p(r - r', t - \tau) \chi(r', \tau) \quad (5.1)$$

In the above,  $\chi(r', \tau)$  represents the joint probability density function of  $R_1$  and  $T_1$ . The term  $q(r, t|r', \tau)$ , with  $t < \tau$ , denotes the conditional probability density function for the position of the chain at time  $t$  before the first turning point from the origin is reached, given that the turning point lies at  $r'$ , and is reached at time  $\tau$ . For the DNA chain,

$$q(r, t|r', \tau) = \begin{cases} \delta(r) & \text{for } 0 \leq t \leq \tau_H \\ \delta(r - \mu_0 E t) & \text{for } \tau_H < t < \tau \end{cases} \quad (5.2)$$

where  $\tau_H$  is the holdup time [41] during which the center of mass motion is obstructed by the obstacle.

We approximate the holdup time with the expression

$$\tau_H = -\frac{\mathcal{L}}{2\mu_0 E} \ln(1 - 2r_0) \quad (5.3)$$

representing the ropelike unhooking time of a chain at constant extension, with  $r_0$  the initial fraction of the chain contained in the short arm and  $\mathcal{L}$  the total chain extension at the start of the unhooking process. Equation 5.3 has been found to provide an excellent approximation to the holdup time for a wide range of chain lengths and field strengths [42]. The short arm fraction at the start of each collision,  $r_0 = x_1(0)/\mathcal{L}$ , with  $x_1(0)$  the short arm length at the start of the unhooking process, is assumed to be uniformly distributed in the interval  $[0, 0.5]$ . The assumption of uniformly distributed initial short arm fraction has been found to hold at high field strengths [42]. The use of other distributions at low field strengths, such as the Gaussian distribution, may have a quantitative effect on the results [103].

The transition probability density function may be written as

$$\chi(r, \tau) = g(\tau|r)h(r) \quad (5.4)$$

where the term  $g(\tau|r)$  denotes the conditional probability density of the transition time  $T_1$ , given that the next collision occurs a distance  $r$  away, with the transition time being the sum of the holdup time  $\tau_H$  and the transit time until the next collision occurring a distance  $r = na$  away, i.e.,

$$T_1 = \tau_H + \frac{na}{\mu_0 E} \quad (5.5)$$

It follows from Equations 5.3 and 5.5, in conjunction with the assumption that  $r_0$  is uniform in  $[0, 0.5]$ , that

$$g(\tau|r = na) = \frac{2\mu_0 E}{\mathcal{L}} \exp\left[-\frac{2\mu_0 E}{\mathcal{L}} \left(\tau - \frac{na}{\mu_0 E}\right)\right] \quad (5.6)$$

with  $\tau \in [na/(\mu_0 E), \infty]$ , where  $n$  is an integer. Following Minc et al. [34], we assume that no collisions occur along the extended backbone of the chain and set the probability  $h(r)$  that successive

collisions are separated by a distance  $R_1 = r$  to be

$$h(r) = \begin{cases} \rho(1-\rho)^{n-n^*} & \text{for } r = na, \ n \geq n^* \\ 0 & \text{otherwise} \end{cases} \quad (5.7)$$

where  $\rho$  is the collision probability at any obstacle and  $n^*$  is the first lattice position at which the next collision can occur, given by the expression [34]

$$n^* = \frac{\mathcal{L}}{a} \quad (5.8)$$

The discreteness of the lattice necessitates that  $n^*$  be at least 1, a condition that we enforce in all our calculations. Note that the mean distance covered between successive collisions obtained from Equation 5.7 is

$$a \langle n \rangle = a \left( \frac{1-\rho}{\rho} + n^* \right) \quad (5.9)$$

Equations 5.4, 5.6 and 5.7 combine to yield

$$\chi(r, \tau) = \frac{2\mu_0 E}{\mathcal{L}} \exp \left[ -\frac{2\mu_0 E}{\mathcal{L}} \left( \tau - \frac{r}{\mu_0 E} \right) \right] \rho(1-\rho)^{r/a-n^*} \sum_{n \geq n^*} \delta(r - na) \quad (5.10)$$

where the last term on the right hand side enforces the condition that the turning point location be an integral multiple of  $a$ .

The long time asymptotic behavior of  $p(r, t)$  is governed by the asymptotic behavior of its Fourier-Laplace transform, denoted  $p^*(k, u)$ , in the limit  $u \rightarrow 0$  [71]. The long time asymptotic mean velocity  $U$  and dispersivity  $D$  are related as usual for diffusion processes to the mean and variance of the random walker's position  $R(t)$  in the long time limit of  $t \rightarrow \infty$ , or  $u \rightarrow 0$  (i.e.,  $\langle R(t) \rangle = Ut$  and  $\langle R(t)^2 \rangle - \langle R(t) \rangle^2 = 2Dt$  in the long time limit). We proceed by computing the Fourier-Laplace transform  $p^*(k, u)$  from Equation 5.1, with use of Equations 5.2 and 5.10, and expanding the result in powers of  $k$ . The first two moments of the walk derive from the coefficients of the first and second powers of  $k$ , respectively. These moments, in turn, are related to the long time asymptotic mean velocity  $U$  and dispersivity  $D$  in the limit  $u \rightarrow 0$ . We then obtain the results

$$\frac{\mu}{\mu_0} = \frac{2(1-\rho + \rho n^*)}{3\rho n^* + 2(1-\rho)} \quad (5.11)$$

and

$$\frac{D}{\mu_0 E a} = \frac{n^{*2} \rho \left[ 2 + \rho(2n^* - 3) + \rho^2 (n^* - 1)^2 \right]}{[3\rho n^* + 2(1-\rho)]^3} \quad (5.12)$$

where we have introduced the mobility  $\mu$  via the relation  $U = \mu E$ .

The analysis of Minc et al. [34] corresponds to the situation  $q(r, t|r', \tau) = \delta(r)$ , under the assumption that the DNA molecule behaves as a leaper, instantaneously transitioning from one turning point to the next. In general, depending on the form of  $\chi(r, \tau)$ , use of Equation 5.2 rather than the leaper model may quantitatively impact the results [71]. With the form of  $\chi(r, \tau)$  chosen here, the results are unchanged upon using the leaper model.

The collision probability  $\rho$  and the field-dependence of the chain extension  $\mathcal{L}$  at the start of unhooking remain to be specified. We postulate that  $\rho$  may be approximated by the expression

$$\rho = \frac{R_g}{a} \quad (5.13)$$

where  $R_g$  is the radius of gyration of the chain. Equation 5.13 attempts to account for the dependence of the collision probability on the chain size and is expected to be best-suited to situations wherein the post diameter is small compared to the coil size, which in turn is small compared to the lattice constant, under the assumption that the chain instantaneously relaxes to its equilibrium coil shape following a collision. We, however, make use of Equation 5.13 even in situations wherein the chain radius of gyration is comparable to the post radius.

The chain extension will be derived from the low- and large-force limit of the Marko–Siggia formula [cf. Equation 1.10] in the regime of weak and strong stretching, respectively. The former, Gaussian regime derives from the Marko–Siggia rule in the limit  $\mathcal{L}/L \ll 1$ , while the latter corresponds to the limit  $\mathcal{L}/L \lesssim 1$ , where  $L$  denotes the contour length of the chain. The crossover from weak stretching to strong stretching occurs at  $\text{Pe}_{\text{chain}} \sim 1$  [102], where we have introduced the Peclet number

$$\text{Pe}_{\text{chain}} = \frac{\mu_0 E \zeta_{\text{chain}} A}{k_B T} \quad (5.14)$$

Note that the definition of the Peclet number here is based on the persistence length  $A$  rather than on the Kuhn length  $b_k$  as was done in Chapter 4. However, the two definitions differ only by a factor of 2, and conclusions based on order of magnitude analyses are unaffected. In Equation 5.14,  $\zeta_{\text{chain}}$  refers to the drag coefficient for the chain. Note that Equation 5.14 represents the nondimensional drag force acting on the chain, whereby the value  $\text{Pe}_{\text{chain}} \sim 1$  delineates the regimes of weak and strong chain stretching, as also seen in Chapter 4 and Ref. [102]. The Marko–Siggia interpolation rule then yields

$$\mathcal{L} = \begin{cases} \frac{L}{6} \text{Pe}_{\text{chain}}, & \text{Pe}_{\text{chain}} \leq 1 \\ L \left( 1 - \text{Pe}_{\text{chain}}^{-1/2} \right), & \text{Pe}_{\text{chain}} > 1 \end{cases} \quad (5.15)$$

where an effective force equivalent to one-fourth of the drag force  $\mu_0 E \zeta_{\text{chain}}$  has been employed to account for the nonuniformity in drag along the chain [42, 52]. As intimated by Equation 5.15, the dependence of the chain extension on the Peclet number is deduced from the Marko–Siggia interpolation formula under the assumption that a sharp transition from weak to strong stretching occurs at  $\text{Pe}_{\text{chain}} = 1$ , although no such sharp transition occurs in reality. We have verified that the results are hardly affected upon instead assuming the transition to occur at  $\text{Pe}_{\text{chain}} = 2$ , corresponding to roughly 30% chain extension.

Equations 5.11 and 5.12 may now be substituted in the expression [34]

$$R_s = \frac{|U_1 - U_2|}{U_1 + U_2} \sqrt{\frac{L_s}{16} \left( \frac{U_1}{D_1} + \frac{U_2}{D_2} \right)} \quad (5.16)$$

for the separation resolution  $R_s$ , where the subscripts 1 and 2 refer to the two species to be separated, and  $L_s$  is the separation length.

## 5.3 Brownian Dynamics Simulations

### 5.3.1 Chain Simulations

We adopt the technique of Brownian dynamics applied to the bead–spring model of the chain to simulate its behavior in a post array. Chain dynamics in an electric field are described by the Langevin equation [cf. Equation 1.23]

$$d\mathbf{r}_j = \left[ \mu_0 \mathbf{E} + \frac{1}{\zeta} (\mathbf{F}_j^s + \mathbf{F}_j^{\text{ev}}) \right] dt + \sqrt{\frac{2k_B T}{\zeta}} d\mathbf{W}_j, \quad j = 1, \dots, N \quad (5.17)$$

applied to each bead  $j = 1, \dots, N$  of the chain, where  $\mathbf{r}_j$  denotes the position vector of bead  $j$  relative to the origin, while  $\mathbf{F}_j^s$  and  $\mathbf{F}_j^{\text{ev}}$  refer, respectively, to the spring force and the net excluded volume force acting on bead  $j$ . The distortion of the electric field  $\mathbf{E}$  caused by the presence of finite-size, nonconducting posts is neglected. The force exerted on the negatively charged DNA chain by the electric field is accounted for via the inclusion of the term  $\mu_0 \mathbf{E}$  in Equation 5.17 [43]. Contrary to convention, we assign the direction of  $\mathbf{E}$  to that of the electric force experienced by a negative test charge, so that  $\mu_0$  is positive. Free draining conditions are assumed, whereby  $\zeta_{\text{chain}} = N\zeta$ , with  $\zeta$  the Stokes drag coefficient for each bead. The terms  $\mathbf{W}_j$  represent independent vector Wiener processes, as described in Section 1.2 and Chapter 4. The  $x$ -coordinate is measured along the direction of the electric field  $\mathbf{E}$ .

We consider DNA molecules of three lengths, namely,  $\lambda$ -DNA (having 48 502 base pairs with a contour length of 20.5  $\mu\text{m}$  when stained with YOYO dye in the ratio of 4 base pairs of DNA per molecule of dye), and the two fragments  $2\lambda/3$ -DNA (containing 33 497 base pairs) and  $\lambda/3$ -DNA obtained from the digestion of  $\lambda$ -DNA with the restriction enzyme Xho I [30]. We adopt the discretization used by Kim and Doyle to model  $\lambda$ -DNA [42], and select  $N_{k,s} = 5.23b_k$ , with  $b_k = 0.106 \mu\text{m}$ . At this discretization, used in conjunction with a sufficiently small time step as described later in this Section, we are assured that aphysical configurations, wherein the chain appears to intersect an obstacle, are forbidden from arising. We, therefore, select  $N = 38$  beads to model  $\lambda$ -DNA, whereas  $2\lambda/3$ -DNA and  $\lambda/3$ -DNA are modeled by  $N = 27$  and  $N = 12$  beads, respectively. The corresponding chain lengths of  $2\lambda/3$ -DNA and  $\lambda/3$ -DNA, 14.4  $\mu\text{m}$  and 6.1  $\mu\text{m}$ , respectively, differ slightly from the values 14.2  $\mu\text{m}$  and 6.3  $\mu\text{m}$ , respectively, estimated by assuming a linear dependence of the contour length on the number of base pairs.

We perform simulations at a number of experimentally accessible field strengths expressed in terms of a Peclet number as defined by Equation 5.14 where  $\zeta_{\text{chain}} = N\zeta$ , with  $\text{Pe}_\lambda$ , based on the value  $N = 38$  selected for  $\lambda$ -DNA, varying from 0.1 to 50. The corresponding values of  $\text{Pe}_{\text{chain}}$  for  $2\lambda/3$ -DNA and  $\lambda/3$ -DNA are obtained by means of the equality  $\text{Pe}_{\text{chain}} = \text{Pe}_\lambda N_{\text{chain}}/38$ , where  $N_{\text{chain}}$  is the number of beads modeling the chain of interest. This range of values corresponds to electric field strengths ranging from 0.5 to 100 V/cm, estimated from Equation 5.14 for a  $\lambda$ -DNA molecule having a radius of gyration of 0.69  $\mu\text{m}$  and a thickness of 2 nm [47] at  $T = 298$  K in a solvent of viscosity 1 cP by making use of the Zimm drag coefficient for a coil [24, 50] at  $\text{Pe}_\lambda = 0.1$  and the drag coefficient for a rod [63] at  $\text{Pe}_\lambda = 50$ , and using the experimentally measured value of  $\mu_0$  [31]. In addition, for  $\lambda$ -DNA, we also provide data for chain dispersivity at  $\text{Pe}_\lambda = 0.01$  and 0.05.

We employ the modified Marko–Siggia law, given by Equation 1.11, to describe the force–extension behavior of the springs. Following Kim and Doyle [42], we adopt the low-force criterion

of Underhill and Doyle [55], and employ the ratio  $\lambda = 1.91$  of the effective persistence length to the true persistence length.

Following Kim and Doyle [42], we employ the soft, repulsive intrachain excluded volume force developed by Jendreck et al. [60], given by Equation 1.21. We employ the value  $v = 0.0004 \mu\text{m}^3$  for the excluded volume parameter, determined by Kim and Doyle to accurately reproduce the radius of gyration of  $\lambda$ -DNA with the present discretization. With the above parameters, the equilibrium radii of gyration obtained from simulations of  $2\lambda/3$ -DNA and  $\lambda/3$ -DNA in free solution are  $0.59 \mu\text{m}$  and  $0.37 \mu\text{m}$ , respectively, which are close to the values  $0.56 \mu\text{m}$  and  $0.34 \mu\text{m}$  obtained from the good solvent scaling law  $R_g \sim L^{0.589}$  [50].

We consider channel heights large compared to the size of the chain [31], and ignore interactions between the beads and the channel walls. As a result, the dynamic behavior of interest to us is confined to the two dimensions spanning the channel plane. The interactions between the chain and the obstacles in the array are modeled by hard-sphere exclusion implemented via the Heyes–Melrose algorithm [104], whereby an overlap between a bead and an obstacle resulting from the integration of Equation 5.17 at any time point is subsequently corrected by displacing the bead along the line of centers of the bead and the obstacle away from the obstacle center, until the bead and the obstacle are just touching. The beads are modeled as having no hard-sphere volume [42]. Since hard-sphere exclusion is implemented independent of time stepping, the possibility exists that a spring may be overstretched as a result of its implementation. This problem is alleviated by using sufficiently small time steps. Simultaneously, the time step must also be small compared to the relaxation time of a single spring. At a Peclet number below 0.1 for each chain, a time step of  $0.01\zeta Q_0^2/(k_B T)$  was found to suffice, with the time step at stronger field strengths chosen to be inversely proportional to the Peclet number. Under these conditions, overstretching is largely eliminated. In the extremely rare instances when overstretching occurred (in fewer than a millionth of the total number of time steps for a typical trajectory), the spring force was calculated by linearly extrapolating the modified Marko–Siggia force law [cf. Equation 1.11] from the value of the force at 99% spring extension.

We adopt the semi-implicit predictor–corrector scheme described in Ref. [63] for the integration of Equation 5.17. Averages are performed over an ensemble of between 100 and 1 000 chains. The array geometries employed are described in Section 5.3.2. Initial equilibrium configurations are generated by employing the Marko–Siggia force law to simulate the evolution to equilibrium of initially Gaussian coils [102]. These coil configurations are placed upstream of the array at the start of the simulation, and simulated in the array until the chain stretch equilibrates, reaching a steady value. A time duration corresponding to the time taken to cross a distance of 50 to 100 lattice spacings at the free solution electrophoretic velocity is found sufficient to ensure equilibration. Subsequently, the equilibrated chain is simulated further in the array for the same time duration.

The long time mean velocity and dispersivity are obtained from the mean and variance of the distribution of the center of mass  $x$ -coordinates (denoted  $x_{\text{cm}}$ ) for an ensemble of chains at the end of the simulation, measured relative to their values at the end of the equilibration process, by fitting to a normal distribution and using the relations  $\langle x_{\text{cm}} \rangle = Ut$  and  $\text{var}(x_{\text{cm}}) = 2Dt$ , where  $t$  is the time duration of the simulation following the equilibration process. In all cases, the assumption of normality is confirmed by performing the Kolmogorov–Smirnov test [105]. Additionally, we define a collision to have occurred when a portion of the chain is present in all four quadrants of a coordinate plane whose origin lies at the obstacle center [41, 42], and enforce the conditions that a collision with a given obstacle occur only once per trajectory, and (although the situation did not arise in our simulations) that a collision at a given time step with multiple obstacles be counted as a single

collision. We deduce the mean probability of collision at each obstacle from simulation by dividing the number of collision events occurring in a trajectory by the number of lattice spacings covered by the chain center of mass in that trajectory following equilibration, averaged over the ensemble. We also measure the mean distance covered by the chain center of mass between successive collisions in each trajectory after equilibration, averaged over the ensemble, while excluding trajectories in which fewer than 2 collisions occur in performing the ensemble-average.

### 5.3.2 Selection of Array Geometries

We chose a hexagonal geometry as being representative of the lattice pattern resulting from the self-assembly of magnetic colloids [72,73], and conducted an initial set of simulations of  $\lambda$ -DNA in a planar, semi-infinite hexagonal array occupying the right-half plane  $x \geq 0$ , composed of obstacles of diameter  $d = 1 \mu\text{m}$  at a lattice constant of  $a = 3 \mu\text{m}$ . The array orientation was such that the separation between adjacent lattice points along the  $x$ -axis was equal to the lattice constant. Hard-sphere exclusion between the chain and the obstacles was enforced by exploiting the regularity of the lattice to identify the obstacles in the vicinity of each bead of the chain at every time step. Figure 5.1 illustrates the results of these simulations. It is clear from Figure 5.1 that the obstacles in a regular, dilute lattice provide straight channels through which the chain can pass without hindrance, and the mobility and normalized dispersivity of the chain rapidly asymptote to  $\mu_0$  and 0, respectively, as the Peclet number is increased. This observation is consistent with the finding of Patel and Shaqfeh [53] that disordered post arrangements are essential for separation.

We were motivated by the above finding to employ an array more representative of a magnetic colloid assembly, generated via free draining Brownian dynamics simulations of a collection of hard spheres, each of diameter  $d = 1 \mu\text{m}$ , with repulsive point dipoles at their centers in two dimensions, with a magnetic field applied normal to the plane and with the neglect of mutual induction between the colloids <sup>1</sup> [72,73]. The magnetic particles are confined to the portion of the  $x$ - $y$  plane bounded by  $x = 0$ ,  $x = X$ ,  $y = 0$  and  $y = Y$  by means of periodic boundary conditions.  $X$  and  $Y$ , denoting the length and width of the periodically repeating unit constituting the semi-infinite, planar array occupying the region  $x \geq 0$ , are chosen to be  $600.1 \mu\text{m}$  and  $129.9 \mu\text{m}$ , respectively. The initial condition corresponds to a perfect hexagonal lattice, with four times as many particles placed along the  $x$ -axis as along the  $y$ -axis. This condition, in conjunction with the ratio  $Y/X = \sqrt{3}/8$  of the unit cell dimensions, was chosen to yield an array orientation such that the separation between adjacent lattice points along the  $x$ -axis was equal to the lattice constant.

The dimensionless interaction energy scale for the magnetic colloid system is defined as [72,73]

$$\Gamma = \frac{\Lambda}{2} \left( \frac{d}{R} \right)^3 \quad (5.18)$$

where  $R = a \sin(\pi/3)$ ,  $a$  denotes the lattice spacing, and  $\Lambda$  is the ratio of the interaction potential between two dipoles oriented parallel to each other and separated by a distance  $d$ , to the thermal energy [72,73]. All two-dimensional systems at the same value of  $\Gamma$  behave identically if  $R$  is the only relevant length scale in the system, provided that the system size is large enough that finite size effects are negligible [72,73]. We chose the value  $\Gamma = 12$ , at which the lattice possesses neither

---

<sup>1</sup>We are grateful to Dr. Ramin Haghgoie of Massachusetts General Hospital and MIT for providing the code for the generation of the arrays used in this thesis.

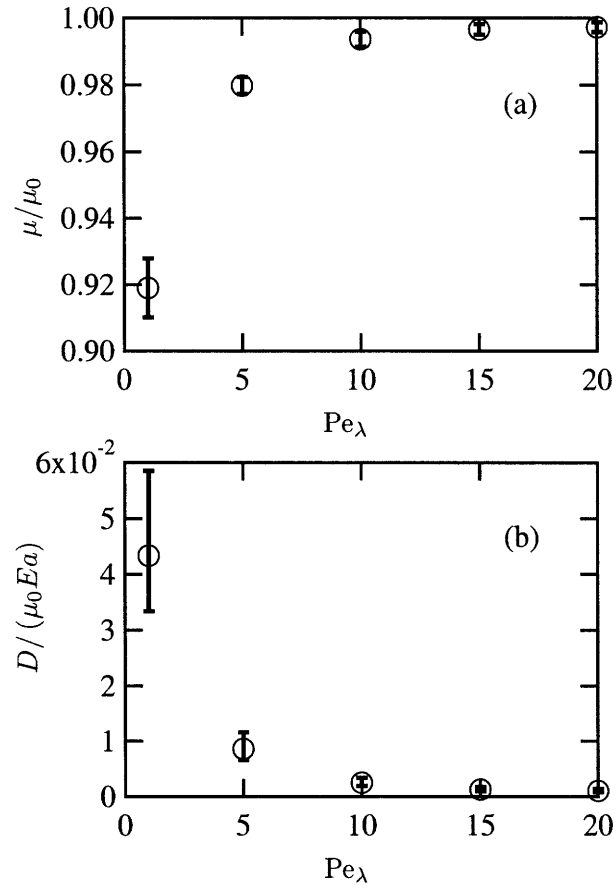


Figure 5.1: Normalized mobility (a) and dispersivity (b) of  $\lambda$ -DNA as a function of  $Pe_\lambda$  calculated from simulation in a regular, hexagonal array having a lattice constant of  $3 \mu\text{m}$ .

translational nor long-range orientational order, and, hence, lies in the liquid phase. The value of  $\Gamma$  was held constant at 12, and the number of colloids  $N_c$  in the unit cell and  $\Lambda$  were varied in order to vary the lattice spacing while holding fixed the remaining lattice characteristics, by means of the relation  $a = [\sqrt{3}N_c/(2XY)]^{-1/2}$  [72, 73]. In all simulations, pairwise dipole-dipole interactions were considered only between pairs of particles separated by a distance less than a cutoff of  $7R$ . The simulations were run until the defect concentration reached steady state [73], at a time step of approximately  $10^{-3}\zeta'd^2/(k_B T)$ , where  $\zeta'$  is the drag coefficient for each magnetic colloid. Following the attainment of steady state, the positions of the magnetic colloids were held constant, and were not allowed to evolve further once the chain was introduced in the array. The reader is referred to Refs. [72] and [73] for further details on the simulation methods adopted for magnetic colloid systems and their characteristics.

We employ assemblies of  $N_c = 40\,000$ ,  $10\,000$ ,  $4\,900$ ,  $2\,500$ ,  $1\,600$  and  $900$  colloidal particles, yielding mean lattice spacings averaged over nearest-neighbor pairs [72, 73] of  $1.53$ ,  $3.06$ ,  $4.37$ ,  $6.12$ ,  $7.65$  and  $10.21\ \mu\text{m}$ , respectively. The corresponding defect concentrations (where a defect is defined as a particle with greater or fewer than six nearest neighbors) are  $0.306$ ,  $0.301$ ,  $0.292$ ,  $0.307$ ,  $0.311$  and  $0.332$ , respectively. The slight increase in defect concentration for the system containing  $N_c = 900$  particles may be the result of finite size effects associated with the relatively small size of the system. However, finite size effects are not significant at  $\Gamma = 12$ , which is sufficiently far from the phase boundary [72, 73]. The assembly having a mean lattice spacing of  $a = 3.06\ \mu\text{m}$  is employed to study the behavior of the chain at varying field strengths. This lattice is illustrated in Figure 5.2, which provides a comparison between a regular, hexagonal lattice and the former quasi-regular array of magnetic colloids, as well as an experimentally generated lattice of magnetic colloids from the study of Doyle et al. [30]. In studies where the mean lattice spacing is varied, the field strength is held constant at its value corresponding to  $\text{Pe}_\lambda = 5$ .

Upon the introduction of the chain in the array, the implementation of hard-sphere chain-obstacle exclusion and the identification of hooked chain configurations require that a search be performed over obstacles at each time step. This is facilitated by binning the obstacles in the unit cell at the start of the simulation via a linked list implementation of neighbor lists within each bin [106]. The bin dimensions are chosen to be comparable to the mean lattice spacing. Periodic boundary conditions are imposed on the chain at the boundaries of the unit cell by periodically reconstructing the unit cell in the vicinity of the chain. Subsequently, chain-obstacle overlaps may be detected by searching only the bin containing the position of each bead of the chain and the eight surrounding bins, and similarly, hooked chain configurations may be identified by searching only the bins enclosed by the maximum and minimum chain coordinates.

The results of our simulations in the self-assembled magnetic colloid arrays are described in Section 5.4.

## 5.4 Comparison of Model Predictions and Simulation Results

### 5.4.1 Varying Field Strengths

Figures 5.3, 5.4 and 5.5 provide comparisons between the normalized mobility and dispersivity, and the mean distance covered between successive collisions obtained from simulations and those predicted by the CTRW model for the three chain lengths studied at various field strengths at a fixed mean lattice spacing of  $3.06\ \mu\text{m}$ . Furthermore, Figure 5.6 provides a comparison between

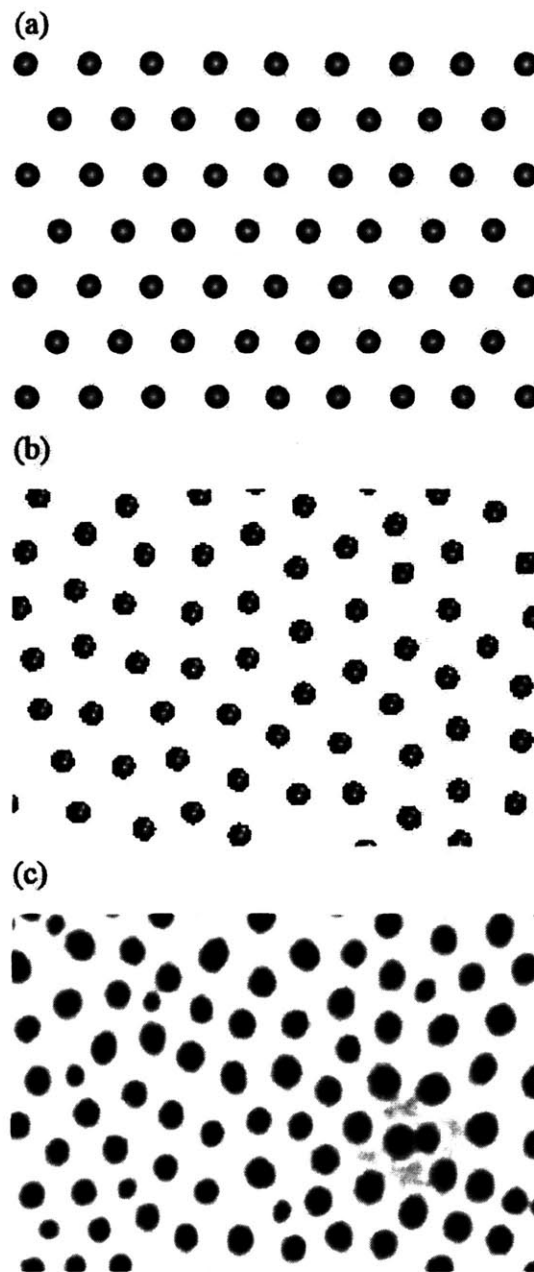


Figure 5.2: (a) A regular, hexagonal lattice, (b) a portion of a self-assembled array of magnetic beads having a mean lattice spacing of  $3.06 \mu\text{m}$ , and (c) a portion of an experimentally generated self-assembled array of magnetic beads from the experimental study of Ref. [30] corresponding to a section of width  $40 \mu\text{m}$ .

the mean collision probability observed in simulations, and those assumed in the present CTRW model, i.e.,  $R_g/a$ , and in the study of Minc et al., i.e.,  $d/a$ . The mobility is normalized with respect to its free solution value  $\mu_0$ , and the dispersivity with respect to  $\mu_0 E a$ . The error bars for the mobility and dispersivity are obtained from the 95% confidence limits for the mean and variance upon fitting the distribution of center of mass  $x$ -coordinates at the end of the simulation relative to their equilibrated values to a normal distribution [105]. Similarly, the error bars for the mean distance covered between collisions and the mean collision probability represent 95% confidence limits for the means of the respective distributions, again upon fitting to a normal distribution. The predictions of the CTRW model for the normalized mobility and dispersivity derive from Equations 5.11 and 5.12, respectively, taken in conjunction with Equations 5.8, 5.13, 5.14 and 5.15. The mean distance between collisions following from the CTRW model is stated in Equation 5.9.

The simulation data depicted in Figures 5.3–5.6 enable the identification of three regimes delineated by the Peclet number for the chain, namely, (i)  $\text{Pe}_{\text{chain}} < O(A/R_g)$ , (ii)  $O(A/R_g) < \text{Pe}_{\text{chain}} \lesssim O(1)$ , and (iii)  $\text{Pe}_{\text{chain}} \gg O(1)$ . Below, we investigate the physical mechanisms operative in these three regimes.

The transition occurring at  $\text{Pe}_{\text{chain}} \sim O(1)$  was encountered earlier in Equation 5.15, and corresponds to the transition from the regime of weak stretching to strong stretching. For  $\text{Pe}_{\text{chain}} \lesssim O(1)$ , the chain is in the near-equilibrium, Gaussian regime and its elasticity is well-described by linear Hooke's law behavior, corresponding to the limit  $\mathcal{L}/L \ll 1$  of the Marko–Siggia law. However, as the Peclet number is increased, the behavior of the chain is increasingly dominated by its finite extensibility, and for  $\text{Pe}_{\text{chain}} \gg O(1)$ , we approach the opposite limit  $\mathcal{L}/L \lesssim 1$  [102].

Figures 5.3 and 5.5 reveal the existence of minima in the chain mobility and the mean distance covered between successive collisions at an  $O(1)$  value of  $\text{Pe}_{\text{chain}}$ . These minima correspond well with the occurrence of a maximum in the collision probability at an  $O(1)$  value of  $\text{Pe}_{\text{chain}}$ , as seen in Figure 5.6. The existence of a minimum in the chain mobility at an  $O(1)$  value of the chain Peclet number was also noted by Patel and Shaqfeh in their study of chain dispersion in random arrays [53]. These authors have interpreted the chain Peclet number as representing the ratio of the escape time for the chain to diffuse away from the obstacle to the hairpin formation time. The time scale  $R_g^2/D_{\text{chain}}$  [with  $D_{\text{chain}} = k_B T/(N\zeta)$ ] for center of mass diffusion over a distance equal to the equilibrium chain radius represents a time scale for escape, enabling the chain to diffuse away from the obstacle, and, hence, avoid hooking, while a time scale of  $L/(\mu_0 E)$  represents a time scale for the formation of a hooked chain configuration. As the ratio of the former to the latter,  $\mu_0 E/D_{\text{chain}}(R_g^2/L) \sim \text{Pe}_{\text{chain}}$ , increases to an  $O(1)$  value, the probability of hooking collisions increases. We caution that the identification of  $\text{Pe}_{\text{chain}}$  with the aforementioned ratio of time scales is strictly valid only in a  $\Theta$  solvent. Upon taking account of the intrachain exclusion arising under good solvent conditions, a weak dependence on the chain length appears in the scaling relation  $\mu_0 E/D_{\text{chain}}(R_g^2/L) \sim N_k^{0.2} \text{Pe}_{\text{chain}}$ , deriving from the scaling law  $R_g^2 \sim N_k^{1.2} b_k^2$  for a self-avoiding walk of  $N_k$  Kuhn steps [50]. However, for the chain sizes presently under consideration,  $N_k \sim 100$  and, consequently,  $N_k^{0.2} \sim 1$ , whereby our conclusions remain valid.

In consequence of the preceding scaling arguments, the probability of forming a hooked, hairpin configuration upon encounter with an obstacle initially increases as the Peclet number increases to approach an  $O(1)$  value. However, as the Peclet number is further increased beyond a value of 1, the chain becomes highly stretched during collisions and the cross-sectional area subsequently presented to the obstacles decreases. As a result, the collision probability decreases, and the mobility and mean distance covered between collisions increase as the Peclet number is increased beyond  $O(1)$

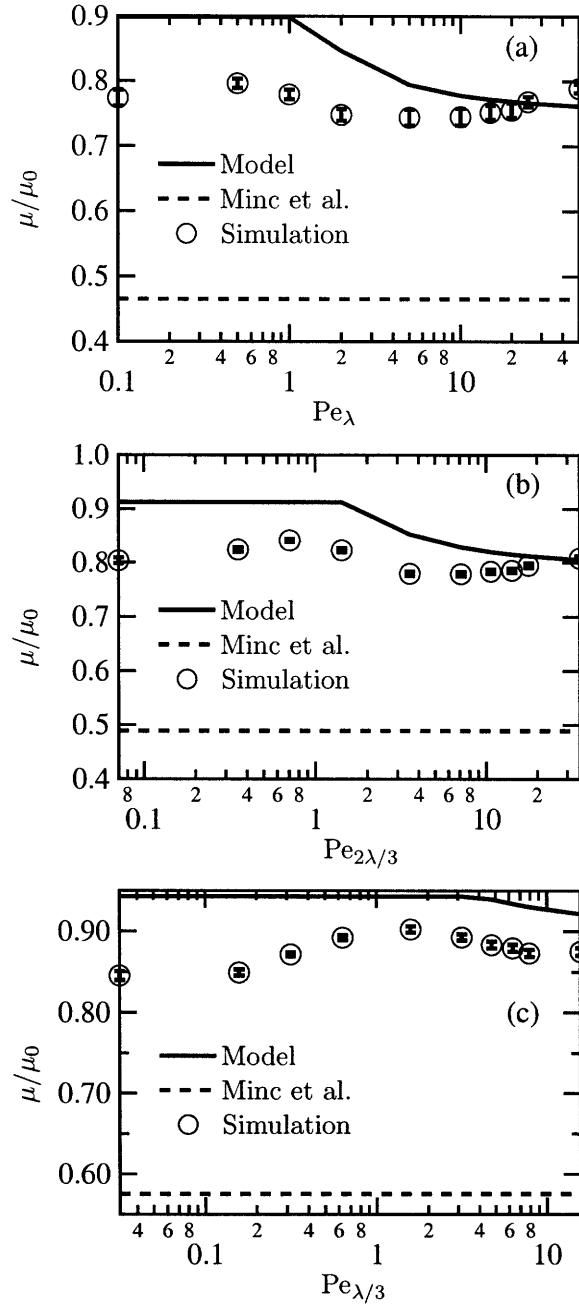


Figure 5.3: Normalized mobility of (a)  $\lambda$ -DNA, (b)  $2\lambda/3$ -DNA, and (c)  $\lambda/3$ -DNA as a function of the Pelet number for  $\lambda$ -,  $2\lambda/3$ - and  $\lambda/3$ -DNA, respectively, obtained by simulation in a self-assembled array of magnetic beads having a mean lattice spacing of  $3.06 \mu\text{m}$  (open circles), that predicted by the model (solid line), and that predicted by the model of Minc et al. (dashed line). The error bars represent 95% confidence bounds on simulation results.

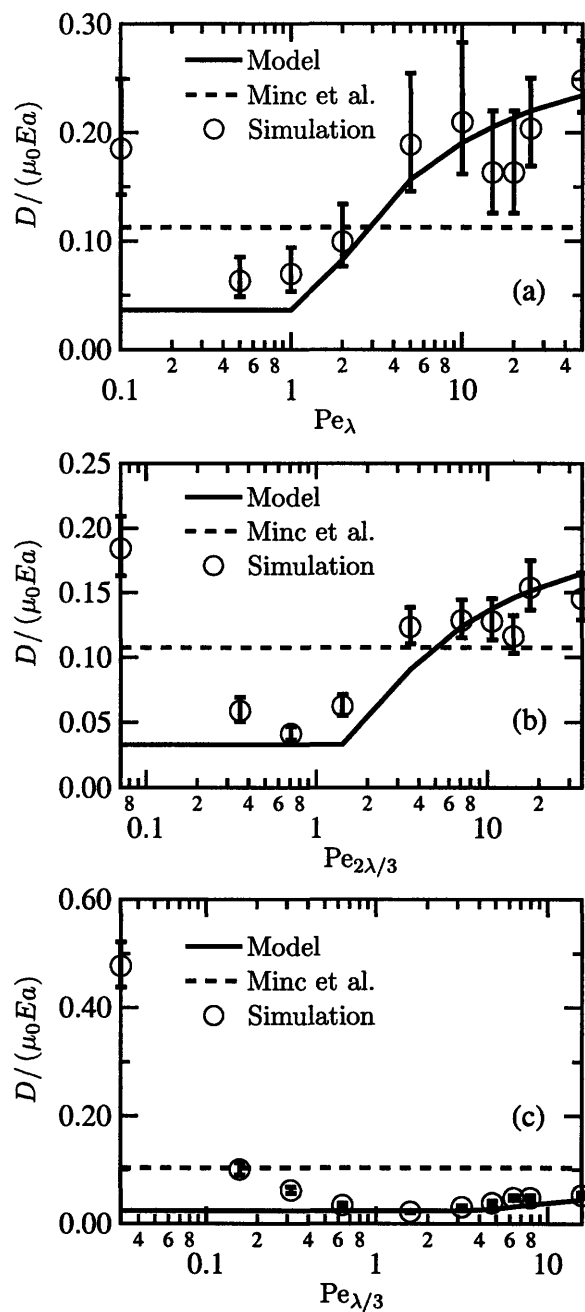


Figure 5.4: Normalized dispersivity of (a)  $\lambda$ -DNA, (b)  $2\lambda/3$ -DNA, and (c)  $\lambda/3$ -DNA as a function of the Peclet number for  $\lambda$ -,  $2\lambda/3$ - and  $\lambda/3$ -DNA, respectively, obtained by simulation in a self-assembled array of magnetic beads having a mean lattice spacing of  $3.06 \mu\text{m}$  (open circles), that predicted by the model (solid line), and that predicted by the model of Minc et al. (dashed line). The error bars represent 95% confidence bounds on simulation results.

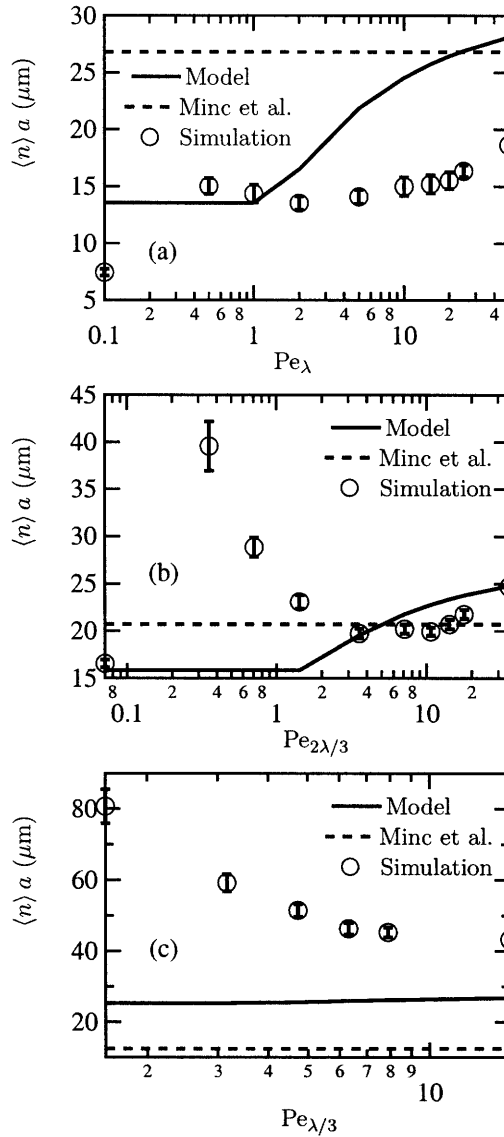


Figure 5.5: Mean distance  $\langle n \rangle a$  covered between successive collisions by (a)  $\lambda$ -DNA, (b)  $2\lambda/3$ -DNA, and (c)  $\lambda/3$ -DNA as a function of the Peclet number for  $\lambda$ -,  $2\lambda/3$ - and  $\lambda/3$ -DNA, respectively, obtained by simulation in a self-assembled array of magnetic beads having a mean lattice spacing of  $3.06 \mu\text{m}$  (open circles), that predicted by the model (solid line), and that predicted by the model of Minc et al. (dashed line). The error bars represent 95% confidence bounds on simulation results. The simulation data shown for  $\lambda/3$ -DNA correspond to  $Pe_{\lambda/3} = 1.58$  and higher only, since collisions were observed to occur in fewer than 10% of the simulated trajectories at lower field strengths.

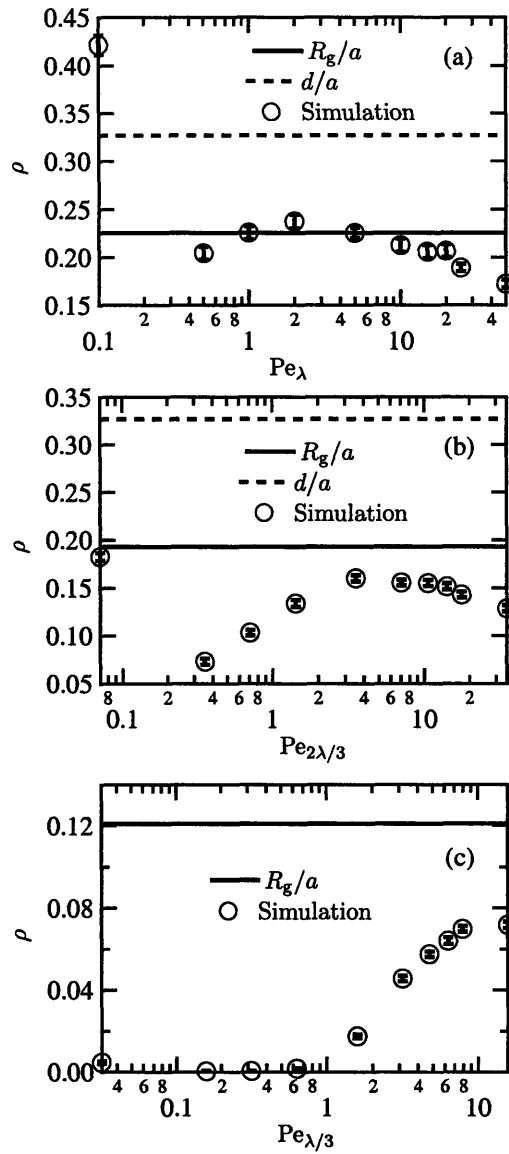


Figure 5.6: Mean collision probability  $\rho$  of (a)  $\lambda$ -DNA, (b)  $2\lambda/3$ -DNA, and (c)  $\lambda/3$ -DNA, calculated as the number of chain-obstacle collisions per lattice column crossed by the chain center of mass, as a function of the Peclet number for  $\lambda$ -,  $2\lambda/3$ - and  $\lambda/3$ -DNA, respectively, obtained by simulation in a self-assembled array of magnetic beads having a mean lattice spacing of  $3.06 \mu\text{m}$  (open circles). The error bars represent 95% confidence bounds on simulation results. Also shown for comparison are the mean collision probability assumed in the model,  $\rho = R_g/a$ , and the areal post density,  $d/a$ . The areal post density is not plotted in (c) due to its much higher value relative to the simulation results.

values. The location of these extrema is shifted to higher values of  $\text{Pe}_{\text{chain}}$  in the case of  $\lambda/3$ -DNA, possibly owing to finite size effects arising in shorter chains.

We next consider the behavior of the chain at Peclet numbers of the order of  $A/R_g$ , or, equivalently, 0.1 for the chain sizes under consideration. We introduce a second parameter  $\text{Pe}_{\text{coil}}$ , defined as follows:

$$\text{Pe}_{\text{coil}} = \frac{\mu_0 E \zeta N}{k_B T / R_g} \equiv \text{Pe}_{\text{chain}} \frac{R_g}{A} \quad (5.19)$$

$\text{Pe}_{\text{coil}}$  represents the ratio of the drag force to the thermal force acting on the chain in its equilibrium, coil configuration. An  $O(1)$  value of  $\text{Pe}_{\text{coil}}$  marks the onset of Gaussian chain stretching, whereas the chain configuration is dominated by thermal forces at lower values of  $\text{Pe}_{\text{coil}}$  [52, 89]. For the systems under consideration, this transition occurs at an  $O(0.1)$  value of  $\text{Pe}_{\text{chain}}$ . Consequently, for  $O(0.1)$  or lower values of  $\text{Pe}_{\text{chain}}$ , the chain retains its coil configuration. The mobilities increase in this regime as the field strength is increased, since the dominant mechanism of chain motion gradually changes from thermal diffusion to convection by the field. Due to the near-absence of chain stretching, the probability of hooking collisions is very low. The apparent increase in collision probability suggested by Figures 5.6(a) and (b) in this regime is merely an artifact of its definition as the number of collisions per lattice spacing covered by the chain, since at low values of  $\text{Pe}_{\text{chain}}$ , the chain center of mass does not cover a significant distance. Moreover, the chain, by darting around obstacles without forming a hooked configuration, is able to satisfy the condition imposed by us to identify collisions that a portion of the chain be present in all four quadrants surrounding the obstacle center. For the same reason, the apparent decrease in the distance covered between successive collisions suggested by Figures 5.5(a) and (b) is also an artifact of the criteria adopted by us for its measurement.

In the regime where  $\text{Pe}_{\text{coil}} \leq 1$ , we may expect the approximation of the DNA coil by a rigid sphere of equivalent radius to be valid. The mobility and diffusivity of a particle in periodic and random lattices under the application of a field have been studied by Gauthier and Slater, and Gauthier et al. via Monte Carlo simulations [107, 108]. These authors found that the mobility and diffusivity of the particle remain constant independent of the field in the regime  $\text{Pe}_{\text{coil}} \leq 1$ , while the diffusivity exhibits a power-law dependence on  $\text{Pe}_{\text{coil}}$  with an exponent of 2 for  $\text{Pe}_{\text{coil}} > 1$ , where  $\text{Pe}_{\text{coil}}$  is now interpreted as the ratio of the force exerted by the field to the thermal force acting over a length scale equal to the particle dimension. Consistent with these findings in the regime  $\text{Pe}_{\text{coil}} \lesssim 1$  or, equivalently,  $\text{Pe}_{\text{chain}} \lesssim 0.1$ , Figure 5.7 reveals that the dispersivity of the chain normalized with respect to its free solution value remains relatively unaffected by the field for  $\text{Pe}_{\text{chain}} \lesssim 0.1$ . The approximation of the chain by a rigid sphere is no longer valid as  $\text{Pe}_{\text{chain}}$  is increased beyond this value. Figure 5.7 suggests a power-law dependence of dispersivity on the chain Peclet number for  $\text{Pe}_{\text{chain}} > 0.1$ , with an exponent of approximately 1.3. The faster-than-linear rise in dispersivity with the chain Peclet number is also manifest in Figure 5.4, and is attributed to the fact that while collisions become increasingly rare at high field strengths, those that do occur involve long holdup times.

We are now in a position to evaluate the ability of the CTRW model to predict the behavior of the chain. The CTRW mechanism is not realized for  $\text{Pe}_{\text{coil}} \sim O(1)$ , owing to the rarity of hooking events, and consequently, the model fails in the regime  $\text{Pe}_{\text{chain}} \sim O(A/R_g)$ . The model is able to predict the dispersivity reasonably well, as depicted by Figure 5.4. However, the model fails to predict the minima in the mobility and the mean distance covered between successive collisions, instead predicting a monotonic decrease in mobility and a monotonic increase in the distance

covered between collisions, respectively, beyond  $Pe_{\text{chain}} = 1$ , as illustrated by Figures 5.3 and 5.5. This failure of the model may be attributed in part to the use of a fixed collision probability  $\rho = R_g/a$  regardless of the field strength. Consequently, the model does not account for the existence of a maximum in  $\rho$  at an  $O(1)$  chain Peclet number. We also note that the dependence of  $\rho$  on the size of the chain is manifestly evident in Figure 5.6, rendering inaccurate the use of the areal post density  $d/a$  for  $\rho$ . In fact, the dependence on the size appears to be stronger than that assumed by Equation 5.13, as suggested by the increase in the disparity between the simulation results and Equation 5.13 as the chain size decreases. Moreover, our use of Equation 5.13 for the collision probability presupposes instantaneous chain relaxation to equilibrium, and fails to take into account the reduction in the transverse radius of gyration, and, hence, the chain cross-section transverse to the electric field direction following a collision at high field strengths. A further shortcoming of Equation 5.13 is that it fails to take into account the dependence of the collision probability on the impact parameter [36, 37, 39] and the distortion of the electric field by the obstacles [39].

Figure 5.8 provides a comparison between the resolution predicted by the model and that obtained from simulation data by means of Equation 5.16 for each pair of chains as a function of the field strength (expressed in terms of  $Pe_\lambda$ ). The mean velocity and dispersivity, measured in the long time limit after the chain has equilibrated in the array, are independent of the array length for a sufficiently long array. In the present study, we consistently employ a separation length of  $L_s = 1$  cm, which is similar to the values used in prior studies [31, 53]. The error bars for the simulation results were computed from the differential error analysis of Equation 5.16, treating the velocities and dispersivities of the two species as independently measurable quantities. The model successfully predicts the nonmonotonic behavior of the resolution with respect to the field strength. The attainment of a high resolution is contingent on the existence of a low dispersivity for both chains and a large velocity difference between the chains. These conditions are met at an  $O(1)$  value of  $Pe_\lambda$ . The decrease in the resolution at high field strengths may be attributed to the increase in dispersivity with the field strength. Furthermore, although the model fails to predict the existence of a minimum in the mobility, it is able to qualitatively capture the decline in the chain mobilities in the region  $Pe_{\text{chain}} \sim O(1)$ , and, consequently, the initial increase in resolution in this region.

Also depicted in Figures 5.3–5.5 and Figure 5.8 are the results for the corresponding quantities predicted by Minc et al. [34] under the same conditions. The model of Minc et al. clearly fails to predict the field-dependence of the chain dynamics and, consequently, the nonmonotonic dependence of the resolution on the electric field strength observed in the simulations conducted in the present study, as well as in previous experimental work [31]. Quantitatively, as manifest in Figure 5.3, Minc et al. predict far lower values of the chain mobility than those observed in simulations, owing to their overestimation of the collision probability and the chain extension.

#### 5.4.2 Varying Mean Lattice Spacings

Figures 5.9–5.12 provide comparisons between the simulation results and model predictions at varying lattice spacings, at a fixed field strength corresponding to  $Pe_\lambda = 5$ , with the error bars again representing 95% confidence bounds on the simulation results. The CTRW model is unable to predict the normalized mobility and dispersivity at a mean lattice spacing of  $1.53 \mu\text{m}$ . The effective mean pore size available to the chain in this array,  $a - d = 0.53 \mu\text{m}$ , is exceeded by the coil diameters of all three DNA chains under consideration. Equation 5.13 predicts an unphysical,

diverging collision probability as  $a$  decreases to 0, leading to the divergence of the dispersivity [cf. Equation 5.12] in this limit, while the mobility [cf. Equation 5.11] approaches a constant value of  $2/3$ . The CTRW mechanism is not realized when  $a - d \lesssim 2R_g$ , and the mechanism is better described by the reptation model [23] or the entropic barrier model [109]. The CTRW model performs well at the remaining lattice spacings, and is able to predict the asymptotic approach of the mobility and dispersivity to  $\mu_0$  and 0, respectively, as the lattice spacing increases.

As evident from Figure 5.12, the collision probability assumed in the CTRW model agrees well with the corresponding simulation results for  $\lambda$ -DNA and  $2\lambda/3$ -DNA. Figure 5.11 reveals that the mean distance covered between successive collisions as predicted by the model accords with simulation results for  $\lambda$ -DNA and  $2\lambda/3$ -DNA at mean lattice spacings below  $7.65 \mu\text{m}$ . However, at mean lattice spacings of  $7.65 \mu\text{m}$  and  $10.21 \mu\text{m}$ , fewer than 2 collisions were observed to occur in as many as up to 50% of all simulated trajectories, which were excluded from the calculation of  $\langle n \rangle a$ . As a result, the simulation results do not reflect the increase in the distance between collisions predicted by the model under these conditions. The field strength at  $\text{Pe}_\lambda = 5$  yields the values  $\text{Pe}_{2\lambda/3} = 3.55$  and  $\text{Pe}_{\lambda/3} = 1.58$ . At these  $O(1)$  values of  $\text{Pe}_{\text{chain}}$ , the collision probability reaches a maximum with respect to the Peclet number and is close to that predicted by Equation 5.13 for  $\lambda$ -DNA and  $2\lambda/3$ -DNA, thus explaining the success of the model. The location of this maximum occurs at a higher value of  $\text{Pe}_{\text{chain}}$  for  $\lambda/3$ -DNA, as pointed out earlier. As a result, there is a large disparity between the collision probability predicted by Equation 5.13 and the much lower values observed in simulations for  $\lambda/3$ -DNA. The corresponding predictions for the mean distance covered between collisions are exceeded by the results obtained from simulation. Collisions were rarely observed to occur at large lattice spacings for  $\lambda/3$ -DNA.

Figure 5.13 depicts the resolution predicted by the model and that obtained from simulation data for each pair of chains as a function of the lattice spacing. The error bars have been computed as before from the differential error analysis of Equation 5.16. The CTRW model predicts the existence of a maximum in the resolution with respect to the lattice spacing, and the decrease of the resolution to 0 at both small and large lattice spacings. In the regime  $a - d > 2R_g$ , the CTRW model correctly predicts the decrease in the resolution between  $\lambda$ -DNA and  $\lambda/3$ -DNA, and between  $\lambda/3$ -DNA and  $2\lambda/3$ -DNA, as the lattice spacing is increased. The quantitative differences between model predictions and simulation results may be attributed to the failure of the model to correctly describe the collision probability for  $\lambda/3$ -DNA. Again in the regime of its validity, the resolution predicted by the model between  $\lambda$ -DNA and  $2\lambda/3$ -DNA is close to that obtained from simulation within error bars. Unfortunately, it is not possible to conclusively identify the existence of a maximum in the resolution from the simulation data of Figure 5.13(b), owing to the size of the error bars.

The predictions of Minc et al. [34], also illustrated in Figures 5.9–5.11 and Figure 5.13, do not adequately capture the chain dynamics with increase in the lattice spacing. As apparent from Figure 5.9, Minc et al. predict much lower values of the mobility than those observed in simulations. Moreover, as shown in Figure 5.10, they predict the existence of a maximum in the normalized dispersivity with respect to the lattice spacing, not seen to occur in simulations. Their predictions fail to reflect the rapid decline in the resolution with increase in the lattice spacing seen in the simulation data of Figure 5.13. At the field strength under consideration, the chains are relatively strongly stretched, and the assumptions made by Minc et al. [34] regarding the holdup time and the collision probability, rather than their neglect of the field-dependence of chain extension, may be responsible for the discrepancies between their predictions and the simulation results.

## 5.5 Discussion

In the present study, we provide a generalization of the CTRW model of DNA dynamics in an array of obstacles [34] with account for the electric field dependence of the chain extension during collisions. We make use of a semi-empirical expression recently developed from studies on chain collisions with single obstacles [42] for the holdup time during which the chain center of mass motion is impeded by the obstacle following a collision. In addition, we take into account the dependence of the collision probability on the chain size.

We evaluate the model by comparing its predictions with the results obtained from Brownian dynamics simulations of bead-spring models of  $\lambda$ -DNA,  $2\lambda/3$ -DNA and  $\lambda/3$ -DNA in obstacle arrays. The use of a regular, hexagonal lattice yields high mobilities approaching the free solution electrophoretic mobility, and very low dispersivities, and, hence, proves ineffective in achieving separation between chains of different sizes. Instead, we select a self-assembled array of magnetic colloids as being representative of arrays used in experimental studies [30–32]. These arrays are generated via Brownian dynamics simulations of magnetic colloids that interact with each other via a repulsive point dipolar potential and mutual hard-sphere exclusion in two dimensions [72, 73]. Our studies are conducted in an array having a mean lattice spacing of  $3.06 \mu\text{m}$  at several experimentally accessible electric field strengths, and at a constant electric field strength equivalent to a Peclet number of  $\text{Pe}_\lambda = 5$  at several values of the mean lattice spacing. Our neglect of hydrodynamic interactions in all simulations is partially justified by the screening of hydrodynamic interactions in complicated microchannel geometries. We also neglect the distortion of the electric field due to the presence of obstacles, a factor that may have adversely impacted our ability to accurately model the probability of chain-obstacle collision [39].

Our simulation studies of chain dynamics at varying Peclet numbers enable the identification of three regimes demarcated by the chain Peclet number. The regime  $\text{Pe}_{\text{chain}} \lesssim O(A/R_g)$  corresponds to the situation wherein thermal equilibrium has yet to be disturbed, i.e., the drag on the chain,  $\mu_0 EN\zeta$ , is exceeded by the thermal force  $k_B T/R_g$  acting on the chain in its equilibrium, coil configuration. Under such conditions, the formation of hooked chain configurations is unlikely, and the mechanism of the CTRW model is not realized. The range  $O(A/R_g) < \text{Pe}_{\text{chain}} \lesssim O(1)$  is associated with chain stretching in the Gaussian regime, whereby the chain extension is well-described by the low-force limit of the Marko-Siggia formula [52]. The chain mobility reaches a minimum at an  $O(1)$  value of  $\text{Pe}_{\text{chain}}$ , corresponding to the attainment of a maximum in the collision probability. For  $\text{Pe}_{\text{chain}} \gg O(1)$ , the chain extension is derived from the large-force limit of the Marko-Siggia law [52]. In this regime, the probability of chain-obstacle collision decreases, and consequently, the mobility increases. At the same time, the chain dispersivity increases with the field strength, owing to the fact that while collisions are rare, they involve long holdup times when they do occur.

The CTRW model, in failing to account for the dependence of the collision probability on the field strength, is unable to predict the existence of a minimum in the chain mobility with respect to the Peclet number. However, it satisfactorily predicts the increase in dispersivity with increasing field strength and the initial decline in the mobility at  $O(1)$  values of the Peclet number, and consequently, is able to predict the existence of a maximum in the separation resolution with respect to the field strength. Under conditions of constant electric field strength, the CTRW model is able to provide reasonable predictions of the chain dynamics as the lattice spacing is varied in the regime of its applicability, when the mean pore size available to the chain is between obstacles

exceeds the chain size.

The use of a constant collision probability, independent of the electric field strength, is an obvious weakness of the model. The model also does not account for the effect of the distortion of the electric field lines in the vicinity of the obstacles and the impact parameter on the collision probability [36,37,39]. Yet another source of error is the assumption that the chain instantaneously relaxes to a coil at the location of its leading end following a collision, and subsequently moves at its free solution electrophoretic velocity  $\mu_0 E$  until the next collision occurs.

Owing to the paucity of experimental studies on the systems under consideration, we are able to provide only limited comparisons with experiment. The nonmonotonicity of the separation resolution with respect to the electric field strength, as predicted by us, was observed by Minc et al. in studies on the separation of  $\lambda$ -DNA and  $2\lambda$ -DNA chains [31]. These authors also observed the separation resolution to increase upon changing the lattice spacing from  $3.8 \mu\text{m}$  to  $4.1 \mu\text{m}$ . This observation, taken in conjunction with the decrease in resolution that must necessarily follow at large lattice spacings upon approaching the single-obstacle limit, renders the resolution nonmonotonic with respect to the lattice spacing. However, in the latter study, the obstacle diameters were concurrently changed from  $1 \mu\text{m}$  to  $1.4 \mu\text{m}$ , whereby the increase in resolution cannot conclusively be attributed to the increase in the lattice spacing. We are unable to confirm the existence of a maximum in the separation resolution with respect to the lattice spacing, as predicted by our model, owing to the size of the error bars associated with our simulation results.

Our findings shed light on the behavior of field-driven polymers in post arrays wherein the pore size is large compared to the coil size of the polymer. Moreover, our results are expected to aid in the appropriate selection of parameters for the operation of obstacle arrays employed for the size separation of DNA chains and similar molecules.

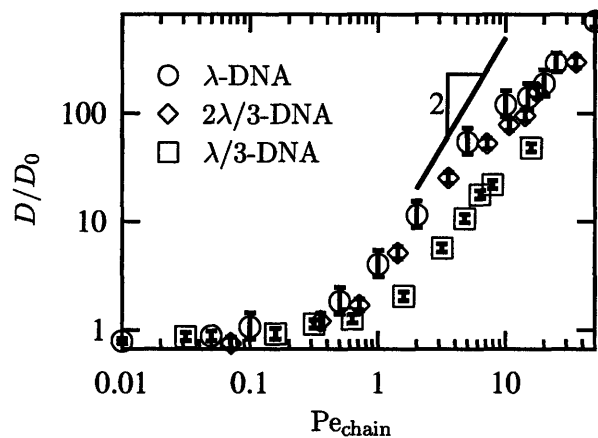


Figure 5.7: *Dispersivity of  $\lambda$ -DNA (circles),  $2\lambda/3$ -DNA (diamonds), and  $\lambda/3$ -DNA (squares) normalized with respect to the free solution diffusion coefficient of a free draining chain, i.e.,  $D_0 = k_B T / (N\zeta)$ , as a function of the Peclet number for  $\lambda$ -,  $2\lambda/3$ - and  $\lambda/3$ -DNA, respectively, obtained by simulation in a self-assembled array of magnetic beads having a mean lattice spacing of  $3.06 \mu\text{m}$ . The error bars represent 95% confidence bounds on simulation results. Above a Peclet number of 0.1 for each chain length,  $D/D_0$  exhibits a power-law dependence on  $Pe_{\text{chain}}$  with an exponent of approximately 1.3. Also shown for comparison is a line of slope 2, representing the power-law dependence of the normalized diffusivity  $D/D_0$  of a rigid particle on the field strength in a lattice of periodic obstacles [108].*

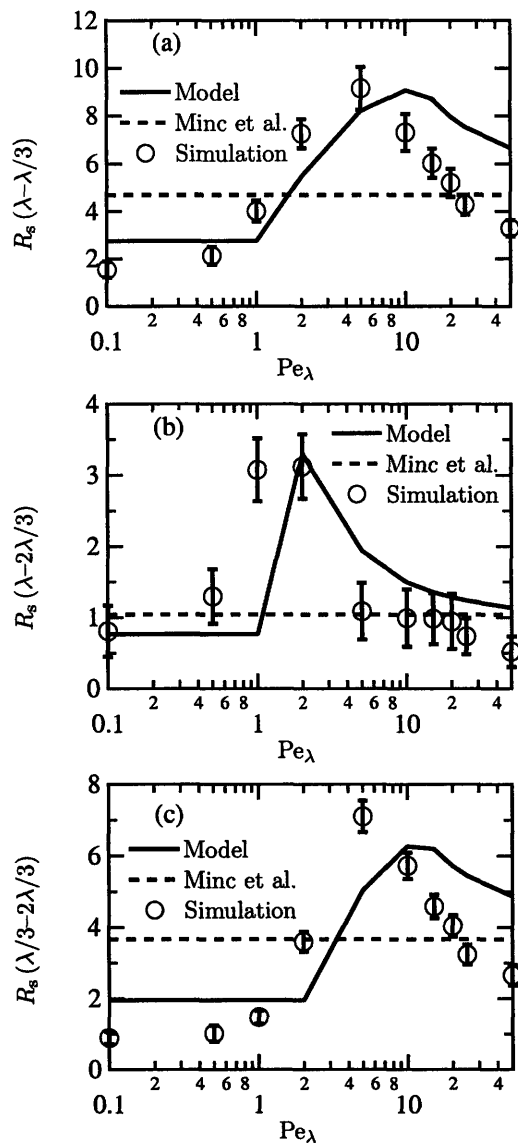


Figure 5.8: Separation resolution between (a)  $\lambda$ - and  $\lambda/3$ -DNA, (b)  $\lambda$ - and  $2\lambda/3$ -DNA, and (c)  $\lambda/3$ - and  $2\lambda/3$ -DNA as a function of  $Pe_\lambda$  calculated by simulation in a self-assembled array of magnetic beads having a mean lattice spacing of  $3.06 \mu\text{m}$  (open circles) and that predicted by the model (solid line) for a separation length of  $L_s = 1 \text{ cm}$ . The error bars represent 95% confidence bounds on simulation results. Also shown for comparison is the separation resolution predicted by the model of Minc et al. (dashed line).

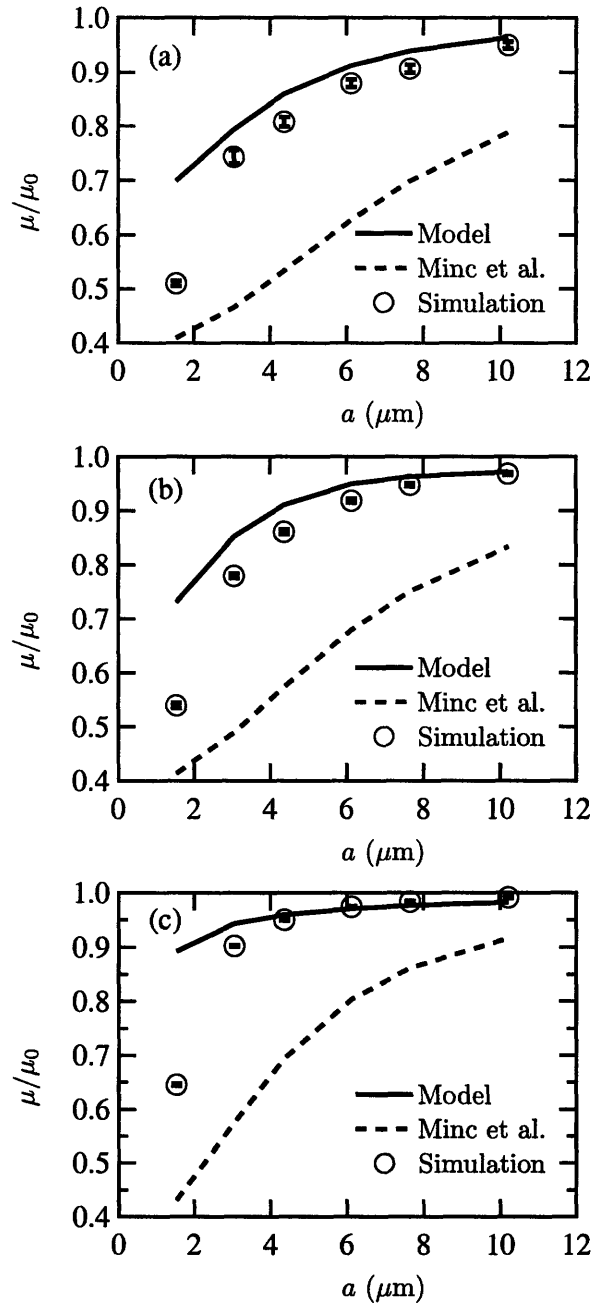


Figure 5.9: Normalized mobility of (a)  $\lambda$ -DNA, (b)  $2\lambda/3$ -DNA, and (c)  $\lambda/3$ -DNA as a function of the mean lattice spacing obtained by simulation in a self-assembled array of magnetic beads at  $\text{Pe}_\lambda = 5$  (open circles), that predicted by the model (solid line), and that predicted by the model of Minc et al. (dashed line). The error bars represent 95% confidence bounds on simulation results.

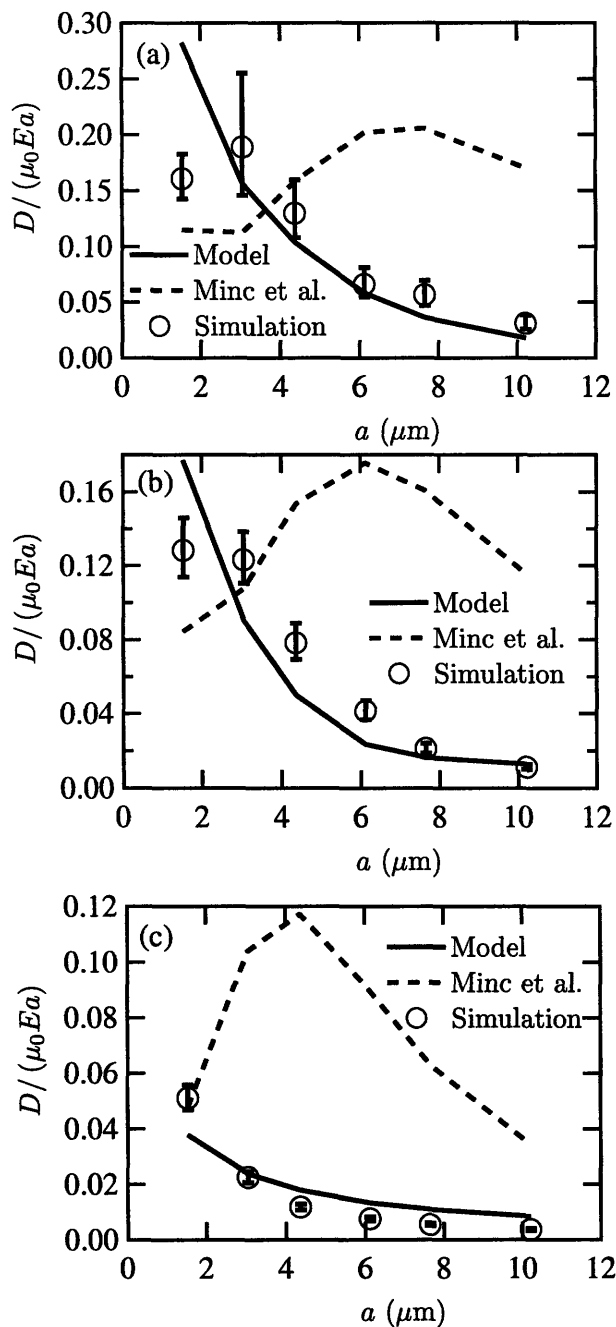


Figure 5.10: Normalized dispersivity of (a)  $\lambda$ -DNA, (b)  $2\lambda/3$ -DNA, and (c)  $\lambda/3$ -DNA as a function of the mean lattice spacing obtained by simulation in a self-assembled array of magnetic beads at  $\text{Pe}_\lambda = 5$  (open circles), that predicted by the model (solid line), and that predicted by the model of Minc et al. (dashed line). The error bars represent 95% confidence bounds on simulation results.

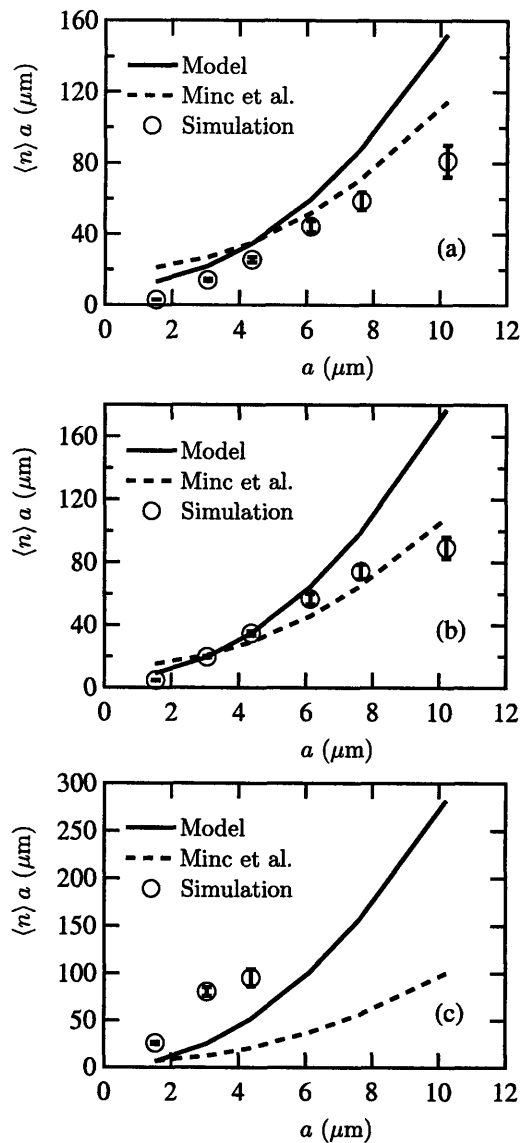


Figure 5.11: Mean distance covered between successive collisions by (a)  $\lambda$ -DNA, (b)  $2\lambda/3$ -DNA, and (c)  $\lambda/3$ -DNA as a function of the mean lattice spacing obtained by simulation in a self-assembled array of magnetic beads at  $\text{Pe}_\lambda = 5$  (open circles), that predicted by the model (solid line), and that predicted by the model of Minc et al. (dashed line). The error bars represent 95% confidence bounds on simulation results. The simulation data shown for  $\lambda/3$ -DNA correspond to  $a = 1.53 \mu\text{m}$ ,  $a = 3.06 \mu\text{m}$ , and  $a = 4.37 \mu\text{m}$  only, since collisions were found to occur in fewer than 10% of the simulated trajectories at larger values of the mean lattice spacing.

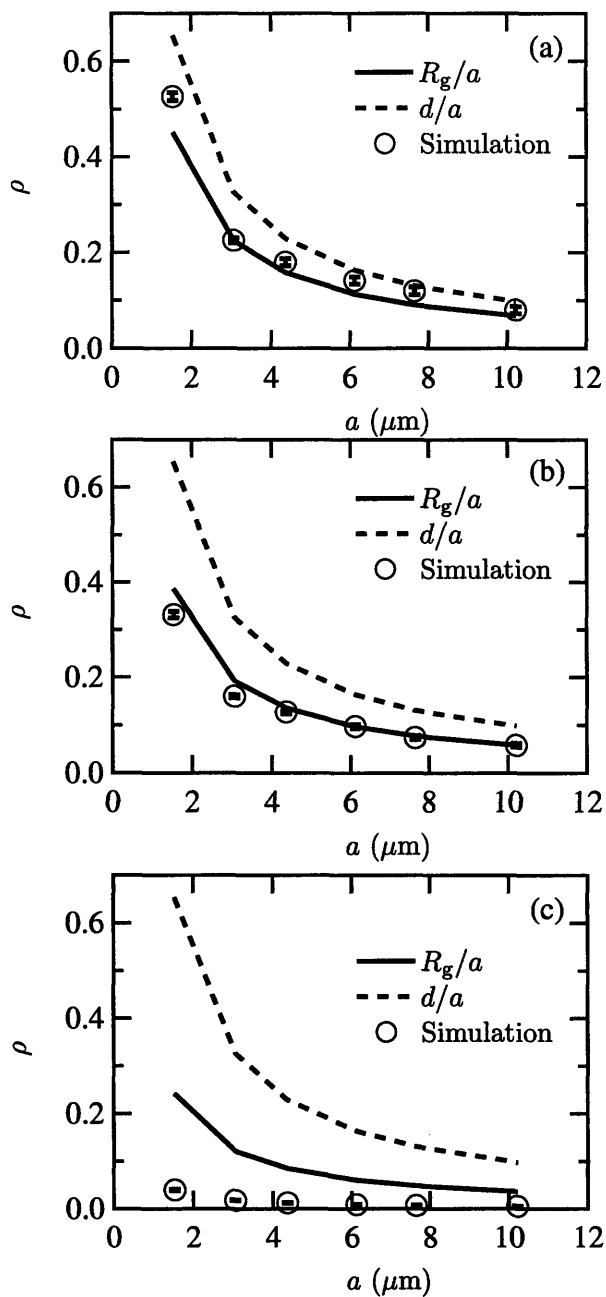


Figure 5.12: Mean collision probability  $\rho$  of (a)  $\lambda$ -DNA, (b)  $2\lambda/3$ -DNA, and (c)  $\lambda/3$ -DNA as a function of the mean lattice spacing, calculated from simulation as the number of chain-obstacle collisions per lattice column crossed by the chain center of mass at  $\text{Pe}_\lambda = 5$  in a self-assembled array of magnetic beads. Also shown for comparison are the mean collision probability assumed in the model,  $\rho = R_g/a$ , and the areal post density,  $d/a$ .

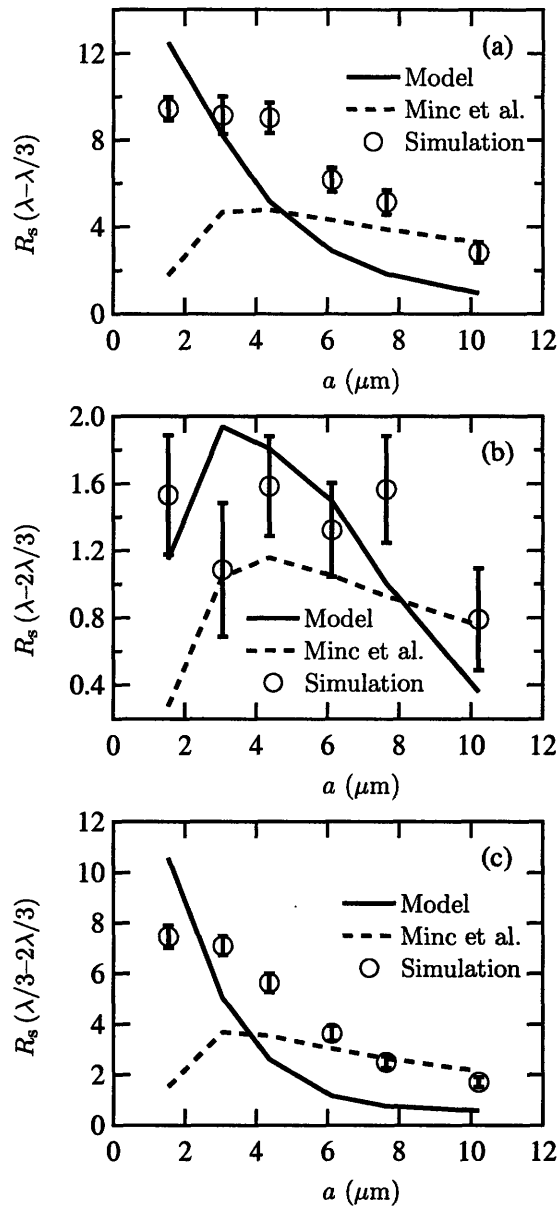


Figure 5.13: Separation resolution between (a)  $\lambda$ - and  $\lambda/3$ -DNA, (b)  $\lambda$ - and  $2\lambda/3$ -DNA, and (c)  $\lambda/3$ - and  $2\lambda/3$ -DNA as a function of the mean lattice spacing calculated by simulation in a self-assembled array of magnetic beads at  $\text{Pe}_\lambda = 5$  (open circles) and that predicted by the model (solid line) for a separation length of  $L_s = 1$  cm. The error bars represent 95% confidence bounds on simulation results. Also shown for comparison is the separation resolution predicted by the model of Minc et al. (dashed line).



## *Conclusions and Outlook*

---

This thesis is concerned with dynamical effects induced by the existence of potential gradients, where the potential field may be equated with a temperature, concentration or an electric potential field. Particle motions in incompressible Stokes flow under conditions of inhomogeneous temperature or concentration, or upon the imposition of an electric field, are considered in Chapters 2 and 3. The dynamics of an electric field driven DNA chain in microfluidic separation devices comprise the subject of Chapters 4 and 5.

### **6.1 Fluid Dynamics in Inhomogeneous Fields**

In Chapters 2 and 3, we consider the motion of spherical and nonspherical particles in Stokes flows induced by the existence of slip at the fluid–particle interface. Our studies are presented in the context of thermally-induced slip of a gas at the surface of a nonuniformly heated solid. However, more generally, slip is also known to occur at liquid–solid interfaces under conditions of inhomogeneous temperature or concentration. Particle motion in the two cases is referred to as thermophoresis and diffusiophoresis, respectively. Another instance of phoretic transport is the motion of a charged particle in an electrolytic liquid upon the imposition of an electric field, referred to as electrophoresis and explained by the imposition of an electrokinetic slip condition at the particle–liquid interface.

The imposition of a slip condition at the fluid–particle interface is rationalized in all cases by the existence of a scale separation between the thickness of the interfacial layer of fluid proximate

to the solid surface and the macroscopic size of the solid particle. For instance, the characteristic thickness of the layer of gas adjoining the solid surface (termed the Knudsen layer) is the mean free path of the gas. The asymptotic solution of the Boltzmann equation in the Knudsen layer and in the bulk gas subject to diffuse reflection of gas molecules at the solid surface yields the velocity at the outer limit of the inner, Knudsen layer, which serves as the continuum boundary condition to be imposed on the flow of the outer, bulk fluid [9]. Similarly, in the case of phoretic transport in liquids, the phoretic slip condition to be imposed on bulk liquid flow is equated to the velocity of the liquid at the outer limit of the inner, interfacial region adjacent to the particle surface, though the velocity satisfies no-slip at the particle surface [20]. Moreover, the thermal slip condition first proposed by Maxwell [3] and later derived rigorously from the kinetic theory of gases [2, 9, 10] is identical in form to the slip condition employed to describe phoretic transport in liquids [20]. As a result, our studies are equally applicable to both situations.

In Chapter 2, we extend Faxen's laws for the force and torque on a spherical particle in an arbitrary incompressible Stokes flow field to include the effect of slip at the particle surface. Our results may be employed to study thermophoretic, diffusiophoretic or electrophoretic particle motions in arbitrary geometries. We treat the motion of a nonspherical particle in Chapter 3. Specifically, we study the flow field around a uniformly translating triaxial ellipsoid modeled as a slightly deformed sphere in the presence of thermal slip in an otherwise quiescent fluid, and confirm that the thermophoretic velocity of a force- and torque-free, thermally insulated particle is independent of its shape, size and orientation. Our general technique may be applied to study the slip-induced motion of other nonspherical, asymmetric particles.

## 6.2 DNA Dynamics in Microfluidic Separation Devices

The size-based separation of DNA chains driven by the imposition of an electric field through an array of obstacles has been experimentally established to occur [29, 30]. However, simple models enabling the accurate a priori prediction of the efficacy of these separation devices have yet to be developed. The development of such models is expected to facilitate device design and operation in such a way as to maximize the separation resolution between chains of different sizes.

The development of a predictive model of device performance requires detailed knowledge of chain-obstacle interactions in the array. While several studies have focused on single chain-obstacle collisions, the nature of tension propagation, which governs the unraveling of the two arms of the chain on either side of the obstacle subsequent to a chain-obstacle collision, remains unknown from prior studies. We investigate this issue in Chapter 4, wherein we study the unraveling of Rouse and wormlike chains upon the imposition of solvent flow (or equivalently, under an imposed electric field). We employ normal mode analysis to investigate the behavior of linear, Rouse chains, and perform Brownian dynamics simulations of the bead-spring model to simulate DNA behavior in strong fields. We subsequently demonstrate that the tension propagation in Rouse chains (representative of DNA stretching in weak fields) is diffusive, whereas that in wormlike chains (modeling DNA dynamics under conditions of strong fields) is convective. These results are of relevance not only to chain unraveling subsequent to chain-obstacle collisions in an obstacle array, but also to other situations involving chain entanglement and transient chain unraveling. These include dilute solution capillary electrophoresis [25, 26] and flows of polymer solutions [70].

The insight into single chain-obstacle collisions provided by the study of Chapter 4 enables the critical reexamination of modeling assumptions made in prior studies [34, 35], as well as the

development of a more accurate model of DNA dynamics in an array of obstacles. In Chapter 5, we extend the continuous-time random walk model [71] of DNA dynamics in the array to account for the dependence of chain dynamics on the electric field strength, and make analytical predictions of the resolution achievable between different chain sizes. Concurrently, we perform Brownian dynamics simulations of DNA chains in an obstacle array for comparison with the model predictions. For this purpose, an obstacle array constituted by magnetic beads modeled as hard spheres with point repulsive magnetic dipoles at their centers at a magnetic field strength such that the array lies in the liquid phase (and, hence, lacks both translational and orientational order) is employed [72,73]. We study the effect of electric field strength and lattice spacing on the separation resolution between different chain sizes, and demonstrate that our analytical model correctly predicts the nonmonotonicity of separation resolution with respect to the electric field strength, as observed in experiments [31].

One open issue that bears investigation is the effect of array order on chain dynamics. A perfectly ordered, hexagonal lattice provides straight channels, enabling the DNA coil to transit through the array without suffering collisions. Disorder is essential in inducing chain-obstacle collisions. The degree of order in a two-dimensional array of magnetic beads may be varied by varying the magnetic field strength at which the array is generated. At an infinite magnetic field strength (or equivalently, at zero temperature), the array is a perfectly ordered crystal, whereas at finite magnetic field strengths, the thermal motion of the magnetic beads causes defects and dislocations to exist in the crystal. At very low magnetic field strengths, the array possesses neither long range translational order nor long range orientational order, and lies in the liquid phase. In our simulations thus far, we have employed arrays in the liquid phase. As the magnetic field strength is increased from zero, a phase transition from the liquid to the hexatic phase involving the onset of quasi-long range orientational order in the hexatic phase occurs at some specific magnetic field strength, followed by a transition to the solid phase possessing quasi-long range translational order as the magnetic field strength is further increased [110]. Preliminary investigations conducted by us (not presented in this thesis) reveal that DNA undergoes a transition from the stretched conformation to the coiled conformation in the array as the phase of the array is changed from the liquid to the solid phase. The coiled conformation of DNA in the array reveals the existence of straight channels through which the chain can pass without hindrance, and such array structures are ineffective in achieving separation. These studies further enable the appropriate design of obstacle arrays to achieve optimal size-based DNA separation.



# *Parameter Estimation for Brownian Dynamics Simulation of $\lambda$ -DNA with Hydrodynamic Interactions*

---

## A.1 Simulation Procedure

In this Appendix, we provide the results of a parametric study of  $\lambda$ -DNA modeled by a bead-spring chain having  $N = 11$  beads at a discretization of  $N_{k,s} = 19.8$  Kuhn steps per spring at equilibrium under good solvent conditions. Hydrodynamic interactions among the beads are modeled via the RPY tensor [cf. Equation 1.22], and Cholesky decomposition [111] is employed to calculate the  $\mathbf{B}$  tensor from the diffusion tensor  $\mathbf{D}$ . We make use of the modified Marko-Siggia spring force law given by Equation 1.11 and adopt the mid-force criterion of Underhill and Doyle [55]. This criterion, which is known to eliminate the error between the wormlike chain force-extension behavior and that predicted by the bead-spring model at 50% mean fractional chain extension, yields the value  $\lambda = 1.1$  for the ratio of the effective to the true persistence length with  $N_{k,s} = 19.8$  [55]. Equation 1.21 is employed to account for intrachain exclusion in a good solvent. Moreover, we replace the Gaussian Wiener processes  $d\mathbf{W}_j$ ,  $j = 1, \dots, N$ , appearing in Equations 1.17 and 1.23 with a vector of random deviates uniformly distributed in the interval  $[-0.5, 0.5]$ , whereby the last term on the right hand side of Equations 1.17 and 1.23 is replaced with  $\sqrt{24dt}\mathbf{B}_{ij} \cdot \mathbf{n}_j$  and  $\sqrt{24dt}(k_B T / \zeta) \mathbf{n}_i$ ,

respectively, where  $\mathbf{n}_j$ ,  $j = 1, \dots, N$ , are random vectors whose three components are uniform in  $[-0.5, 0.5]$  [49,112]. Algorithms for the generation of uniform pseudorandom variables are described in Ref. [111]. We adopt the semi-implicit predictor–corrector method [63,64] for the integration of Equations 1.17 and 1.23 with  $\mathbf{v} = \mathbf{0}$  by means of Brownian dynamics simulation.

We wish to determine values of the parameters  $v$  and  $a$ , representing the excluded volume parameter and the bead radius, respectively, in such a way as to most closely reproduce the behavior of a  $\lambda$ -DNA molecule in a good solvent. For this purpose, we attempt to reproduce the experimentally measured equilibrium radius of gyration, diffusion coefficient and relaxation time of  $\lambda$ -DNA through Brownian dynamics simulation.

The radius of gyration of stained  $\lambda$ -DNA under good solvent conditions has been computed by Smith et al. [65], who made measurements of chain diffusivity and used the Zimm model to relate the radius of gyration to the diffusivity [50]. These authors report the values  $R_g = 0.73 \mu\text{m}$  and  $D = 0.47 \mu\text{m}^2/\text{s}$  for the radius of gyration and diffusivity, respectively, at a temperature of  $T = 297 \text{ K}$  in a solvent of viscosity  $\eta = 0.95 \text{ cP}$ . More recently, Chen et al. [47] have reported the values  $R_g = 0.69 \mu\text{m}$  and  $D = 0.45 \mu\text{m}^2/\text{s}$  for the radius of gyration and diffusivity, respectively, at a temperature of  $T = 294 \text{ K}$  in a solvent of viscosity  $\eta = 1.08 \text{ cP}$ . By means of the proportionality  $D \propto T/\eta$ , the measurements of Smith et al. [65] yield the slightly lower value  $0.41 \mu\text{m}^2/\text{s}$  for the diffusivity under the conditions at which the study of Chen et al. [47] was conducted. In this Appendix, we determine  $v$  and  $a$  so as to best match the measurements of Chen et al. [47].

The relaxation time of stained  $\lambda$ -DNA was reported by Perkins et al. [66] and Smith and Chu [67] to be  $\tau = 3.89 \text{ s}$  in a solvent of viscosity  $41 \text{ cP}$ . We employ the relation  $\tau \propto \eta$  [49] to deduce the value  $\tau = 0.1 \text{ s}$  in a solvent of viscosity  $\eta = 1.08 \text{ cP}$ . Relaxation times as high as twice this value have been reported by Babcock et al. [68] and Li et al. [69], although these differences have been attributed to errors in viscosity measurement [49,68]. We here determine  $a$  so as to best reproduce the value  $\tau = 0.1 \text{ s}$  in a solvent of viscosity  $\eta = 1.08 \text{ cP}$ . (Note that the studies cited above report the longest stress relaxation time, whereas the relaxation times defined in Chapter 4 are conformational relaxation times.)

We employ the nondimensionalization introduced earlier in Chapter 4, and set the units of length, energy and diffusivity equal to the maximum spring length  $Q_0$ ,  $k_B T$  and  $k_B T/\zeta$ , respectively, where  $\zeta = 6\pi\mu a$  is the Stokes drag coefficient for a single bead of radius  $a$ . Consequently, our unit of force becomes  $k_B T/Q_0$ , and the unit of time adopted by us is  $\zeta Q_0^2/(k_B T)$ . Following the notation introduced in Chapter 4, nondimensional variables are denoted by the symbol “~” surmounting the corresponding dimensional variable. In our simulations, we employ a nondimensional time step size of  $5 \times 10^{-4}$ , corresponding to 10% of the relaxation time of a single spring modeled as a Hookean dumbbell, i.e.,  $(\zeta/4)N_{k,s}b_k^2/(3k_B T)$ . Our initial configuration is one in which all springs are aligned along one of the axes (say, the  $x$ -axis), and are at 75% extension. We simulate the chain behavior for a time period corresponding to 50 relaxation times and, after a duration of 10 relaxation times has elapsed from the start of the simulation, we sample the center of mass position and mean squared displacement, stretch, and squared stretch at time intervals corresponding to 5% of the chain relaxation time, where the relaxation time is estimated as the longest stress relaxation time  $\tau_r = \zeta/(8H)[\sin(\pi/(2N))]^{-2}$  for a Rouse chain of  $N$  beads [57]. The  $\mathbf{D}$  and  $\mathbf{B}$  tensors are updated once in every 10 time steps (with the corresponding time interval being the relaxation time of a single spring). The results for the diffusivity thereby obtained are found to differ by less than 2% from the values obtained on updating  $\mathbf{D}$  and  $\mathbf{B}$  at every time step.

Averages are performed at the sampled time points over an ensemble of  $N_{\text{ens}} = 100$  chains

to determine the mean chain stretch  $\langle X \rangle$ , radius of gyration  $R_g$ , and center of mass short- and long-time diffusivities (denoted by  $D_S$  and  $D_L$ , respectively), defined by the following expressions:

$$\langle X \rangle = \frac{1}{N_{\text{ens}}} \sum_{m=1}^{N_{\text{ens}}} \left( \max_i x_{i,m} - \min_i x_{i,m} \right) \quad (\text{A.1})$$

where  $x_{i,m}$  refers to the  $x$ -coordinate of bead  $i$ ,  $i = 1, \dots, N$ , in trajectory  $m$ ,  $m = 1, \dots, N_{\text{ens}}$ ,

$$R_g^2 = \left\langle \frac{1}{N} \sum_{i=1}^N |\mathbf{r}_i - \mathbf{r}_{\text{cm}}|^2 \right\rangle \quad (\text{A.2})$$

with  $\mathbf{r}_i$  the position of bead  $i$  for  $i = 1, \dots, N$ ,  $\mathbf{r}_{\text{cm}}$  the center of mass position, and with the angular brackets representing the ensemble-average,

$$D_S = \left\langle \frac{|\mathbf{r}_{\text{cm}}(t + dt) - \mathbf{r}_{\text{cm}}(t)|^2}{6dt} \right\rangle \quad (\text{A.3})$$

where  $dt$  is the time step size, and

$$D_L = \lim_{t \rightarrow \infty} \left\langle \frac{|\mathbf{r}_{\text{cm}}(t) - \mathbf{r}_{\text{cm}}(0)|^2}{6t} \right\rangle \quad (\text{A.4})$$

where, in the calculation of  $D_S$  and  $D_L$ , time-averaging is performed in addition to ensemble-averaging over all sampled time points after an initial time period of 10 relaxation times has elapsed, and  $\mathbf{r}_{\text{cm}}(0)$  refers to the center of mass position 10 relaxation times after the start of the simulation. We verified that the running averages plotted as a function of time after the initial duration of 10 relaxation times converged to the equilibrium values of  $D_S$  and  $D_L$ . Time-averaging is also performed in the same manner to compute the equilibrium values of chain stretch and  $R_g$ . In addition to the mean stretch, we measured the mean squared stretch, denoted by  $\langle X^2 \rangle$ , at all sampled time points. The longest relaxation time  $\tau$  is obtained from the expression

$$\ln \left( \langle X^2 \rangle(t) - \langle X^2 \rangle_{\text{eq}} \right) = C - \frac{t}{\tau} \quad (\text{A.5})$$

where the subscript “eq” refers to the equilibrium value determined via time- and ensemble-averaging and  $C$  is a constant, by fitting Equation A.5 to a straight line for the time interval during which the chain stretch ranges from 30% to 10% chain extension. As already stated in Chapter 4, convergence with time step size and ensemble size is achieved. The equilibrium radius of gyration, chain stretch, and short- and long-time diffusivities of  $\lambda$ -DNA were found to vary by less than 2% upon reducing the time step size to  $10^{-4}$  and even further to  $10^{-5}$ . Upon increasing the ensemble size to 200 and 400 chains, the equilibrium chain stretch was found to differ by less than 1% from the corresponding values obtained from an ensemble of 100 chains for  $\lambda$ -DNA.

## A.2 Code Validation

We validated our code at the outset to ensure that we correctly reproduce the values obtained from simulation by Jendřejack et al. [60] with use of the parameters specified by these authors, namely,  $a = 77$  nm and  $v = 0.0012$   $\mu\text{m}^3$ . For this purpose alone, we employ the (unmodified) Marko–Siggia law with  $\lambda = 1$  [cf. Equation 1.11]. In a solvent of viscosity 43.3 cP and at the temperature  $T = 296$  K, we obtain the value  $1.3$   $\mu\text{m}$  for the chain stretch both with and without account for hydrodynamic interactions, and the value  $0.092k_{\text{B}}T/\zeta$  for both the long- and short-time diffusivities under free draining conditions, which are close to the value  $1.5$   $\mu\text{m}$  reported for the stretch by Jendřejack et al. and the diffusivity  $k_{\text{B}}T/(N\zeta)$  of a free draining chain. Under the same conditions in the presence of hydrodynamic interactions, we obtain the value  $5.1$  s for the longest relaxation time, which is about 20% higher than the value reported by Smith and Chu [67], but is lower than the value of  $5.4$  s determined from simulation by Stoltz et al. [113]. For the radius of gyration, we obtain  $0.78$   $\mu\text{m}$ , which is in close accord with the results of Refs. [49,60,65]. We obtain  $0.0116$   $\mu\text{m}^2/\text{s}$  and  $0.0118$   $\mu\text{m}^2/\text{s}$ , respectively, for the long- and short-time diffusivities with account for hydrodynamic interactions, which are close to the value  $0.0115$   $\mu\text{m}^2/\text{s}$  reported by Jendřejack et al. [60]. Moreover, we made use of our code to repeat the study presented in Section V. D. and depicted in Figure 8 of Ref. [60], and obtained the scaling behavior  $R_{\text{g}} \sim L^{0.611}$  and  $D_{\text{S}} \sim L^{-0.581}$  upon varying the chain length, in close agreement with that obtained from renormalization group calculations [50].

The time taken for the simulation of a chain comprising  $N$  beads in the presence of hydrodynamic interactions, with the  $\mathbf{D}$  and  $\mathbf{B}$  tensors updated once in every 10 time steps, was found to grow as  $N^{2.2}$ . Table A.1 lists the time taken for the simulation of a single chain over a time period corresponding to  $10^4$  time steps on a 1.7 GHz Intel Pentium 4 processor for several values of  $N$ .

Table A.1: *Time taken per  $10^4$  steps for the simulation of a single chain of  $N$  beads with hydrodynamic interactions on a 1.7 GHz processor*

$N$	$t$ (s per $10^4$ steps)
11	10.97
21	24.52
41	90.52
61	263.0
81	532.6
101	906.6
141	2107
201	5153

### A.3 Parameter Determination

We now return to the problem of determining  $v$  and  $a$  to best reproduce the radius of gyration and diffusivity reported by Chen et al. [47] and the relaxation time reported by Perkins et al. [66] and Smith and Chu [67], with  $T = 294$  K and  $\eta = 1.08$  cP. By conducting free draining simulations wherein the value of  $v$  is varied, we were able to establish that the value  $\tilde{v} = 3 \times 10^{-5}$  (dimensionally,  $v = 2.8 \times 10^{-4} \mu\text{m}^3$ ) yields the value  $0.69 \mu\text{m}$  for the radius of gyration, identical to that determined by Chen et al. [47]. Note that the experimental determination of  $R_g$  follows indirectly from the measurement of  $D$  with use of Zimm's expression for the drag on a coil [50].

The equilibrium radius of gyration obtained from simulation is unaffected by the value of  $a$ , which is next varied in simulation with account for hydrodynamic interactions. Table A.2 summarizes the results of our parametric studies. The value  $\tilde{a} = 0.045$  (dimensionally,  $a = 94.45$  nm) yields the results  $D_S = 0.47 \mu\text{m}^2/\text{s}$  and  $\tau = 0.14$  s when used in conjunction with the value  $\tilde{v} = 3 \times 10^{-5}$ , which are in reasonable accord with the experimentally measured values [47, 66, 67]. With the selected parameter set, we obtain the scaling behavior  $R_g \sim L^{0.539}$  and  $D_S \sim L^{-0.551}$ , which are close to the scaling laws derived from renormalization group calculations [50].

Table A.2: *Parameter dependence of results obtained from Brownian dynamics simulation of  $\lambda$ -DNA with hydrodynamic interactions*

$\tilde{v}$	$\tilde{a}$	$R_g$ ( $\mu\text{m}$ )	$D_s$ ( $\mu\text{m}^2/\text{s}$ )	$\tau$ (s)
$3.0 \times 10^{-5}$	0.044	0.69	0.48	0.1350
$3.0 \times 10^{-5}$	0.045	0.69	0.47	0.1367
$3.0 \times 10^{-5}$	0.046	0.69	0.47	0.1391
$3.5 \times 10^{-5}$	0.050	0.69	0.45	0.1497
$3.0 \times 10^{-5}$	0.040	0.69	0.50	0.1264
$4.0 \times 10^{-5}$	0.040	0.71	0.49	0.1293
$5.0 \times 10^{-5}$	0.040	0.73	0.48	0.1312
$8.0 \times 10^{-5}$	0.040	0.75	0.47	0.1367
$2.0 \times 10^{-5}$	0.045	0.66	0.48	0.1335
$3.5 \times 10^{-5}$	0.045	0.69	0.47	0.1383
$5.0 \times 10^{-5}$	0.045	0.72	0.45	0.1438
$8.0 \times 10^{-5}$	0.045	0.76	0.44	0.1522



## *Nonisothermal Flow Around an Ellipsoid*

---

### B.1 $O(\epsilon)$ Temperature Field

We here solve in detail the  $O(\epsilon)$  temperature problem for the flow around the ellipsoid as discussed in Chapter 3. From Equations 3.25 and 3.26, the boundary conditions for the  $O(\epsilon)$  temperature problem appropriate to this geometry reduce to

$$\mathbf{T}^{(1)}\Big|_a = \mathbf{T}_s^{(1)}\Big|_a + 2\left(\frac{1-\gamma}{2+\gamma}\right) a\mathbf{B} : \mathbf{P}_2\mathbf{P}_1 \quad (\text{B.1})$$

and

$$\hat{\mathbf{r}} \cdot \nabla \mathbf{T}^{(1)}\Big|_a + 2\left(\frac{1-\gamma}{2+\gamma}\right) \left[ 2\mathbf{B} : \mathbf{P}_2\mathbf{P}_1 - \hat{\mathbf{V}}\mathbf{P}_2 : \mathbf{B} \right] = \gamma \hat{\mathbf{r}} \cdot \nabla \mathbf{T}_s^{(1)}\Big|_a \quad (\text{B.2})$$

Since  $\mathbf{P}_1(\hat{\mathbf{r}}) = \hat{\mathbf{r}}$  and  $\mathbf{P}_2(\hat{\mathbf{r}}) = (3\hat{\mathbf{r}}\hat{\mathbf{r}} - \mathbf{I})/2$ , we obtain

$$\mathbf{P}_2\mathbf{P}_1 = \frac{3}{2}\hat{\mathbf{r}}\hat{\mathbf{r}} - \frac{1}{2}\mathbf{I}\hat{\mathbf{r}} \quad (\text{B.3})$$

which, in combination with the expression [75]

$$\hat{\mathbf{r}}\hat{\mathbf{r}} = \frac{2}{5}\mathbf{P}_3 + \frac{1}{5} \left[ (\mathbf{IP}_1) + (\mathbf{IP}_1)^\dagger + (\mathbf{P}_1\mathbf{I}) \right] \quad (\text{B.4})$$

yields

$$\mathbf{P}_2\mathbf{P}_1 = \frac{3}{5}\mathbf{P}_3 - \frac{1}{5}(\mathbf{IP}_1) + \frac{3}{10}(\mathbf{IP}_1)^\dagger + \frac{3}{10}(\mathbf{P}_1\mathbf{I}) \quad (\text{B.5})$$

Straightforward differentiation of  $\mathbf{P}_2$  yields

$$\hat{\mathbf{V}}\mathbf{P}_2 = \frac{3}{2} \left[ \mathbf{I}\hat{\mathbf{r}} + (\mathbf{I}\hat{\mathbf{r}})^\dagger - 2\hat{\mathbf{r}}\hat{\mathbf{r}} \right] \quad (\text{B.6})$$

where the transposition symbol  $\dagger$  entails the interchange of the two indices immediately preceding or succeeding it, according as it follows or precedes the argument to which it is affixed. Therefore, upon making use of Equation (B.4), we obtain

$$\hat{\mathbf{V}}\mathbf{P}_2 = \frac{9}{10} \left[ \mathbf{IP}_1 + (\mathbf{IP}_1)^\dagger \right] - \frac{6}{5}\mathbf{P}_3 - \frac{3}{5}\mathbf{P}_1\mathbf{I} \quad (\text{B.7})$$

Equations B.1 and B.2 now simplify to

$$\mathbf{T}^{(1)} \Big|_a = \mathbf{T}_s^{(1)} \Big|_a + 2 \left( \frac{1-\gamma}{2+\gamma} \right) a \mathbf{B} : \left[ \frac{3}{5}\mathbf{P}_3 - \frac{1}{5}\mathbf{IP}_1 + \frac{3}{10}(\mathbf{IP}_1)^\dagger + \frac{3}{10}\mathbf{P}_1\mathbf{I} \right] \quad (\text{B.8})$$

and

$$\begin{aligned} \frac{\partial \mathbf{T}^{(1)}}{\partial r} \Big|_a + 2 \left( \frac{1-\gamma}{2+\gamma} \right) \left\{ 2\mathbf{B} : \left[ \frac{3}{5}\mathbf{P}_3 - \frac{1}{5}\mathbf{IP}_1 + \frac{3}{10}(\mathbf{IP}_1)^\dagger + \frac{3}{10}\mathbf{P}_1\mathbf{I} \right] \right. \\ \left. - \left[ \frac{9}{10}\mathbf{IP}_1 + \frac{9}{10}(\mathbf{IP}_1)^\dagger - \frac{6}{5}\mathbf{P}_3 - \frac{3}{5}\mathbf{P}_1\mathbf{I} \right] : \mathbf{B} \right\} = \gamma \frac{\partial \mathbf{T}_s^{(1)}}{\partial r} \Big|_a \end{aligned} \quad (\text{B.9})$$

Owing to the symmetry of  $\mathbf{B}$ , the boundary conditions, Equations B.8 and B.9, may be rewritten in the forms

$$\mathbf{T}^{(1)} \Big|_a = \mathbf{T}_s^{(1)} \Big|_a + \frac{6}{5} \left( \frac{1-\gamma}{2+\gamma} \right) a (\mathbf{P}_1 \cdot \mathbf{B} + \mathbf{P}_3 : \mathbf{B}) \quad (\text{B.10})$$

and

$$\frac{\partial \mathbf{T}^{(1)}}{\partial r} \Big|_a - \frac{6}{5} \left( \frac{1-\gamma}{2+\gamma} \right) [\mathbf{P}_1 \cdot \mathbf{B} - 4\mathbf{P}_3 : \mathbf{B}] = \gamma \frac{\partial \mathbf{T}_s^{(1)}}{\partial r} \Big|_a \quad (\text{B.11})$$

Upon expanding  $\mathbf{T}^{(1)}$  and  $\mathbf{T}_s^{(1)}$  in solid harmonics and imposing the boundary conditions, Equations B.10 and B.11, in conjunction with the vanishing of  $\mathbf{T}^{(1)}$  at infinity and the finiteness of  $\mathbf{T}_s^{(1)}$  at  $r = 0$ , we eventually obtain the respective expressions given in Equations 3.45 and 3.46.

## B.2 Derivation of $\mathbf{K}^{(1)}$

Here, we present the detailed computation of  $\mathbf{K}^{(1)}$ , which is given by Equation 3.54. Since  $P_0 = 1$ , and  $\hat{\mathbf{r}} = 2\mathbf{P}_2/3 + \mathbf{I}/3$ , it follows that

$$\int_{S_1} \mathbf{P}_2 (\mathbf{I} - 2\hat{\mathbf{r}}) d\Omega = -\frac{4}{3} \int_{S_1} \mathbf{P}_2 \mathbf{P}_2 d\Omega \quad (\text{B.12})$$

where we have used the orthogonality of the polyadics  $\mathbf{P}_n$ . We make use of Equation B.7 to write

$$\begin{aligned} \int_{S_1} \hat{\mathbf{r}} \hat{\nabla} \mathbf{P}_2 d\Omega &= \frac{9}{10} \int_{S_1} \mathbf{P}_1 \mathbf{I} \mathbf{P}_1 d\Omega + \frac{9}{10} \int_{S_1} \mathbf{P}_1 (\mathbf{I} \mathbf{P}_1)^\dagger d\Omega \\ &\quad - \frac{6}{5} \int_{S_1} \mathbf{P}_1 \mathbf{P}_3 d\Omega - \frac{3}{5} \int_{S_1} \mathbf{P}_1 \mathbf{P}_1 d\Omega \mathbf{I} \end{aligned} \quad (\text{B.13})$$

We know that  $\int_{S_1} \mathbf{P}_1 \mathbf{P}_1 d\Omega = 4\pi \mathbf{I}/3$ , and  $\int_{S_1} \mathbf{P}_1 \mathbf{P}_3 d\Omega = \mathbf{0}$ . Reverting to Cartesian tensor notation in order to calculate the remaining integrals in Equations B.12 and B.13 yields

$$\int_{S_1} (\mathbf{P}_2 \mathbf{P}_2)_{ijkl} d\Omega = \frac{\pi}{5} (-2\delta_{ij}\delta_{kl} + 3\delta_{ik}\delta_{jl} + 3\delta_{il}\delta_{jk}) \quad (\text{B.14})$$

$$\int_{S_1} (\mathbf{P}_1 \mathbf{I} \mathbf{P}_1)_{ijkl} d\Omega = \frac{4\pi}{3} \delta_{il}\delta_{jk} \quad (\text{B.15})$$

$$\int_{S_1} [\mathbf{P}_1 (\mathbf{I} \mathbf{P}_1)^\dagger]_{ijkl} d\Omega = \frac{4\pi}{3} \delta_{ik}\delta_{jl} \quad (\text{B.16})$$

and, hence,

$$\int_{S_1} (\hat{\mathbf{r}} \hat{\nabla} \mathbf{P}_2)_{ijkl} d\Omega = \frac{2\pi}{5} (3\delta_{il}\delta_{jk} + 3\delta_{ik}\delta_{jl} - 2\delta_{ij}\delta_{kl}) \quad (\text{B.17})$$

Since  $\mathbf{B}$  is a traceless, symmetric dyadic,  $\delta_{il}\delta_{jk} : \mathbf{B} = \delta_{ik}\delta_{jl} : \mathbf{B} = \mathbf{B}$ , and  $\delta_{ij}\delta_{kl} : \mathbf{B} = \text{Tr}(\mathbf{B})\mathbf{I} = \mathbf{0}$ .

Similarly,

$$\begin{aligned} \int_{S_1} \hat{\nabla} \mathbf{P}_2 : \mathbf{B} \hat{\mathbf{r}} d\Omega &= \frac{9}{10} \int_{S_1} \mathbf{I} \mathbf{P}_1 : \mathbf{B} \mathbf{P}_1 d\Omega + \frac{9}{10} \int_{S_1} (\mathbf{I} \mathbf{P}_1)^\dagger : \mathbf{B} \mathbf{P}_1 d\Omega \\ &\quad - \frac{6}{5} \int_{S_1} \mathbf{P}_3 : \mathbf{B} \mathbf{P}_1 d\Omega - \frac{3}{5} \int_{S_1} \mathbf{P}_1 \mathbf{I} : \mathbf{B} \mathbf{P}_1 d\Omega \end{aligned} \quad (\text{B.18})$$

Again, we evaluate Equation B.18 in Cartesian tensor notation to obtain

$$\int_{S_1} \hat{\nabla} \mathbf{P}_2 : \mathbf{B} \hat{\mathbf{r}} d\Omega = \frac{12\pi}{5} \mathbf{B} \quad (\text{B.19})$$

Finally,

$$\int_{S_1} (\mathbf{I} - \hat{\mathbf{r}}\hat{\mathbf{r}}) d\Omega = \frac{8\pi}{3}\mathbf{I} \quad (\text{B.20})$$

In invariant notation, we finally obtain, upon substitution of Equations B.12, B.14, B.17, B.19 and B.20 in Equation 3.54, the result for  $\mathbf{K}^{(1)}$  given in Equation 3.55.

## *Normal Mode Analysis of a Tethered Rouse Chain*

---

### C.1 Normal Mode Solution

In this Appendix, we present the solution of the Langevin equations, given by Equations 4.1 and 4.2 of Chapter 4, for a Rouse chain. For convenience, we use dimensional notation in the following analysis. The force acting on bead  $j$  is given by Hooke's law:

$$\begin{aligned}\mathbf{F}_j &= H(\mathbf{r}_{j+1} - 2\mathbf{r}_j + \mathbf{r}_{j-1}), \quad j = 1, \dots, N-2 \\ &= -H(\mathbf{r}_{N-1} - \mathbf{r}_{N-2}), \quad j = N-1\end{aligned}\tag{C.1}$$

where, as stated in Chapter 4,  $H = 3k_B T / (\lambda b_k^2 N_{k,s})$ . Since  $\mathbf{r}_0(t) = \mathbf{0} \forall t$ , it follows that  $\mathbf{F}_1 = H(\mathbf{r}_2 - 2\mathbf{r}_1)$ . Therefore, we obtain the equations

$$d\mathbf{r}_j = \left( \mathbf{v} - \frac{H}{\zeta} \sum_{k=1}^{N-1} A_{jk} \mathbf{r}_k \right) dt + \sqrt{\frac{2k_B T}{\zeta}} d\mathbf{W}_j, \quad j = 1, \dots, N-1\tag{C.2}$$

where  $A_{jk}$  ( $j, k = 1, \dots, N-1$ ) are the matrix elements of the  $(N-1) \times (N-1)$  Rouse matrix

$$\mathbf{A} = \begin{bmatrix} 2 & -1 & \cdot & \cdot \\ -1 & 2 & -1 & \cdot \\ \cdot & \cdot & \cdot & \cdot \\ \cdot & \cdot & -1 & 1 \end{bmatrix} \quad (\text{C.3})$$

$\mathbf{A}$ , being a real, symmetric, positive definite matrix, possesses real, positive eigenvalues and a complete set of orthonormal eigenvectors. Consequently,  $\mathbf{A}$  is diagonalized by the similarity transformation  $[\Omega^{-1} \mathbf{A} \Omega]_{jk} = a_k \delta_{jk}$ , where  $a_k > 0$  ( $k = 1, \dots, N-1$ ) are the eigenvalues of  $\mathbf{A}$ , while  $\Omega$  is the unitary matrix whose columns are the eigenvectors of  $\mathbf{A}$ . The unitarity of  $\Omega$  leads to the equality

$$\sum_{j=1}^{N-1} \Omega_{ji} \Omega_{jk} = \delta_{ik}, \quad i, k = 1, \dots, N-1 \quad (\text{C.4})$$

We now make use of Equation C.4 to introduce the transformations

$$\mathbf{r}_j = \sum_{k=1}^{N-1} \Omega_{jk} \mathbf{r}'_k \quad (\text{C.5})$$

$$\mathbf{r}'_k = \sum_{j=1}^{N-1} \Omega_{jk} \mathbf{r}_j \quad (\text{C.6})$$

By means of the above transformations, Equation C.2 may be expressed in terms of the variables  $\mathbf{r}'_k$ . A subsequent multiplication by  $\Omega_{jm}$  and a summation over the index  $j$ , followed by an application of Equation C.4 and the similarity transformation, finally yield the set of equations

$$d\mathbf{r}'_m = \left( \sum_{j=1}^{N-1} \Omega_{jm} \mathbf{v} - \frac{H}{\zeta} a_m \mathbf{r}'_m \right) dt + \sqrt{\frac{2k_B T}{\zeta}} d\mathbf{W}'_m, \quad m = 1, \dots, N-1 \quad (\text{C.7})$$

where we have introduced the independent vector Wiener processes  $\mathbf{W}'_m$  via

$$d\mathbf{W}'_m = \sum_{j=1}^{N-1} \Omega_{jm} d\mathbf{W}_j \quad (\text{C.8})$$

It is readily verified that  $\langle d\mathbf{W}'_m(t) \rangle = \mathbf{0}$  and  $\langle d\mathbf{W}'_m(t) d\mathbf{W}'_n(t') \rangle = dt \delta_{mn} \delta(t-t') \boldsymbol{\delta}$ , with  $m, n = 1, \dots, N-1$ . The solution of the decoupled, linear stochastic differential equations represented by

Equations C.7 may be effected [57] to yield

$$\mathbf{r}'_m(t) = \exp\left(-\frac{H}{\zeta}a_m t\right) \mathbf{r}'_m(0) + \frac{\zeta \mathbf{v}}{H a_m} \left( \sum_{j=1}^{N-1} \Omega_{jm} \right) \left[ 1 - \exp\left(-\frac{H}{\zeta}a_m t\right) \right] + \sqrt{\frac{2k_B T}{\zeta}} \int_0^t d\mathbf{W}'_m(t') \exp\left(-\frac{H}{\zeta}a_m(t-t')\right) \quad (\text{C.9})$$

where the stochastic integral on the right hand side of the above equation is a Gaussian random variable having vanishing mean. An application of Equations C.5 and C.6 to Equation C.9 finally yields the expression

$$\mathbf{r}_k(t) = \sum_{m,l=1}^{N-1} \Omega_{km} \exp\left(-\frac{H a_m t}{\zeta}\right) \Omega_{lm} \mathbf{r}_l(0) + \frac{\zeta}{H} \mathbf{v} \sum_{m,j=1}^{N-1} \Omega_{km} \Omega_{jm} \frac{1 - \exp\left(-\frac{H}{\zeta}a_m t\right)}{a_m} + \sqrt{\frac{2k_B T}{\zeta}} \sum_{m=1}^{N-1} \Omega_{km} \int_0^t d\mathbf{W}'_m(t') \exp\left(-\frac{H}{\zeta}a_m(t-t')\right) \quad (\text{C.10})$$

Since our initial configuration corresponds to an equilibrium Gaussian coil with vanishing mean spring vectors, the mean initial bead positions must also vanish. We now employ Equation C.10 to derive the mean bead positions at time  $t$ :

$$\langle \mathbf{r}_k(t) \rangle = \frac{\zeta}{H} \mathbf{v} \sum_{m,j=1}^{N-1} \Omega_{km} \Omega_{jm} \frac{1 - \exp\left(-\frac{H}{\zeta}a_m t\right)}{a_m} \quad (\text{C.11})$$

The mean end-to-end distance in the flow direction readily follows from Equation C.11:

$$L_e = \langle \mathbf{r}_{N-1}(t) \rangle \cdot \hat{\mathbf{x}} = \frac{\zeta}{H} v \sum_{m,j=1}^{N-1} \Omega_{N-1,m} \Omega_{jm} \frac{1 - \exp\left(-\frac{H}{\zeta}a_m t\right)}{a_m} \quad (\text{C.12})$$

The mean spring tension in spring  $k$  ( $k = 1, \dots, N-1$ ) in the flow direction is given by the expressions

$$F_{\text{spr } 1, x} = \zeta v \sum_{m,j=1}^{N-1} \Omega_{1m} \Omega_{jm} \frac{1 - \exp\left(-\frac{H}{\zeta}a_m t\right)}{a_m} \quad (\text{C.13})$$

and

$$F_{\text{spr } k, x} = \zeta v \sum_{m,j=1}^{N-1} (\Omega_{km} - \Omega_{k-1,m}) \Omega_{jm} \frac{1 - \exp\left(-\frac{H}{\zeta}a_m t\right)}{a_m}, \quad k > 1 \quad (\text{C.14})$$

Equations C.12–C.14 are expressed in the dimensionless notation introduced in Chapter 4, Section 4.2 by Equations 4.3–4.5.

The eigenvalues and eigenvectors of the Rouse matrix remain to be specified. In our study, we

make use of the solution provided by Rzehak and Zimmermann [95], given by Equations 4.6 and 4.7.

## C.2 Continuous Approximation

In the continuous limit of the linear bead–spring model with  $N \gg 1$ , the bead positions  $\mathbf{r}_j$  are governed by the equation [24]

$$\frac{\partial \mathbf{r}_j}{\partial t} = \frac{H}{\zeta} \frac{\partial^2 \mathbf{r}_j}{\partial j^2} \quad (\text{C.15})$$

subject to the boundary conditions

$$\begin{aligned} \mathbf{r}_j(j=0) &= \mathbf{0} \\ \left. \frac{\partial \mathbf{r}_j}{\partial j} \right|_{j=N} &= \mathbf{0} \end{aligned} \quad (\text{C.16})$$

the eigenvalues and eigenvectors for which are given by the expressions

$$a_m^c = \left[ \left( m - \frac{1}{2} \right) \frac{\pi}{N} \right]^2 \quad (\text{C.17})$$

and

$$\Omega_{jm}^c = \frac{1}{\sqrt{\frac{N}{2} - \frac{1}{4}}} \sin \left( \frac{2m-1}{2N} \pi j \right) \quad (\text{C.18})$$

with the superscript  $c$  denoting the continuous approximation. With the exception of the tension in the spring at the free chain end (which becomes negative at very early times), the solution obtained by means of the continuous approximation is found to be indistinguishable from that obtained using the eigenmodes of Rzehak and Zimmermann for a chain of 61 beads, thus reinforcing the scaling of the relaxation times for the slow modes with  $N^2$  for  $N \gg 1$ .

---

## *Bibliography*

---

- [1] S. Chapman and T. G. Cowling. *The Mathematical Theory of Non-uniform Gases: An Account of the Kinetic Theory of Viscosity, Thermal Conduction and Diffusion in Gases*. Cambridge University Press, Cambridge, 1970.
- [2] M. N. Kogan, V. S. Galkin, and O. G. Fridlender. *Sov. Phys. Usp.*, 19:420–428, 1976.
- [3] J. C. Maxwell. *Philos. Trans. R. Soc. London*, 170:231–256, 1879.
- [4] A. V. Bobylev. *J. Stat. Phys.*, 80:1063–1083, 1995.
- [5] O. Reynolds. *Philos. Trans. R. Soc. London*, 170:727–845, 1879.
- [6] P. S. Epstein. *Z. Phys.*, 54:537–563, 1929.
- [7] J. Tyndall. *Proc. R. Inst.*, 6:1–14, 1870.
- [8] F. Zheng. *Adv. Colloid Interface Sci.*, 97:255–278, 2002.
- [9] M. N. Kogan. *Rarefied Gas Dynamics*. Plenum Press, New York, 1969.
- [10] M. N. Kogan. *Annu. Rev. Fluid Mech.*, 5:383–404, 1973.
- [11] V. S. Galkin, M. N. Kogan, and O. G. Fridlender. *Fluid Dynamics*, 7:287–292, 1974.

- [12] S. G. Brush. *Kinetic Theory*, volume 3. Pergamon, New York, 1972.
- [13] V. S. Galkin, M. N. Kogan, and O. G. Fridlender. *Fluid Dynamics*, 5:364–371, 1973.
- [14] F. A. Morrison. *J. Colloid Interface Sci.*, 34:210–214, 1970.
- [15] M. E. Schimpf and S. N. Semenov. *J. Phys. Chem. B*, 104:9935–9942, 2000.
- [16] M. E. Schimpf and S. N. Semenov. *J. Phys. Chem. B*, 105:2285–2290, 2001.
- [17] S. N. Semenov. *Philos. Mag.*, 83:2199–2208, 2003.
- [18] S. N. Semenov and M. E. Schimpf. *Phys. Rev. E*, 69:011201, 2004.
- [19] R. Piazza and A. Guarino. *Phys. Rev. Lett.*, 88:208302, 2002.
- [20] J. L. Anderson. *Annu. Rev. Fluid Mech.*, 21:61–99, 1989.
- [21] A. Regazzetti, M. Hoyos, and M. Martin. *J. Phys. Chem. B*, 108:15285–15292, 2004.
- [22] D. A. Saville. *Annu. Rev. Fluid Mech.*, 9:321–337, 1977.
- [23] J.-L. Viovy. *Rev. Mod. Phys.*, 72:813–872, 2000.
- [24] P. G. de Gennes. *Scaling Concepts in Polymer Physics*. Cornell University Press, Ithaca, 1979.
- [25] A. E. Barron, D. S. Soane, and H. W. Blanch. *J. Chromatogr. A*, 652:3–16, 1993.
- [26] A. E. Barron, H. W. Blanch, and D. S. Soane. *Electrophoresis*, 15:597–615, 1994.
- [27] M. E. Starkweather, M. Muthukumar, and D. A. Hoagland. *Macromolecules*, 31:5495–5501, 1998.
- [28] M. E. Starkweather, D. A. Hoagland, and M. Muthukumar. *Macromolecules*, 33:1245–1253, 2000.
- [29] W. D. Volkmuth and R. H. Austin. *Nature*, 358:600–602, 1992.
- [30] P. S. Doyle, J. Bibette, A. Bancaud, and J.-L. Viovy. *Science*, 295:2237, 2002.
- [31] N. Minc, C. Futterer, K. D. Dorfman, A. Bancaud, C. Gosse, C. Goubault, and J.-L. Viovy. *Anal. Chem.*, 76:3770–3776, 2004.
- [32] N. Minc, P. Bokov, K. B. Zeldovich, C. Futterer, J.-L. Viovy, and K. D. Dorfman. *Electrophoresis*, 26:362–375, 2005.
- [33] K. Inatomi, S. Izuo, S. Lee, H. Ohji, and S. Shiono. *Microelectronic Engineering*, 70:13–18, 2003.
- [34] N. Minc, J.-L. Viovy, and K. D. Dorfman. *Phys. Rev. Lett.*, 94:198105, 2005.
- [35] K. D. Dorfman. *Phys. Rev. E*, 73:061922, 2006.

- [36] E. M. Sevick and D. R. M. Williams. *Phys. Rev. Lett.*, 76:2595–2598, 1996.
- [37] P. M. Saville and E. M. Sevick. *Macromolecules*, 32:892–899, 1999.
- [38] E. M. Sevick and D. R. M. Williams. *Europhys. Lett.*, 56:529–535, 2001.
- [39] G. C. Randall and P. S. Doyle. *Phys. Rev. Lett.*, 93:058102, 2004.
- [40] G. C. Randall and P. S. Doyle. *Macromolecules*, 38:2410–2418, 2005.
- [41] G. C. Randall and P. S. Doyle. *Macromolecules*, 39:7734–7745, 2006.
- [42] J. M. Kim and P. S. Doyle. *Macromolecules*, under consideration, 2007.
- [43] D. Long, A. V. Dobrynin, M. Rubinstein, and A. Ajdari. *J. Chem. Phys.*, 108:1234–1244, 1998.
- [44] M. Mandelkern, J. G. Elias, D. Eden, and D. M. Crothers. *J. Mol. Biol.*, 152:153–161, 1981.
- [45] T. Strick, J.-F. Allemand, V. Croquette, and D. Bensimon. *Prog. Biophys. Mol. Biol.*, 74:115–140, 2000.
- [46] T. T. Perkins, D. E. Smith, R. G. Larson, and S. Chu. *Science*, 268:83–87, 1995.
- [47] Y.-L. Chen, M. D. Graham, J. J. de Pablo, G. C. Randall, M. Gupta, and P. S. Doyle. *Phys. Rev. E*, 70:060901, 2004.
- [48] P. J. Flory. *Principles of Polymer Chemistry*. Cornell University Press, Ithaca, 1953.
- [49] R. G. Larson. *J. Rheol.*, 49:1–70, 2005.
- [50] M. Doi and S. F. Edwards. *The Theory of Polymer Dynamics*. Clarendon, Oxford, 1986.
- [51] M. Fixman and J. Kovac. *J. Chem. Phys.*, 58:1564–1568, 1973.
- [52] J. F. Marko and E. D. Siggia. *Macromolecules*, 28:8759–8770, 1995.
- [53] P. D. Patel and E. S. G. Shaqfeh. *J. Chem. Phys.*, 118:2941–2951, 2003.
- [54] R. B. Bird, C. F. Curtiss, R. C. Armstrong, and O. Hassager. *Dynamics of Polymeric Liquids*, volume 2: Kinetic Theory. Wiley Interscience, New York, second edition, 1987.
- [55] P. T. Underhill and P. S. Doyle. *J. Non-Newton. Fluid Mech.*, 122:3–31, 2004.
- [56] S. Chandrasekhar. *Rev. Mod. Phys.*, 15:1–89, 1943.
- [57] H. C. Oettinger. *Stochastic Processes in Polymeric Fluids: Tools and Examples for Developing Simulation Algorithms*. Springer, Berlin, 1996.
- [58] D. L. Ermak and J. A. McCammon. *J. Chem. Phys.*, 69:1352–1360, 1978.
- [59] C. Pozrikidis. *Introduction to Theoretical and Computational Fluid Dynamics*. Oxford University Press, New York, 1997.

- [60] R. M. Jendrejack, J. J. de Pablo, and M. D. Graham. *J. Chem. Phys.*, 116:7752–7759, 2002.
- [61] J. Rotne and S. Prager. *J. Chem. Phys.*, 50:4831–4837, 1969.
- [62] H. Yamakawa. *J. Chem. Phys.*, 53:436–443, 1970.
- [63] C. C. Hsieh, L. Li, and R. G. Larson. *J. Non-Newt. Fluid Mech.*, 113:147–191, 2003.
- [64] C. M. Schroeder, E. S. G. Shaqfeh, and S. Chu. *Macromolecules*, 37:9242–9256, 2004.
- [65] D. E. Smith, T. T. Perkins, and S. Chu. *Macromolecules*, 29:1372–1373, 1996.
- [66] T. T. Perkins, D. E. Smith, and S. Chu. *Science*, 276:2016–2021, 1997.
- [67] D. E. Smith and S. Chu. *Science*, 281:1335–1340, 1998.
- [68] H. P. Babcock, R. E. Teixeira, J. S. Hur, E. S. G. Shaqfeh, and S. Chu. *Macromolecules*, 36:4544–4548, 2003.
- [69] L. Li, H. Hu, and R. G. Larson. *Rheol. Acta*, 44:38–46, 2004.
- [70] R. G. Larson. *The Structure and Rheology of Complex Fluids*. Oxford University Press, Oxford, 1999.
- [71] B. D. Hughes. *Random Walks and Random Environments*, volume 1: Random Walks. Clarendon, Oxford, 1995.
- [72] R. Haghgoie and P. S. Doyle. *Phys. Rev. E*, 70:061408, 2004.
- [73] R. Haghgoie and P. S. Doyle. *Phys. Rev. E*, 72:011405, 2005.
- [74] J. Happel and H. Brenner. *Low Reynolds Number Hydrodynamics*. Prentice Hall Inc., Englewood Cliffs, N. J., 1965.
- [75] H. Brenner. *Chem. Eng. Sci.*, 19:703–727, 1964.
- [76] E. Yariv and H. Brenner. *Phys. Fluids*, 14:3354–3357, 2002.
- [77] M. M. R. Williams. *J. Phys. D: Appl. Phys.*, 19:1631–1642, 1986.
- [78] M. M. R. Williams. *J. Phys. D: Appl. Phys.*, 20:354–359, 1987.
- [79] D. W. Mackowski. *J. Colloid Interface Sci.*, 140:138–157, 1990.
- [80] H. Brenner. *Chem. Eng. Sci.*, 19:519–539, 1964.
- [81] D. L. Ripps and H. Brenner. *Chem. Eng. Sci.*, 22:375–387, 1967.
- [82] T. M. MacRobert. *Spherical Harmonics: An Elementary Treatise on Harmonic Functions With Applications*. Dover Publications, New York, 1948.
- [83] H. Brenner. *J. Fluid Mech.*, 111:197–215, 1981.
- [84] H. Brenner and L. J. Gajdos. *Can. J. Chem.*, 59:2004–2018, 1981.

- [85] S. Ferree and H. W. Blanch. *Biophys. J.*, 85:2539–2546, 2003.
- [86] R. G. Larson, T. T. Perkins, D. E. Smith, and S. Chu. *Phys. Rev. E*, 55:1794–1797, 1997.
- [87] M. Cheon, I. Chang, J. Koplik, and J. R. Banavar. *Europhys. Lett.*, 58:215–221, 2002.
- [88] F. Brochard-Wyart. *Europhys. Lett.*, 23:105–111, 1993.
- [89] F. Brochard-Wyart. *Europhys. Lett.*, 30:387–392, 1995.
- [90] R. Rzehak, W. Kromen, T. Kawakatsu, and W. Zimmermann. *Eur. Phys. J. E*, 2:3–30, 2000.
- [91] R. Rzehak, D. Kienle, T. Kawakatsu, and W. Zimmermann. *Europhys. Lett.*, 46:821–826, 1999.
- [92] F. Brochard-Wyart, H. Hervet, and P. Pincus. *Europhys. Lett.*, 26:511–516, 1994.
- [93] K. Avramova, V. Yamakov, and A. Milchev. *Macromol. Theory Simul.*, 9:516–522, 2000.
- [94] R. Rzehak and W. Zimmermann. *Europhys. Lett.*, 59:779–785, 2002.
- [95] R. Rzehak and W. Zimmermann. *Phys. Rev. E*, 68:021804, 2003.
- [96] R. Rzehak. *Eur. Phys. J. E*, 11:335–348, 2003.
- [97] O. Hallatschek, E. Frey, and K. Kroy. *Phys. Rev. Lett.*, 94:077804, 2005.
- [98] U. Seifert, W. Wintz, and P. Nelson. *Phys. Rev. Lett.*, 77:5389–5392, 1996.
- [99] H. S. Carslaw and J. C. Jaeger. *Conduction of Heat in Solids*. Oxford University Press, Oxford, second edition, 1959.
- [100] H. Scher and M. Lax. *Phys. Rev. B*, 7:4491–4502, 1973.
- [101] S. Popelka, Z. Kabatek, J.-L. Viovy, and B. Gas. *J. Chromatography A*, 838:45–53, 1999.
- [102] A. Mohan and P. S. Doyle. *Macromolecules*, 40:4301–4312, 2007.
- [103] G. I. Nixon and G. W. Slater. *Phys. Rev. E*, 50:5033–5038, 1994.
- [104] D. M. Heyes and J. R. Melrose. *J. Non-Newtonian Fluid Mech.*, 46:1–28, 1993.
- [105] M. H. DeGroot and M. J. Schervish. *Probability and Statistics*. Addison–Wesley, New York, 2002.
- [106] M. P. Allen and D. J. Tildesley. *Computer Simulation of Liquids*. Oxford University Press, Oxford, 1987.
- [107] M. G. Gauthier and G. W. Slater. *J. Chem. Phys.*, 117:6745–6756, 2002.
- [108] M. G. Gauthier, G. W. Slater, and K. D. Dorfman. *Eur. Phys. J. E*, 15:71–82, 2004.
- [109] M. Muthukumar. *J. Non-Crystalline Solids*, 131–133:654–666, 1991.

- [110] D. R. Nelson and B. I. Halperin. *Phys. Rev. B*, 19:2457–2484, 1979.
- [111] W. H. Press, S. A. Teukolsky, W. T. Vetterling, and B. P. Flannery. *Numerical Recipes in Fortran: The Art of Scientific Computing*. Cambridge University Press, New York, second edition, 1992.
- [112] P. S. Grassia, E. J. Hinch, and L. C. Nitsche. *J. Fluid Mech.*, 282:373–403, 1995.
- [113] C. Stoltz, J. J. de Pablo, and M. D. Graham. *J. Rheol.*, 50:137–167, 2006.